



Hydrodynamics and cross-shore sand transport during barrier island inundation

Anita Engelstad

Hydrodynamics and cross-shore sand transport during barrier island inundation

Hydrodynamica en kustdwars zand transport tijdens overstroming van Wadden eilanden

(met een samenvatting in het Nederlands)

PROEFSCHRIFT

ter verkrijging van de graad van doctor aan de Universiteit Utrecht
op gezag van de rector magnificus, prof. dr. H.R.B.M. Kummeling,
ingevolge het besluit van het college voor promoties in het openbaar te verdedigen
op vrijdag 25 oktober 2019 des ochtends te 10.30 uur

door

Anita Cathrine Engelstad

geboren op 24 december 1965 te Heidelberg, Duitsland

Promotor:

Prof. dr. P. Hoekstra

Prof. dr. B. G. Ruessink

Copromotor:

Dr. M. van der Vegt

This work was financially supported by the Netherlands Organisation for Scientific Research (NWO) under contract 850.13.051, as well as by Natuurmonumenten, the National Forest Service (Staatsbosbeheer, SBB), and the Wadden Academy.

Hydrodynamics and cross-shore sand transport during barrier island inundation

Promotor:

Prof. dr. P. Hoekstra

Prof. dr. B. G. Ruessink

Copromotor:

Dr. M. van der Vegt

Examination committee:

Prof. dr. G. Masselink

University of Plymouth, United Kingdom

Dr. A. Matias

Universidade do Algarve, Portugal

Prof. dr. ir. A.J.H.M. Reniers

Delft University of Technology, The Netherlands

Prof. dr. ir. J.A. Roelvink

IHE Delft Institute for Water Education, The Netherlands

Prof. dr. H.E. de Swart

Utrecht University, The Netherlands

ISBN 978-90-6266-554-9

Published by Faculty of Geosciences, Universiteit Utrecht, The Netherlands, in:
Utrecht Studies in Earth Sciences (USES), ISSN 2211-4335

Typeset using X_YTEX

Printed by: IPSKAMPprinting || www.proefschriften.net.

Cover: The beach on Schiermonnikoog during a storm in December 2014.



Except where otherwise noted, this work is licensed under the Creative Commons Attribution 4.0 International Licence, <http://creativecommons.org/licenses/by/4.0/>,

© 2019 by A. Engelstad.

Chapters 2 and 3 are last-author versions of previously published articles,

© by A. Engelstad and co-authors. More information and citation suggestions are provided at the beginning of these chapters.

Utrecht Studies in Earth Sciences 196

Hydrodynamics and cross-shore sand transport during barrier island inundation

A. Engelstad

Utrecht 2019

Faculty of Geosciences, Utrecht University

Contents

Summary	1
Samenvatting	3
1 Introduction	7
1.1 Context	7
1.2 Inundation impacts and processes	10
1.3 Research objectives	13
1.4 Methods and Outline	14
2 Observations of waves and currents during barrier island inundation	17
2.1 Introduction	17
2.2 Data collection and boundary conditions	19
2.3 Data analysis	22
2.4 Results	25
2.5 Discussion	34
2.6 Conclusions	37
3 Sand suspension and transport during inundation of a Dutch barrier island	39
3.1 Introduction	39
3.2 Data collection and boundary conditions	41
3.3 Analysis of Sand Suspension and Transport	46
3.4 Results	49
3.5 Discussion	54
3.6 Conclusions	56
4 Sand transport processes during barrier island inundation under variations in cross-shore geometry and hydrodynamic forcing	59
4.1 Introduction	59
4.2 Methods	61
4.3 Results	69
4.4 Discussion	78
4.5 Conclusions	80
5 Synthesis	81
5.1 Main findings	81
5.2 Discussion and perspectives	86
Appendix A Validation of SWASH results	91
A.1 Boundary conditions and model settings	91
A.2 Model-data comparison	92
References	97

vii

Dankwoord/Acknowledgements	104
About the author	107

Summary

Barrier islands are commonly low-lying, narrow, sandy islands that parallel the mainland. They protect the coastline, adjacent marshes and wetlands from storms and create shallow lagoons and intertidal areas between the islands and the mainland. These back barrier basins, such as those in the Wadden Sea that separate the North Sea and the coasts of the Netherlands, Germany and Denmark, accommodate complex ecosystems and a large diversity of species. Sea level rise threatens the existence of barrier islands, and their survival will at least partly depend on their ability to accumulate sand or to slowly propagate landwards. Such large-scale changes in island morphology can be caused by storm-driven overwash and inundation. While barrier islands are naturally dynamic features which migrate landward or alongshore, dikes such as the sand drift dikes in the Netherlands are cutting off the sand supply to the landward side of the dikes. To alleviate the effect of sea level rise, the re-opening of these dikes is considered in the Netherlands to allow more mobility and accretion of sand. However, not much is known about the hydrodynamics and the sand transport, such as the amount and the direction of the transport, during overwash and inundation of barrier islands fringing the Wadden Sea and it is uncertain how the system will respond.

The overall aim of this study is to increase our understanding of sand transport processes during the inundation of barrier islands in the Wadden Sea. Many studies were performed on barrier islands in the US but not much field data exist since it is inherently difficult to measure hydrodynamic and sand transport processes during storms. Further, the wave-, tide- and storm climate for barrier islands in the Wadden Sea differ from the ones found in the US, and while islands in the Wadden Sea are generally short and wide, US barrier islands are overall more elongated and narrow. These characteristics are assumed to affect the response to overwash and inundation. In this thesis, the hydrodynamic and sand transport processes of barrier islands separating the North Sea and the Wadden Sea have been studied using field data collected during inundation. The effect that island geometries and hydrodynamic forcing have on the sand transport were then investigated using a numerical model.

The hydrodynamics during inundation were investigated with data collected by an array of instruments installed from North to Wadden Sea across the eastern tip of Schiermonnikoog, the Netherlands. Results (Chapter 2) show that inundation depths at the beach crest (the shallowest point in the cross-shore profile) varied between 0.3-1.5 m and that waves did not lose their energy completely when propagating across the submerged field area, while wave breaking was the dominant dissipation mechanism for short and infragravity waves. Infragravity waves (0.005-0.05 Hz) were an important part of the wave field and propagated landwards, frequently as bores. Mean cross-shore velocities landwards of the crest varied significantly between events and were generally maximum and landwards directed before high tide (0.2-1.2 m/s). At times, they reversed after high tide (max -0.2 m/s). The mean cross-shore velocities were forced by the water-level gradient between the beach crest and the Wadden Sea. While the large-scale water-level gradient between North and Wadden Sea was frequently directed towards the North Sea due to higher water levels in the Wadden Sea, the local wave set-up at the beach crest regularly exceeded water levels in the Wadden Sea.

The observed variations in mean flow velocities were also reflected in the observed net depth-integrated suspended sand transport (Chapter 3). It was often larger before high tide, resulting in $\sim 80\%$ of the sand being transported in this period. The transport direction was almost entirely landwards directed. Infragravity waves contributed to the transport when mean flow velocities were low (< 0.5 m/s) while short wave transport was insignificant. Further, episodically high suspended sand concentrations coincided with infragravity bores, which accommodated the larger short waves on their crests, so that the high sand suspension was likely caused by the combined bed shear stresses of mean flow, short- and infragravity waves. This suggests that sand transport on the barrier islands is governed by two regimes: it is flow-driven when mean flow velocities are high (> 0.5 m/s) and infragravity related bed shear stresses are low, and it is episodic when these stresses are high and mean flow velocities are low (< 0.5 m/s).

To investigate the dependence of these findings on island geometry and hydrodynamic forcing, the phase resolving numerical model SWASH was used (Chapter 4). Results suggested that the sand transport in the shoaling and surf zone was dominated by short and infragravity stirring and transport. At the crest and further landwards, mean flow transport was most important, while wave stirring was sharply reduced after the crest once most waves had broken. Sand transport was increased for steeper compared to gentler slopes, since wave dissipation was less. Results further indicated that the transport over the crest and the submerged island depend on the water-level gradient and the offshore wave forcing which determined the wave set-up at the beach crest. This is in agreement with the observations. In the simulations, the transport was generally landwards directed or close to zero, again in agreement with the observations, with the exception when small offshore wave forcing coincided with extremely elevated water levels in the basin (here 0.55 m higher than on the ocean side). An increase in the island-top slope toward the back barrier, as well as an increase in island width, reduced the mean flow transport, suggesting that in addition to back barrier processes, such as water levels and offshore wave forcing, the island geometry can be important for sand transport processes.

Samenvatting

Barrière-eilanden of Waddeneilanden zijn meestal laaggelegen, smalle eilanden van zand met een oriëntatie min of meer parallel aan de kustlijn van het vasteland. Ze beschermen de kust van het vasteland tegen stormen en creëren getijbekkens, ondiepe lagunes en moerassen tussen de eilanden en het vasteland. In het Waddengebied van Nederland, Duitsland en Denemarken markeren de eilanden de grens tussen Noordzee en Waddenzee. De Waddenzee is opgebouwd uit een serie van aaneengesloten getijbekkens met getijgeulen, platen, slikken en kwelders. De eilanden zelf worden gekenmerkt door belangrijke natuurlijke ecosystemen met o.a. stranden, duinen en kwelders met een grote biodiversiteit. De stijging van de zeespiegel vormt echter een directe bedreiging voor het voortbestaan van barrière-eilanden en het overleven van deze eilanden zal in sterke mate worden bepaald door het vermogen om zand op te nemen en/of langzaam landwaarts te migreren. Grootschalige morfologische veranderingen van eilanden kunnen optreden tijdens storm en daaraan gerelateerde overstroming van de eilanden en de afzetting van sediment. Alhoewel barrière eilanden een grote mate van natuurlijke dynamiek vertonen met vaak een landwaartse en kustlangse migratie is deze dynamiek op tal van plaatsen in de wereld aan banden gelegd. Zo ook langs de Nederlandse Waddenkust waar stuifdijken langs de Noordzee – een stelsel van langgerekte kunstmatige voorduinen – het transport van water en zand vanuit Noordzee naar de eilanden blokkeert.

Om het effect van de stijgende zeespiegel te compenseren, wordt in Nederland overwogen om (nieuwe) openingen te maken in de bestaande stuifdijken. Op deze wijze kan het landwaartse transport van zand worden hersteld en krijgen eilanden de gelegenheid om mee te groeien met de zeespiegel. Vooralsnog is echter onvoldoende bekend over de werking van de verschillende hydrodynamische en zandtransport processen tijdens storm om hier met zekerheid uitspraken over te kunnen doen. Zo leven er belangrijke vragen op het gebied van de grootte en richting van de zandtransporten tijdens storm als een deel van het eiland wordt overspoeld door water van brekende golven (overwash) dan wel volledig overstroomt (inundatie).

Doel van deze studie is het bestuderen van de waterbeweging en zandtransportprocessen tijdens storm op en over een Waddeneiland, mede onder invloed van de morfologie van het eiland en de processen in de Waddenzee. De bestaande kennis op gebied van overwash en inundatie is met name opgebouwd door onderzoek in de Verenigde Staten. Maar de resultaten van dit onderzoek zijn niet direct vertaalbaar naar de kust van de Waddeneilanden. Zo kunnen getijcondities en golf- en stormklimaat aanzienlijk van elkaar verschillen. Maar ook bestaan er belangrijke verschillen in morfologie tussen de eilanden. Daar waar de Waddeneilanden veelal breed en relatief kort zijn, zijn de barrière eilanden in de VS vaak langwerpig en smal. Deze verschillen in hydrodynamische en morfologische condities zijn naar verwachting ook van invloed op de werking van overwash en inundatie op de Waddeneilanden en daarmee het vermogen om zand in te vangen. Ook kan worden vastgesteld dat goede veldmetingen van processen tijdens storm maar zeer beperkt voorhanden zijn ten gevolge van de extreme, hoog-energetische condities.

In dit proefschrift zijn de hydrodynamische en zandtransportprocessen onderzocht die optreden tijdens (gedeeltelijke) inundatie van een Waddeneiland. In het kader van het onderzoek zijn een reeks van gedetailleerde veldmetingen van hydrodynamica en zandtransport uitgevoerd tijdens extreme stormcondities in een dwarsraai van Noordzee tot Waddenzee over de oostpunt van het eiland Schiermonnikoog. De mate waarin de geometrie van een eiland in combinatie met de hydrodynamische processen van invloed is op de zandtransporten, is vervolgens nader onderzocht met een numeriek model.

De hydrodynamische studies laten zien dat overstromingsdieptes ter hoogte van het hoogste punt in het dwarsprofiel (kam: het knikpunt van het strand; engels: berm) varieerden van 0.3 – 1.5 m. Inkomende korte (0.05 – 1 Hz) en lange golven (infragravity waves; 0.005 – 0.05 Hz) verloren weliswaar een belangrijk deel van hun energie door breking in ondiep water (< 0.5 m) maar met name landwaarts van de kam bleken juist infragravity golven een belangrijk aandeel te hebben in het golfveld. Het betrof hier lopende golven die zich in landwaartse richting voortplantten. Daar waar de waterdiepte zeer beperkt was manifesteerden deze golven zich als restgolven met een steil front (bores). De gemiddelde stroomsnelheden ter plaatse van de kam en tijdens vloed bereikten waarden van 0.2 – 1.2 m/s in landwaartse richting. In een beperkt aantal gevallen werd tijdens afgaand tij een zeewaarts gerichte stroming – van Waddenzee naar Noordzee – gemeten ter grootte van ongeveer 0.2 m/s. De grootte en richting van de kustdwarse stroming werd bepaald door het verhang in waterstand tussen Noordzeekust en Waddenzee. Terwijl het grootschalige verhang tussen Noordzee en Waddenzee vaak naar de Noordzee was gericht ten gevolge van hogere waterstanden in de Waddenzee werd dit effect vaak volledig overtroffen door het optreden van golfspanning. Brekende golven aan de Noordzeezijde van de kust waren daardoor verantwoordelijk voor een lokale verhoging in de gemiddelde waterstand (“wave setup”) en dit effect genereerde een netto landwaarts gericht verhang en dito stroming.

Het patroon in stroomsnelheden werd ook weerspiegeld in de gemeten netto en over de diepte geïntegreerde, suspensieve zandtransporten. Vooral tijdens opkomend tij werd veel zand getransporteerd en bijna $\sim 80\%$ van het totale zandtransport werd gerealiseerd in de fase voor hoog water. Het transport was bijna geheel in landwaartse richting. Op het moment dat de stroomsnelheden afnamen (< 0.5 m/s) leverden ook infragravity golven een bijdrage aan het transport. De transportbijdrage van korte golven was daarentegen zeer beperkt en van ondergeschikt belang. Incidentele hoge zandconcentraties bleken vooral op te treden onder invloed van de aanwezigheid van infragravity restgolven (bores) die daarbij als drager fungeerden voor hogere, korte golven. De hoge zandconcentraties waren dan ook naar alle waarschijnlijkheid het gevolg van de totale schuifspanning onder invloed van de gecombineerde werking van de gemiddelde stroming, korte- en infragravity golven. Op basis van de observaties was het mogelijk om twee transportregimes te onderscheiden. Voor condities met hoge stroomsnelheden (> 0.5 m/s) en kleine bodemschuifspanningen ten gevolge van infragravity golven, was het transport stromings gedomineerd. In de omgekeerde situatie - snelheden < 0.5 m/s en grotere bodemschuifspanningen door infragravity golven – was er sprake van een episodisch transportregime.

Om de gevonden resultaten nader te onderzoeken en te kunnen relateren aan de geometrie van een eiland en de opgelegde hydrodynamische randvoorwaarden werd het numerieke model SWASH gebruikt. Volgens het model werden zandtransporten in de ondiepe kust- en brandingszone vooral bepaald door het opwoelen en transport door korte en infragravity golven. Rond de kam van het strand en verder landwaarts veranderde dit beeld en was het transport vooral een functie van de gemiddelde stroming. Doordat inmiddels de meeste golven waren gebroken, was de opwoelende werking van de golven hier sterk gereduceerd. De

zandtransporten namen toe naarmate de helling steiler werd omdat golven in die condities minder onderhevig waren aan energiedissipatie in vergelijking met een relatief flauw profiel. Het zandtransport over de kam en het ondergelopen deel van het eiland werd daarnaast in belangrijke mate bepaald door het grootschalig verhang tussen Noordzee en Waddenzee, in combinatie met de energie (= golfhoogte) van de inkomende golfvelden. De inkomende golfenergie bepaalde de wave set-up en daarmee het netto verhang over het eiland; een beeld dat ook uit de metingen naar voren was gekomen. Volgens zowel de modelsimulaties als de metingen was het transport in het algemeen landwaarts gericht of nihil. Alleen indien de waterstand in het bekken substantieel hoger was dan aan de zeezijde (in dit geval 0.55 m verschil) en er sprake was van laag-energetische, inkomende golven kon er sprake zijn van een beperkt zeewaarts transport. Tenslotte kon op basis van de modelresultaten worden geconcludeerd dat een toename in zowel de landwaartse helling – van kam naar achterliggend getijbekken – als de breedte van het eiland zullen leiden tot een beperking van de zandtransporten door de gemiddelde stroming. Dit impliceert dat naast waterstanden en golfcondities ook de geometrie van een eiland van invloed kan zijn op de zandtransporten.

Chapter 1

Introduction

1.1 Context

Barrier islands front approximately 10 % of open ocean coasts (Stutz and Pilkey, 2011). They are commonly low-lying, narrow sandy islands that are parallel to the coastline. Barrier islands play an important role in sheltering the mainland from wave energy and offer protection for marshes and wetlands that fringe the landward side of the islands and the mainland (Stone and McBride, 1998). The area between the island and the mainland, the back-barrier basin, is usually shallow and the islands create bays, lagoons, and intertidal areas which provide rich habitat for a variety of species. A typical example is the Wadden Sea, which stretches from the Netherlands to Denmark (the Dutch part is shown in Figure 1.1) and which is located between barrier islands separating the North Sea and the mainland. The area is on the UNESCO's World Heritage List for its large-scale intertidal ecosystems and its faunal diversity.

However, the projected global sea level rise of 0.28-0.98 m by the end of the 21st century (IPCC, 2013) threatens the existence of barrier islands (Lorenzo-Trueba and Ashton, 2014; Passeri et al., 2018). Their survival will at least partly depend on their ability to accrete sand (grow in height) or to move landward. Naturally, barrier islands are dynamic features which are constantly on the move (transient landscapes). Oftentimes, they migrate landwards due to sand transport by waves and currents, or they move laterally (along the coast) forced by tide-, wave-, and wind-driven currents. Many barrier systems have migrated landward over the last few thousand years through overwash processes, maintaining themselves even as the sea level slowly rose (Eitner, 1996; Oost et al., 2012). This suggests that overwash (water overtops the beach- or dune-crest) and inundation (the area is continuously submerged), which are storm-driven events, could alleviate the effects of sea level rise. However, the morphodynamics on barrier islands in the Wadden Sea are strongly influenced by human intervention. The building of sand drift dikes (sand blown artificial dunes) began in the 17th century on many Frisian islands (Oost et al., 2012) and most barrier islands are now heavily protected against flooding from the North and Wadden Sea. This has led to the loss of dynamic processes, which are important for the local ecology and has threatened plant and animal species that inhabit the islands (Loeffler et al., 2011). Moreover, sand drift dikes are effectively cutting off any sand supplies landward of the dunes which prevents the accretion of sand and the migration of these barriers (Figure 1.2). To allow more mobility of sand in order to counteract the effects of sea level rise, the re-opening of dunes and dikes is considered for uninhabited parts of barrier islands in the Netherlands. However, it is uncertain how the system will respond, since knowledge of hydrodynamic and sand transport processes, such as the amount and direction of the transport, during overwash and inundation in the Wadden Sea region are limited.



Figure 1.1: The Dutch barrier islands are fronting the Netherlands, separated by the Wadden Sea (brownish area). The North Sea is to the North and West. Photo: USGS/ESA.

Many studies on overwash and inundation have been conducted over time, but most focused on barrier islands in the United States. It is unclear if that knowledge is applicable to the Wadden Sea islands, since island geometries and storm forcing differ significantly. Barrier islands in the US, such as those in the Gulf of Mexico or along the coast of North Carolina, are often located in a wave-dominated, microtidal climate (tidal range < 2 m) where mean annual offshore significant wave heights are small (0.8-1 m, Georgiou et al., 2005). Here, barrier islands are primarily elongated and low-lying and island lengths varying from ~ 1 -100 km, while typical widths range between 1 to 3 km, but are often even smaller. For example, the Outer Banks are a 320 km long string of barrier islands along the coasts of Virginia and North Carolina. Most of these islands are 1-4.8 km wide and the highest topography are sand dunes 3-7 m high (Dolan et al., 1985). Hatteras island, part of the Outer Banks, has a length of roughly 80 km and is one of the longest barrier islands. The system in the North Sea, on the other hand, is a mixed-energy wave and tidal regime with a tidal range of about 1.5-2.3 m. Mean offshore significant wave heights in the North Sea range from 0.5 m in the summer to 2 m in the winter (Oost et al., 2012). Most of the islands are drum-shaped and separated by tidal inlets connecting the North Sea and the basins in the Wadden Sea. The island heads are located updrift (at the western end) and are the widest part of the islands, typically 2-3 km, while the barrier length ranges between 10 and 30 km (for a prototype Wadden Sea island see Figure 1.3). Washover complexes (gaps in the dunes where sand is deposited during overwash and inundation) are usually found on the smaller, down-drift side of the islands between relatively high (~ 10 m) fore dunes (Hoekstra et al., 2009). The hydrodynamic forcing is also quite different for US and Wadden Sea barriers. In the US, cold fronts, tropical storms and hurricanes can increase wave heights dramatically to 3-4



Figure 1.2: Most of the western part of Schiermonnikoog, a Dutch barrier island, is fronted by a sand dike on the North Sea side, while the eastern side is open to overwash and inundation.

m during frontal conditions (Rosati and Stone, 2009), which in extreme cases exceed 10 m during hurricanes (the maximum recorded was 17 m during Hurricane Katrina). The storm surge also varies in these conditions from 0.3 - 0.4 m during cold fronts to several meters. The maximum recorded storm surge in recent history was 8.5 m during Hurricane Katrina (Georgiou et al., 2005). Large amounts of rainfall contribute to floodings in the basin during hurricanes, and the storm surge ebb after its passing can cause severely elevated basin water levels. In the Wadden Sea, storms caused by low pressure systems in the winter time force wave heights with a maximum of 8-11 m (Oost et al., 2012), but usually range from 4-7 m. Storm surges can severely increase water levels along the coast, with the highest recorded sea levels reaching 3.5-4 m (Hoekstra et al., 2009; Oost et al., 2012). Inundation depths during a storm with an exceedance frequency of one in ten years on the barrier island of Schiermonnikoog in the Wadden Sea resulted in inundation depths of 1.5-2 m in the center and at the basin side of the island (Hoekstra et al., 2009). Wave heights and surge levels are, however, strongly dependent on wind direction due to fetch lengths and the alignment of the basin. A storm with winds from the north-west has maximum impact, while winds from the east can even cause water levels to be lower than normal.

Since conditions in the US and in the Wadden Sea are very distinct, knowledge gained from the study of overwash and inundation in the US can not be applied without verification for Wadden Sea processes. Further, most studies investigated the long-term morphological development or changes before and after storms (e.g. Kahn and Roberts, 1982; FitzGerald

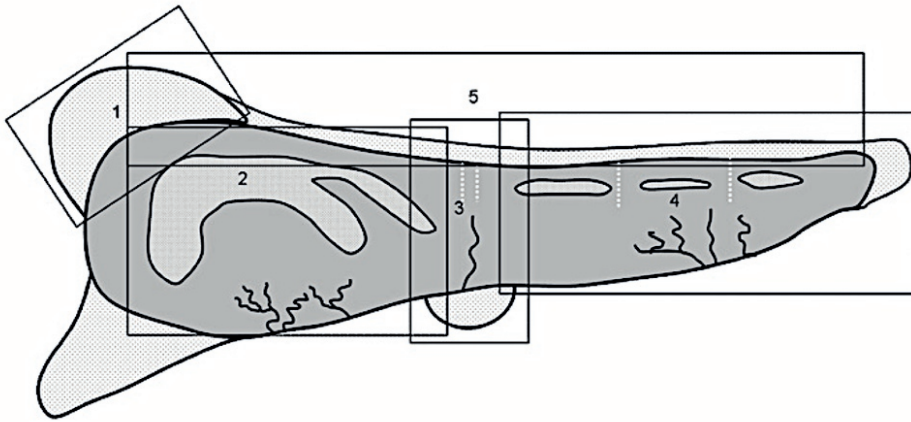


Figure 1.3: The prototype Wadden Sea island consists of: (1) island head, (2) dune arc, (3) washover complex, (4) island tail, (5) beach and shoreface (after Loeffler et al. (2011)).

and Pendleton, 2002; Morton and Sallenger, 2003; Christiansen et al., 2004; Nielsen and Nielsen, 2006; Matias et al., 2008; Long et al., 2014). Generally, few studies include on-site hydrodynamic measurements (e.g. Fisher et al., 1974; Leatherman, 1976; Holland et al., 1991; Hoekstra et al., 2009; Matias et al., 2010; Van der Vegt and Hoekstra, 2012; Sherwood et al., 2014) which are important for the analysis of sand transport processes, and are needed as validation and calibration for numerical models. In addition, the existing knowledge of hydrodynamic and sand transport processes in the surfzone of closed beaches (no-overwash or inundation) might have limitations, since the dynamics in an open boundary system might differ from a closed boundary system. The objective of this thesis is to further our understanding of the hydrodynamic and the resulting cross-shore sand transport processes during the inundation of barrier islands in the Wadden Sea and similar systems.

1.2 Inundation impacts and processes

1.2.1 Storm impact

The impact of storms on barrier island depends, amongst other factors, on the storm surge height, the wave forcing and the dune/island elevation. Sallenger, A. H., Jr. (2000) defined four regimes for barriers impacted by tropical and extra-tropical storms: a.) the swash regime under which run-up is commonly restricted to the foreshore. The eroded sand that is transported offshore during a storm is ultimately deposited again under calm conditions, leading to no net change; b.) the collision regime under which run-up reaching the dune base will erode the dune; c.) the overwash regime when the wave run-up is higher than the dune crest, causing dune erosion and landward sand deposition, and d.) the inundation regime when the barrier is inundated by high water levels caused by a storm surge. Here, the erosional rates can be very high and sand transport can cover distances on the order of a kilometer (Sallenger, A. H., Jr. (2000), and references therein). The large-scale morphological response to inundation includes landward transition, dune lowering and destruction, barrier-

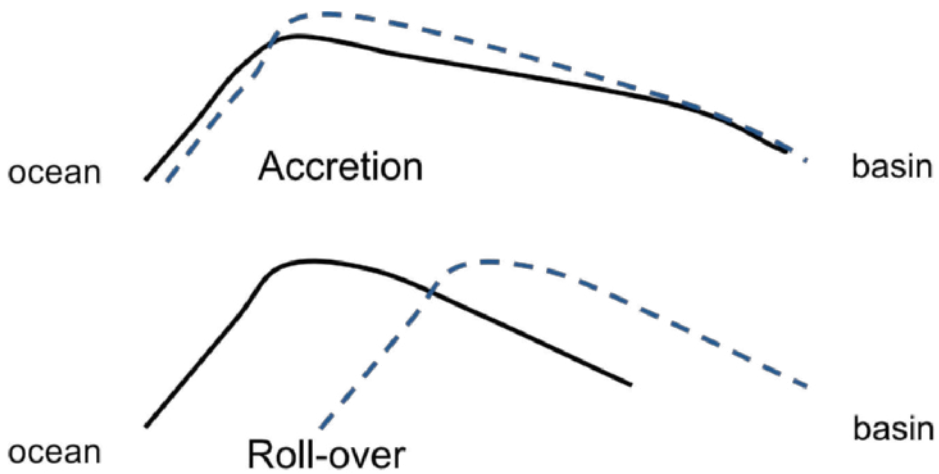


Figure 1.4: Initial barrier island cross-shore profile (black curves), and the morphological response to inundation (dashed lines). Shown here is accretion (top) and roll-over (bottom; after Donnelly, 2007)

disintegration (break-up), accretion (Figure 1.4), and rollover (Donnelly, 2007). From the Sallenger, A. H., Jr. (2000) impact regimes, it can be assumed that barrier islands with high dunes or multiple dune rows will likely first be in the collision regime during storms, and the eroded sand will be transported seawards. Low barrier islands, however, are more likely to experience overwash or inundation under the same water level and wave forcing. In this case, sand can be transported either sea- or landwards from the beach/dune area. Nielsen and Nielsen (2006) showed for a barrier spit in Denmark that the low-lying area of an existing washover fan accumulated sand and had a positive sand budget. On the other hand, the adjacent dune area, where dunes were artificially reinforced, experienced erosion and the local net sand budget was negative, probably due to the loss of sand in an offshore as well as alongshore direction. Since sand is suspended from the bed (stirred) and transported by the wave orbital motion and the mean flow, it is expected that wave- and current - processes are crucial in determining the amount and direction of sand transport, and therefore the barrier response.

1.2.2 Sand transport by waves

Incident, short (0.05-1 Hz) waves contribute considerably to sand stirring and transport in the nearshore. As waves approach the coast, they start to shoal due to the decreasing water depth, meaning that the wave length shortens, while the wave height increases. Non-linear energy transfers cause a change in the wave-shape from a sinusoidal to a skewed shape with high peaks and long elongated troughs (Elgar and Guza, 1985). Further landward in the surfzone, the waves continue to transform into a forward leaning, asymmetric shape with steep wave fronts and more gentle backs. After breaking, the waves propagate toward shore as surf bores, while asymmetry increases and skewness decreases.

This change in shape, and therefore in orbital velocity, is imperative for sand transport. Offshore in deep water, the net transport of sands by waves is zero, since the sinusoidal wave motion causes the same amount of landward as seaward transport. Under skewed waves, the velocity under the crest is larger than under the trough, causing higher bed shear stresses

to mobilize more sand during the landward stroke (e.g. Ribberink and Al-Salem, 1995). In asymmetric waves, fluid acceleration is stronger under the steep leading face and weaker under the gentle back, causing more transport under the crest (e.g. Drake and Calantoni, 2001). Phase-lag effects between the suspension of sand into the water column and the transport during the wave cycle can further affect the transport direction (e.g. Ruessink et al., 2009). Skewed and asymmetric short waves have been shown to contribute significantly to sand transport on closed beaches (e.g. Roelvink and Stive, 1989; Gallagher et al., 1998; Elgar et al., 2001; Hoefel and Elgar, 2003; Ruessink et al., 1998b; Ruessink et al., 2011; Brinkkemper et al., 2018) and in laboratory reef experiments (Bodde et al., 2014; Pomeroy et al., 2015). Reefs are similar to inundation on a barrier island in that the landward boundary is open, so that processes are likely similar.

Generally, infragravity waves (0.005-0.05 Hz) were shown to also be important for sand stirring and transport (Hanes and Huntley, 1986; Hanes, 1991; Russell, 1993; Aagaard and Greenwood, 1994; Houser and Greenwood, 2007; Kularatne and Pattiaratchi, 2014; De Bakker et al., 2016). Video observations by Hoekstra et al. (2009) during inundation of a Dutch barrier island showed that while the incident wave field was composed of short and infragravity waves, the high-frequency waves were dissipated as they propagated across the very wide (> 500 m) beach. Hoekstra et al. (2009) further found that during the inundation of a secondary inlet beach, infragravity wave transport contributed 15-20% to the total transport, while the contribution of short waves was 5-10%. The remaining part was transported by the mean flow, which is discussed below. McCall et al. (2010) showed in a numerical modeling study for Santa Rosa Island, USA, which was impacted by hurricane Ivan, that while the foredune was eroded, the foreshore, back barrier and basin accumulated sand. These processes increased with an increase in wave height and period. In addition, laboratory work suggests that stirring and transport on a reef top is dominated by infragravity waves (Bodde et al., 2014), which agrees with findings that a substantial part of the wave field in this open boundary system consists of infragravity waves (Van Dongeren et al., 2013). De Bakker et al. (2016) found for field observations on closed beach systems that if the ratio of infragravity wave (H_{IG}) to short-wave height (H_{SW}) is relatively small ($H_{IG}/H_{SW} < 0.4$) that the transport direction depends on the correlation of the infragravity waves with the wave group. Offshore, where the infragravity waves are bound to the wave group, the highest short waves are located in the trough of the infragravity waves and stir the sand during the offshore stroke of the infragravity wave. After the start of short-wave breaking, infragravity waves modulate the water depth and short waves stir sand primarily during the onshore stroke of the infragravity waves. On gentle sloping beaches H_{IG}/H_{SW} can be larger than 0.4 in the inner surf zone, which in combination with the undertow can lead to sand suspension on infragravity waves scales (De Bakker et al., 2016) during the offshore stroke. It is, however, unknown if processes will be the same on a barrier island in the Wadden Sea, given the open boundary. It is imperative to gain a better understanding of how waves transform as they propagate across an inundated barrier island in the Wadden Sea, and if wave energy will be dissipated entirely. Further, in a closed beach system infragravity wave energy can be substantially reflected seawards on steep sloping beaches since energy is conserved (e.g. Elgar et al., 1994; De Bakker et al., 2014), but during inundation infragravity waves might continue to propagate onshore, as was found for reefs. While the composition of the wave field and the transformation of waves as they propagate toward the basin are expected to significantly affect sand transport, a thorough understanding of these processes during island inundation is lacking.

1.2.3 Currents and water levels

In addition to waves, sand is stirred and transported by the mean flow. As mentioned in Section 1.2.2, Hoekstra et al. (2009) found the mean flow to contribute 70-80% to the total transport on the beach of an inundated secondary inlet. Mean flow velocities in open boundary systems depend primarily on wave forcing and the difference in water levels between ocean and basin. Symonds et al. (1995) found for a (open boundary) reef system that the radiation stress gradient, caused by the breaking waves, is partitioned between setting up the water level and driving a cross-shore flow before the location of maximum wave set-up. This is usually located around the reef crest, which coincides with the minimum water depth after which wave breaking strongly decreases (or in other words, most wave energy will have been dissipated before the crest). From the crest to the back barrier basin, the mean-flow is then determined by the difference in water levels, which is setting up a pressure gradient that is driving the flow. If water levels are the same in the ocean and in the basin, the flow will be landward directed due to the wave set-up. However, during storms water levels might be significantly higher in the back basin due to high winds, atmospheric pressure, tidal phase lags or wave-driven water fluxes into the bay, or they can be caused by the storm surge ebb after the passing of hurricanes. Higher water levels in the basin compared to the ocean can induce a hydraulic gradient which is seaward directed, forcing an offshore flow. Observations and numerical modeling results for systems in the USA showed significant seaward sand transport and deposition due to the storm surge ebb (Kahn and Roberts, 1982; Goff et al., 2010; Sherwood et al., 2014; Harter and Figlus, 2017). For the Netherlands, video based observations by Hoekstra et al. (2009) also suggested that water levels were elevated in the back-barrier area and that inundation initially occurred from the ocean and the basin side. Model results obtained by Van Dongeren and Van Ormondt (2007) for the same area were initiated with measured water levels during a storm for which water levels also were higher in the basin for the entire high-tide period. Model results predicted initial flooding from both sides, as well. However, a reversal of the mean flow was only predicted 2.5 hours after high tide (for a location in the washover gap close to the North Sea). These results need to be confirmed and generalized, and it is important to determine the strength and direction of mean flow during inundation of a barrier island in the Wadden Sea, and how this will change during the tidal cycle, in order to determine the capacity of barrier islands in the Wadden Sea to capture sand resulting in accretion.

1.3 Research objectives

The overarching aim of this thesis is to gain a better understanding of the hydrodynamic forcing and the resulting cross-shore sand transport processes on intra-wave to tidal time scales during the inundation of barrier islands in the Wadden Sea. To accomplish this, two overarching research questions and several subquestions were defined. The first question addresses the hydrodynamic forcing, while the second question relates to sand transport.

1. *What are the hydrodynamic processes during barrier island inundation?*

Wave- and current processes suspend and transport sand as was discussed in Section 1.2. While the hydrodynamic processes in the nearshore on a closed beach system are relatively well understood, they will likely differ during inundation. In order to evaluate the morphological response of barrier islands in the Wadden Sea to inundation, it is necessary to understand the composition of the wave field. For example, infragravity wave energy can be substantially reflected seawards on steep sloping beaches (e.g. Elgar et al., 1994;

De Bakker et al., 2014) in a closed beach system, but this will probably differ for an open boundary. Also of interest is, how waves transform while they propagate across the island and what the energy dissipation mechanisms are. In addition, currents suspend and transport sand. They can also impact the net transport direction for short (Ruessink et al., 2011) and IG waves (De Bakker et al., 2016), since they add to the bed shear stresses of the orbital motion. Relevant questions that need to be addressed are: what is the direction and magnitude of the mean flow and how is it effected by tidal and local forcing such as elevated water levels in the back barrier basin?

2. *What are the sand transport processes during inundation and how are they affected by variations in island geometry and hydrodynamic forcing?*

Gaining insight into sand transport processes during inundation is important in order to assess the response of barrier islands such as erosion, accretion or landward migration. Here, two subquestions address first the transport mechanism on the inundated island in detail, and second explore how this will change for the entire domain (surfzone to basin) under variations in forcing and island geometries.

a) *What is the relative importance of waves and currents in sand stirring and transport and what is the transport direction?*

Wave energy on the inundated island will probably not be completely lost, and short- and infragravity waves might contribute to sand stirring and transport landwards of the crest. In a closed boundary system, seaward directed sand transport by the undertow can be significant in energetic conditions (Gallagher et al., 1998; Ruessink et al., 1998b). This will probably differ in an open boundary system, where it is expected that the mean flow is driven by wave breaking and water-level gradients as outlined in Section 1.2.3. To gain insight into transport processes, the contribution of waves and currents to the net transport and how this changes with storm- and tidal-forcing will be investigated.

b) *What are the effects of island geometry and hydrodynamic forcing on sand transport?* To generalize the findings from the question above, the foreshore slope, island shape, and the hydrodynamic forcing need to be taken into account. On steep sloping (closed) beaches the wave field is dominated by short wave motion, while on a gentle sloping beach infragravity waves are dominant (de Bakker et al., 2015). Further, the transport direction of infragravity waves can depend on the locations of the short wave relative to the infragravity wave, which will change depending on location in the domain (De Bakker et al., 2016). It is hypothesized that also the island slope from the beach crest to the basin could effect sand transport, since it will modulate inundation depths. The island width, on the other hand, was identified as critical for the landward migration of barriers (Rosati and Stone, 2007). In addition, it is assumed that the magnitude of the transport is at least partly determined by the offshore wave forcing, since it will effect wave velocities and wave set-up. Further, the difference in water levels between ocean and basin effect magnitude as well as the direction of the transport as outlined in Section 1.2.

1.4 Methods and Outline

In order to answer the first research question, field data were collected on the eastern tip of the Dutch barrier island Schiermonnikoog during a 3 month campaign from November

2014 until the end of January 2015. Schiermonnikoog is the fifth major Dutch barrier island (counting from the west), and is almost 18 km long, 3 km wide at its up-drift western end and about 1.5 km wide at its narrow down-drift eastern end where the field area was located. The field site is subaerial but free of vegetation and inundates during storms when water levels are elevated. The maximum height in the cross-shore profile is 1.6 m above mean sea level (MSL), allowing for a higher frequency of flooding than other parts of the island. In addition, the area is open to flooding from the North Sea side as well as from the back-barrier basin.

To measure water levels, flow velocities, and waves, an instrument array was placed roughly cross-shore in a transect from the North Sea to the Wadden Sea over a distance of 1.3 km. The instrument array consisted of three Acoustic Doppler Velocimeters (ADV), sampling pressure and velocity, and ten stand-alone pressure sensors (Figure 1.5). In addition, changes in the transect profile were measured with a Real Time Kinematic Global Positioning System (RTK-GPS).

The first part of the second research (2a) question was again addressed by collecting and analyzing field data at the same location as described above. Between November 2016 and February 2017, an instrument frame was positioned close to the beach crest, equipped with an ADV, an array of optical backscatter sensors, measuring the suspended sand concentrations, and a pressure sensor. In addition, four stand-alone pressure sensors were placed along the transect.

To answer question 2b, a numerical model (SWASH) was used. The phase resolving, non-hydrostatic wavemodel SWASH (Simulating WAVes till SHore) (Zijlema et al., 2011) was chosen since it has been shown to reasonably hindcast hydrodynamic bulk properties and the transformation of infragravity and short waves in the laboratory (Smit et al., 2014; Rijnsdorp et al., 2014) and in the field (Rijnsdorp et al., 2015; Fiedler et al., 2018). The use of the model allows for a better spatial view of the processes from the outer surfzone to the back barrier basin for which it would be otherwise extremely difficult and expensive to collect field observations. It also allows to run a variation of simulations to assess changes in geometry and forcing on sand transport.

In Chapter 2, results are presented that address question 1 (hydrodynamic processes during inundation of a barrier island in the Wadden Sea), and in Chapter 3 findings for question 2a are shown, addressing the sand transport processes on the island. Both chapters are based on field data. Chapter 4 explores simulation results for variations in island geometry and hydrodynamic forcing (question 2b). In Chapter 5 the findings are synthesized and recommendations for further research are provided. Chapters 2, 3 and 4 are based on published peer-reviewed journal articles and therefore there is some overlap between the chapters, particularly in the site descriptions.



Figure 1.5: A stand-alone pressure sensor which was used during the first field campaign (upper panel) and the instrument frame with Accoustic Doppler Velocimeters (ADV) and optical backscatter sensors (OBS) used during the second field campaign (lower panel).

Chapter 2

Observations of waves and currents during barrier island inundation

Based on: Engelstad, A., Ruessink, B.G., Wesselman, D., Hoekstra, P., Oost, A., and van der Vegt, M. (2017), Observations of waves and currents during barrier island inundation. *Journal of Geophysical Research: Oceans*, 122, 3152–3169.

Abstract

Overwash and inundation on barrier islands can transport sediment onshore, leading to vertical accretion. These processes could ensure barrier island growth in times of sea-level rise, but wave and current fields during overwash and inundation are not well understood. Field data of water levels, waves, and currents were collected on a barrier island in the Netherlands to investigate the hydrodynamics during island inundation. Observations show that even in shallow water depths (< 0.5 m) wave energy was not completely dissipated as waves propagated from the North Sea onshore. Additionally, locally generated wind waves entered the field area from the Wadden Sea and propagated offshore. Infragravity waves were an important part of the wave field, particularly onshore of the beach crest. They were observed to be onshore progressive and displayed a bore-like shape when water depths were shallow. Wave breaking was the dominant dissipation mechanism for high-frequency waves as well as for infragravity waves, which is in agreement with prior research on infragravity wave energy dissipation on mild sloping (closed-boundary) beaches. A large-scale offshore directed water-level gradient between the Wadden Sea and the North Sea side, caused by elevated water levels in the Wadden Sea during the storms, frequently drove an offshore flow if it was large enough to exceed the cross-shore gradient due to wave set-up. In addition, elevated water levels in the Wadden Sea decreased current velocities due to a decrease in water-level gradients. This study highlights the influence of back-barrier processes on the hydrodynamics during inundation.

2.1 Introduction

The accretion of sediment on barrier islands is essential for increasing the stability of barrier islands in times of sea level rise. Overwash on barrier islands and island inundation could increase the resilience of barrier islands (Oost et al., 2012) due to the associated onshore sediment transport (Leatherman, 1976; Sallenger, A. H., Jr., 2000). During overwash, water carrying suspended sediments overtops the beach- or dune crest without directly returning to the sea (Donnelly et al., 2006). Once the beach and foredunes are continuously submerged, this process is defined as inundation (Sallenger, A. H., Jr., 2000). Overwash and inundation typically occur during extreme events, such as storms and hurricanes, when water levels are elevated by storm surges and wave set-up. These processes can cause large-scale coastal changes, such as the breaching of barrier islands, island instabilities (Donnelly et al., 2006;

Safak et al., 2016) and the landward transition of islands (roll-over), but it can also lead to vertical growth. The impact of overwash and inundation is particularly noticeable for low-lying, narrow, microtidal barriers in the US, where overwash and inundation events are driven by hurricanes (Fisher et al., 1974; Leatherman, 1976; FitzGerald and Pendleton, 2002; Donnelly et al., 2006). However, overwash and inundation also occur on barrier islands and spits in Europe under mesotidal settings with extratropical storms such as in Portugal, Denmark, Germany, and the Netherlands (Matias et al., 2010; Christiansen et al., 2004; Nielsen and Nielsen, 2006; Hoekstra et al., 2009; Oost et al., 2012; Van der Vegt and Hoekstra, 2012). In mesotidal, mixed energy systems, overwash and inundation can result in net vertical growth of the islands, particularly on the broader and higher barrier islands in the North Sea (Nielsen and Nielsen, 2006; Christiansen et al., 2004).

Because it is inherently difficult to measure wave- and flow-dynamics during storm conditions, not much is known about the hydrodynamic processes. Most of the conducted studies focused on morphological changes before and after storms (Morton and Sallenger, 2003; Nielsen and Nielsen, 2006; Matias et al., 2008), laboratory work (Edge et al., 2007; Matias et al., 2013), and numerical modeling (Van Dongeren and Van Ormondt, 2007; McCall et al., 2010; McCall et al., 2011). Some studies include onsite hydrodynamic measurements (Fisher et al., 1974; Leatherman, 1976; Holland et al., 1991; Hoekstra et al., 2009; Matias et al., 2010; Van der Vegt and Hoekstra, 2012; Sherwood et al., 2014). Generally, there is not much detailed field data on the hydrodynamic conditions during overwash and inundation events. Wave-processes are relatively well studied and understood on a closed surfzone-beach-dune system (without overwash or inundation). However, basic processes such as current magnitudes and directions and wave transformation are less well analyzed and understood during inundation. For example, low-frequency (~ 0.005 - 0.05 Hz) infragravity-wave reflection and return flows, which can be important on closed beaches (Guza and Thornton, 1985; Herbers et al., 1995; Ruessink et al., 1998a; Janssen et al., 2003), may be reduced or absent during overwash and inundation. This could effectively alter the cross- and alongshore wave and current dynamics over the inundated area compared to a closed beach. Of interest is also how the incident wave field transforms over long stretches of shallow water depths on gentle slopes. Video observations by Hoekstra et al. (2009) showed that while the incident wave field was composed of high-frequency (~ 0.05 - 1 Hz) and infragravity waves during an overwash event, the high-frequency waves were dissipated as they propagated across the very wide beach of the barrier island. The observed erosion of the dunes, therefore, was primarily caused by low-frequency waves. Additionally, during the inundation of barrier islands both, waves and water, are able to enter from the sea as well as from the back-basin area. Water levels might be elevated in the backbarrier-basin for example due to winds, tidal phase lags or wave-driven water fluxes into the back barrier area (Sherwood et al., 2014). Observations (FitzGerald and Pendleton, 2002; Hoekstra et al., 2009; Sherwood et al., 2014), and modelling results (Van Dongeren and Van Ormondt, 2007; Sherwood et al., 2014) suggest that higher water levels on the basin side create a hydraulic gradient that is able to drive a flow from the basin to the sea side, initially preventing the flow from the sea to reach the back barrier (Van Dongeren and Van Ormondt, 2007). The hydraulic gradient can then potentially lead to sediment deposition on the seaward side of a barrier island (Sherwood et al., 2014).

In the Netherlands, most barrier islands are heavily guarded by natural dunes and sand drift dikes (sand blown artificial dunes) to protect the islands against storms from the ocean side (North Sea) and the back-barrier basin (Wadden Sea), effectively cutting off any sediment supplies landward of the dunes. At present, the re-opening of dunes and dikes is considered for uninhabited areas. A new paradigm in coastal zone management includes

a more flexible and dynamic behavior of the coast by facilitating natural hydrodynamics and geo-ecological processes wherever safely possible to enhance coastal resilience. However, to evaluate the feasibility and effectiveness of restoring such natural processes, the hydrodynamics during overwash and inundation need to be better understood. The objectives of the present work are to examine the transformation of infragravity and high-frequency waves as they propagate across the inundated part of a barrier island and to investigate the dominant dissipation mechanisms. Further, the effects of water levels, wave- and wind forcing on the cross-shore flow velocities are investigated, and the importance of back-barrier processes is considered. This is done by analyzing a hydrodynamic data-set, collected in the course of a 3-month field campaign on the Dutch island of Schiermonnikoog. The field site, the instrumentation, and the boundary conditions are described in Section 2.2. In Section 2.3, the data processing and the methodology used to analyze the wave and flow fields are introduced. Section 2.4 presents the results on waves and currents. The limitations of a 1-D approach, the similarities of wave processes for open and closed boundary systems, and the importance of the back-barrier basin are explored in Section 2.5. Finally, conclusions are given in Section 2.6.

2.2 Data collection and boundary conditions

2.2.1 Field Site

Field data were collected on the eastern tip of the Dutch barrier island Schiermonnikoog (Figure 2.1) during a 3-month campaign from November 2014 until the end of January 2015. Schiermonnikoog is part of a barrier island chain fronting the coasts of the Netherlands and Germany (Figure 2.1). These barrier islands separate the North Sea from the Wadden Sea (the back-barrier basin). Schiermonnikoog is almost 18 km long, 3 km wide at its up-drift western end and about 1.5 km wide at its narrowest down-drift eastern end. The eastern end of the island is still growing and has, in fact, grown ~ 3 km towards the east since 1982 (Loeffler et al., 2011). The mean offshore significant wave height is 0.5-1 m in the summer (April to October) and 1-2 m in the winter (October to April), while significant wave heights during storms can reach 8-11 m during north-westerly winds (Oost et al., 2012). The system is mesotidal, mixed-energy and tide-dominated, with a tidal range of ~ 1.5 -2.3 m. The tidal wave propagates towards the east. Storm surges can significantly increase water levels along the barrier islands and the coast, potentially leading to severe flooding of unprotected areas. The highest recorded set-up of water levels during storm surges was ~ 3.5 -4 m (Hoekstra et al., 2009; Oost et al., 2012). The field site is subaerial but free of vegetation and inundation only occurs during storms when water levels are elevated. The coastline is aligned ~ -10 degrees with true East, and the area is approximately alongshore uniform for at least one kilometer on both sides of the instrument transect. However, a tidal inlet channel is situated ~ 1.5 km to the east. The maximum height in the cross-shore profile is ~ 1.6 m above mean sea level (MSL) (Figure 2.2), allowing for a higher frequency of flooding than in other parts of the island. In addition, the area is open to flooding from the North Sea side as well as from the back-barrier basin.

2.2.2 Instrumentation

To measure water levels, flow velocities and waves, instruments were placed roughly cross-shore (Figure 2.1) at 0.1-0.2 m above the bed. The instrument transect stretched across the island from the North Sea to the Wadden Sea over a distance of ~ 1.3 km (Figure 2.2). The instrument array consisted of 3 instrument frames, each equipped with an Acoustic Doppler



Figure 2.1: Barrier islands fronting the coasts of The Netherlands and Germany. The Wadden Sea encompasses a series of back-barrier basins between the islands and the coast. The field site (marked by the orange squares) was located on the eastern tip of the barrier island Schiermonnikoog.

Velocimeter (Nortek vector, cabled version), sampling pressure and velocity continuously at 16 Hz. An additional pressure sensor (Ocean Sensor System Wave Gauge, type OSSI-010-003C) was collocated to the Acoustic Doppler Velocimeter (ADV) at the Wadden Sea (labeled P9 in Figure 2), because of a potential drift in the ADV-pressure offset. In addition, nine stand-alone pressure sensors (also Ocean Sensor System Wave Gauge, type OSSI-010-003C) were placed along the instrument-transect (labeled P1-P8 and P10 in Figure 2.2). All stand-alone pressure sensors sampled continuously at 10 Hz with an accuracy of ~ 1 mbar. The transect profile and the height of the instrument locations were measured with a Real Time Kinematic Global Positioning System (RTK-GPS) with an accuracy of ~ 0.02 m in the horizontal and ~ 0.03 - 0.05 m in the vertical. The steepest slope of the profile is less than $1/100$ ($0.9/100$ between P1 and P2), while the highest point of the profile (~ 1.6 m) was just north of P4. Grain sizes were analyzed from sediment samples collected at the center ADV (median grain size of $203 \mu\text{m}$) and the Wadden Sea ADV (median grain size of $199 \mu\text{m}$).

2.2.3 Boundary conditions

Storm conditions with wind speeds ranging from 12 - 19 m/s and local wind directions from SW to NW (Table 2.1), measured at the offshore station Wierumergronden, caused water levels to increase (Table 2.1) and flood the field site. This led to 11 inundation events at the field site during the observational period. Inundation of the field site only took place during high tide, and the overwash regime was limited to a short period of time during the rising tide until the field site was inundated. Here, each flooding is treated as a single event, although the field site might have been flooded multiple times during one storm. Only events dur-

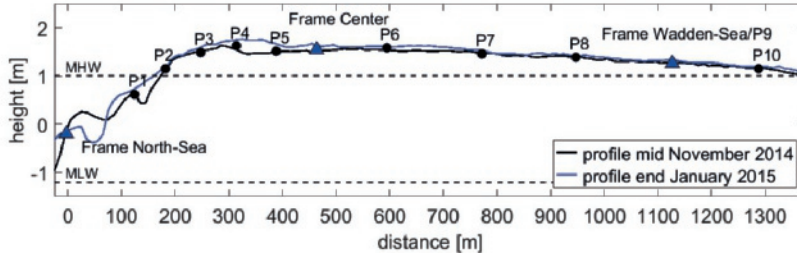


Figure 2.2: The cross-island profiles in mid November 2014 (black curve) and at the end of January 2015 (blue curve) are shown with the North Sea to the left and the back-barrier area (Wadden Sea) to the right. Black dots mark the stand-alone Ocean Sensor System pressure sensors (P1-P10), while the blue triangles mark the instrument frames equipped with Nortek ADVs (pressure and currents). The dashed lines indicate mean high water (MHW) and mean low water (MLW) levels, respectively. The vertical datum is NAP (Dutch Ordnance Datum), where 0 m NAP corresponds to Mean Sea Level.

ing which all instruments were covered with water are considered. Inundation depths at P4 (Figure 2.3), the highest located instrument, were generally shallow (0.3-0.6 m), but reached 1.3 m during the largest event (flooding 9). Offshore significant wave heights, measured at station Schiermonnikoog Noord, ranged from 3.0-5.8 m (Table 2.1) with wave directions persistently from the NW. This is consistent with northerly wind directions offshore (not shown). Significant wave periods ($T_{1/3}$) varied between 8 s and 12 s (Table 2.1). Water levels in the North Sea and in the Wadden Sea were measured by the tidal-stations Huibertgat and Schiermonnikoog, respectively (Table 2.1).

Table 2.1: Boundary conditions for all observed floodings^a

flooding #	date	wind speed [m/s]	wind direction [°]	wave Hs [m]	wave T [s]	wave θ [°]	water level N. Sea [m]	water level W. Sea [m]
1	11.Dec.2014	13.86	243	4.08	10.6	298	1.98	2.05
2	11.Dec.2014	16.73	268	3.78	9.7	293	1.75	1.85
3	12.Dec.2014	12.56	246	4.02	10.0	297	1.75	1.85
4	20.Dec.2014	19.16	260	4.65	10.0	300	1.96	2.03
5	20.Dec.2014	15.15	308	4.97	11.0	319	1.74	1.98
6	02.Jan.2015	17.07	280	4.83	10.5	305	2.03	2.18
7	10.Jan.2015	16.70	243	3.13	9.9	303	1.91	1.95
8	10.Jan.2015	18.90	282	2.96	7.9	284	1.87	1.74
9	11.Jan.2015	17.95	269	5.88	12.1	312	2.65	2.87
10	11.Jan.2015	19.46	284	5.67	11.4	316	1.81	2.05
11	29.Jan.2015	16.24	251	4.38	10.4	300	2.08	2.17

^aIf dates are listed twice, two inundation events occurred on the same day and were separated by a low tide. Wind speeds and directions as well as significant wave heights (Hs) and periods (T), measured by an offshore meteorological station (Wierumergronden) and a wave buoy (Schiermonnikoog Noord), were averaged over one hour at high tide. In addition, the water levels in the North (N.) Sea (measured at Huibertgat) and Wadden (W.) Sea (measured at Schiermonnikoog station) are given, which were also averaged over one hour at high tide.

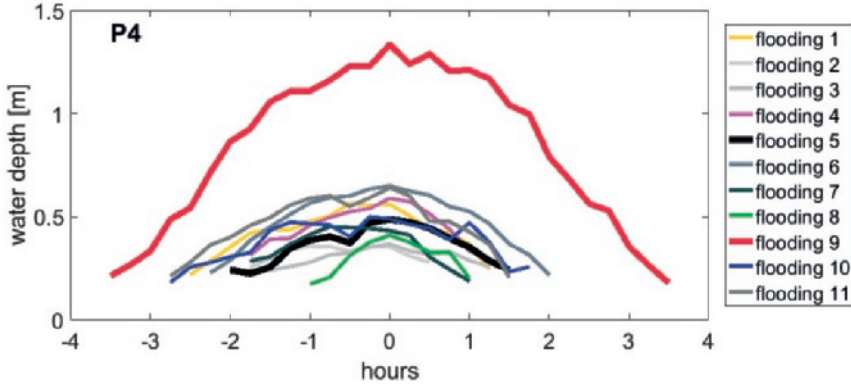


Figure 2.3: All inundation events are shown for the instrument closest to the crest (P4). The time on the x-axis is set relative to high-tide (0 hours). The events marked by the thick black line (flooding 5) and the thick red line (flooding 9) will be used in the analysis and the discussion as examples for shallow and deep floodings, respectively.

2.3 Data analysis

2.3.1 Initial data analysis

Pressure and current velocities were processed in 15 minutes blocks for time series of water levels, wave heights, and cross-shore velocities. Clock-offsets within the stand-alone pressure sensors were linearly interpolated. Data were rejected when pressure sensor coverage was less than 0.04 m to avoid intermittent exposure to air. Pressure data were corrected for air pressure and converted to free surface elevation using linear wave theory. The free surface elevation was then lowpass (0.005-0.05 Hz) and highpass (0.05-1 Hz) filtered, after which wave heights were calculated as four times the standard deviations of the filtered surface elevations. Additionally, the velocity data were objected to further quality controls following the guidelines by Elgar et al. (2005) and Mori et al. (2007). If more than 10% of the record did not pass the quality control, the block was rejected, otherwise the data were interpolated. Since velocities were only available for a single height, the Karman-Prandtl boundary equation

$$U(z) = \frac{U_{*c}}{K} \ln \frac{z}{z_0} \quad (2.1)$$

was used to estimate the vertical current profile. Here U_{*c} is the current related shear velocity, K is the Van Karman constant (0.41), z is the height of the instrument above the bottom, and z_0 is the roughness length calculated from the median grain diameter. For this, U_{*c} was found from the single point measurements and in turn was used to estimate the velocities at 20 locations between the bed and the surface. Finally, the estimated velocities were averaged. Cross- and alongshore velocities account for the island angle.

Velocity-data from the ADV on the North Sea side were not used, because the instrument was intermittently buried by sand, as was the first stand-alone pressure sensor (P1) on the North Sea side. Burial depths for this ADV pressure sensor and for P1 were visually estimated from the raw data during times when the instruments were not inundated and measured only air- and pore pressure. To account for instrument burial in calculations of the sea surface elevation, the correction factor of Raubenheimer et al. (1998) was used. Because P1 was intermittently buried, the water-level gradient between the North Sea and the

Wadden Sea was calculated between P2 and P10, although using P1 and P10 gave similar results. Generally, water-level gradients were calculated by finite differencing over adjacent pressure sensors as

$$\frac{d\zeta}{dx} = \frac{\zeta(P_{n+1}) - \zeta(P_n)}{L}, \quad (2.2)$$

where ζ is the water level at each instrument, which is the sum of averaged water depths and heights of the instrument location (with respect to MSL), and L is the distance between adjacent instruments. n indicates an instrument closer to the North Sea side whereas $n + 1$ indicates an instrument closer to the Wadden Sea side. For all instruments, the distance to the bed was measured at the beginning and the end of the campaign. The difference between these measurements was linearly interpolated. The largest bed level changes were observed in the zone between the mean high water (MHW) and mean low water level (MLW) and directly onshore of the crest (Figure 2.2).

2.3.2 Wave transformation

To investigate the transformation of infragravity (0.005-0.05 Hz) and high-frequency (0.05-1 Hz) waves as they propagate across the field site, spectral estimates were obtained for one representative shallow flooding (flooding 5) and the deepest flooding (flooding 9). These examples will be used throughout this publication to highlight the influence (or lack thereof) of different inundation depths on wave and current dynamics. Assuming water levels to be approximately stationary around high tide, variance densities were estimated with Welch's method using 1 hour records of sea surface elevations, block lengths of 10 minutes and 5 minutes overlap, resulting in 36 degrees of freedom. Further, the energy flux F was calculated as

$$F = \rho g E c_g \cos \theta, \quad (2.3)$$

where ρ is the water density, g is the gravitational acceleration, E is the variance density and c_g is the group speed in the shallow water approximation \sqrt{gh} , where h is the water depth. Waves are considered to be normally incident to the shoreline so that the mean angle of incidence, θ , is assumed to be 0 degrees. Further, the cross-shore energy flux gradient, $\frac{dF}{dx}$, was estimated through finite differencing over adjacent stations and \bar{F} is the energy flux averaged between adjacent stations. To investigate energy losses (and gains) for high- and low-frequency waves and to relate them to local aspects such as bottom slope and inundation depth without the dependency on the energy in the wave field, the normalized energy flux gradient, or growth rate, κ was used

$$\kappa = \frac{dF}{dx} \frac{1}{\bar{F}} \quad (2.4)$$

for which F was calculated in the low- (0.005-0.05 Hz) and high frequency (0.05-1 Hz) bands.

To gain a better understanding of the dissipation mechanisms, the energy balance equation was considered as

$$\frac{dF}{dx} = S_{dis}, \quad (2.5)$$

where S_{dis} is the dissipation term. While nonlinear energy transfers might be important (e.g. de Bakker et al, 2015), they are ignored for the purpose of this study, as is the generation by wind. Dissipation contains dissipation by wave breaking (D_{br}) and by bottom friction (D_{bfr}) so that

$$S_{dis} = D_{br} + D_{bfr}. \quad (2.6)$$

Wave breaking was estimated following Thornton and Guza (1983) as

$$D_{br} = -\frac{3\sqrt{\pi}}{16} \rho g \bar{f} \frac{B^3}{\gamma^4 h^5} H_{rms}^7, \quad (2.7)$$

where H_{rms} is the root-mean squared wave height, and \bar{f} is the mean frequency. B is a breaker coefficient of $O(1)$ which accounts for different breaker types. The free model parameter γ is given by Ruessink et al. (2003) as

$$\gamma = 0.29 + 0.76 * kh, \quad (2.8)$$

where k is the wavenumber. The mean frequency (\bar{f}), γ , and H_{rms}^7 were calculated in the high- and low-frequency limits. Dissipation due to bottom friction (Thornton and Guza, 1983), calculated also in the above mentioned frequency limits, was estimated as

$$D_{bfr} = -\rho c_f \frac{1}{16\sqrt{\pi}} \left(\frac{2\pi\bar{f}H_{rms}}{\sinh(kh)} \right)^3, \quad (2.9)$$

where the bed friction coefficient c_f was calculated as (Zijlema et al., 2011)

$$c_f = \frac{n^2 g}{h^{\frac{1}{3}}}, \quad (2.10)$$

with the Manning's roughness coefficient n set to 0.0225 (Grunnet et al., 2004).

The onshore propagation of infragravity waves was investigated by establishing the cross-correlations between consecutive instruments after lowpass filtering the time series of sea surface elevations.

2.3.3 Momentum balance

The cross-shore momentum balance was used to investigate how water levels, wave- and wind forcing effect flow velocities. The cross-shore momentum balance is considered over one hour at high tide as:

$$\frac{\delta u}{\delta t} + u \frac{\delta u}{\delta x} = -g \frac{\delta \zeta}{\delta x} - \frac{1}{\rho h} \left(\frac{\delta S_{xx}}{\delta x} + \tau_{botx} - \tau_{windx} \right). \quad (2.11)$$

The terms from left to right are flow acceleration and advection, pressure gradient, wave force, bottom friction and wind stress. Since velocities were only available for two locations, velocities from the center ADV and the Wadden Sea ADV were inter- and extrapolated to P5-P10 so that flow acceleration, advection, and bottom friction could be estimated for these locations (they are not available for P1-P4). For the flow acceleration, $\frac{\delta u}{\delta t}$, the time step was an hour, and $\frac{\delta u}{\delta x}$ was calculated as the difference in flow velocity between adjacent instruments, divided by the distance between these instruments. The water-level gradient $\frac{\delta \zeta}{\delta x}$ was estimated as the difference in the mean water level between adjacent instruments, again divided by the distance between these instruments. Here, the water-level gradient is both the result of the local radiation stress, as well as the large scale difference in water levels between the North and Wadden Sea. The cross-shore component of the radiation stress was calculated in the shallow water approximation as (Longuet-Higgins and Stewart, 1964)

$$S_{xx} = 3/2 E, \quad (2.12)$$

where E is the energy density integrated over the frequency range 0.005-1 Hz. The bed shear stress can be approximated as (Ruessink et al., 2001)

$$\tau_{bot,x} = c_f \rho u \sqrt{(1.16 u_{rms})^2 + u^2 + v^2}, \quad (2.13)$$

where c_f is defined as in equation (2.10) and u and v are the depth-averaged mean cross- and alongshore velocities, respectively. Finally, the cross-shore component of the wind shear stress was calculated from

$$\tau_{wind} = \rho_{air} C_d U_{10}^2; \quad (2.14)$$

where ρ_{air} is the density of air, U_{10} is the wind speed at 10 meter height obtained from the Wierumergronden meteorological station (averaged over an hour), and C_d is the wind drag coefficient calculated as 1.2875×10^{-3} for $U_{10} < 7.5$ m/s (Wamdi Group, 1988) and $(0.8 + 0.065 U_{10}) \times 10^{-3}$ for $U_{10} \geq 7.5$ m/s (Wu, 1982). Calculations of the cross-shore velocity u were done by substituting (2.13) into (2.11) and solving for u . Since the results give two possible solutions (positive and negative), the solution closest to the observation was chosen.

2.4 Results

2.4.1 Waves

Time-series of infragravity and high-frequency wave heights (Figure 2.4) were explored for the shallow and the deep flooding at the North Sea side (P1), the crest (P4), and the Wadden Sea side (P10). Sea-swell wave heights ranged from 0.6-1.2 m during high tide at the North Sea side (Figure 2.4d), and were significantly smaller at the crest (~ 0.15 -0.6 m at P4) (Figure 2.4e) and at the Wadden Sea (~ 0.25 -0.75 m at P10) (Figure 2.4f). Since waves were considerably higher offshore (5 m and 5.9 m for the shallow and the deep flooding, respectively; Table 2.1), it can be assumed that most wave breaking already occurred further seaward of the field site. Interestingly, high-frequency wave heights were higher at the Wadden Sea side compared to the crest, which is especially notable during the deep flooding (thick red line in Figure 2.4) when wave heights were about 0.15 m higher at the Wadden Sea. This was unexpected, since waves were assumed to enter the field site from the North Sea, and substantial increases in wave height due to local wind forcing were thought to be negligible because of the oftentimes westerly wind direction (Table 2.1) and the relatively short fetch. Spectral densities were used to evaluate the increase in wave heights. Shown here are only results for the shallow flooding, since results were similar for the deep flooding. Wave energy around the spectral peak (~ 0.1 Hz), indicating waves from the North Sea (Figure 2.5), dissipated as waves propagated toward the center and was lowest at P5. On the other hand, wave energy in the frequency band ~ 0.2 -0.5 Hz increased between P5 and P10. Spectral directions indicate that waves in this frequency-range were actually coming from the South (not shown) during the shallow flooding. During the deep flooding the velocity range of both ADVs were exceeded, and while unwrapping the data worked well for averages of 15 minutes, the data could not be recovered for reliable spectral directions for this case. The southerly direction suggests that these waves were locally generated in the Wadden Sea and propagated towards the center of the transect. This notion is supported by the wave spectrum from a directional wave rider buoy in the Wadden Sea at Pieterburenwad (to the southeast of Schiermonnikoog) where spectral peaks ranged between 0.25-0.5 Hz for almost all flooding events (not shown). During the shallow flooding, a strong increase in spectral densities is found for frequencies > 0.5 Hz between P5 and P10 (Figure 2.5). For this frequency-range, winds from the NW with speeds of 15 m/s and wave directions from the NW suggest wind wave growth. This growth

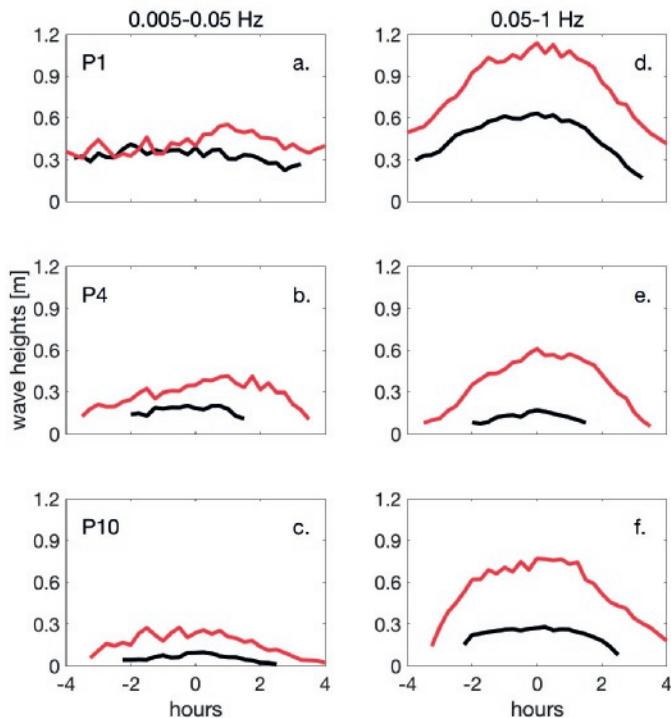


Figure 2.4: Low- (a.-c.) and high-frequency (d.-f.) wave heights at the North Sea side (a. and d.), the crest (b. and e.) and the Wadden Sea side (c. and f.). The red curve shows the deep flooding while the black curve shows the shallow flooding. Note that vertical scales are different for low- and high- frequencies. The time on the x-axis is set relative to high-tide (0 hours).

was absent during the deep flooding since the wind direction was normal (W) to the transect. Infragravity wave heights ranged from 0.3-0.6 m at the North Sea side and ~ 0 -0.3 m at the Wadden Sea side (Figures 2.4a-c) at high tide, and appeared to be depth-modulated by tidal variations (Figures 2.4a-c) like the high-frequency waves (Figures 2.4d-f). Depth modulation of infragravity waves was also noticed in observations on a fringing reef (Pomeroy et al., 2012) and in model results (Van Dongeren et al., 2013). However, infragravity waves heights decreased until about P6 (Figure 2.6b) and then stayed approximately constant. This differs for the sea-swell waves which decreased rapidly with decreasing depths as they propagated onshore, which is consistent with depth-limited breaking (compare Figures 2.6a and c). Due to the slower decay in wave heights, infragravity waves became increasingly important at the center of the transect. Here, they were about equal in height to the high-frequency waves (Figures 2.4b and e), particularly during shallow events.

Correlation coefficients for infragravity waves at consecutive instruments, with average values of 0.9 at the North Sea side, 0.8 right after the crest, and 0.3 at the Wadden Sea side, suggest that these waves were onshore progressive and unidirectional. The correlation was best close to the North Sea and decreased towards the Wadden Sea, coinciding with the decrease in wave heights. In shallow water depths, infragravity waves showed a bore-like shape

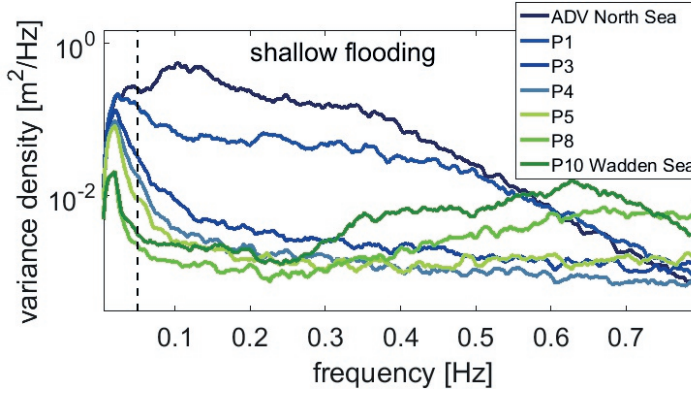


Figure 2.5: Variance densities for the shallow flooding. Results for the deep flooding are similar, but without the increase for frequencies > 0.5 Hz. The dashed black line shows the cut-off between infragravity (0.005-0.05 Hz) and high-frequency (0.05-1 Hz) waves.

(Figure 2.7) onshore of the crest up to $\sim P6$, suggesting that even after the crest part of the energy losses were caused by wave breaking. Tracking individual infragravity waves (see the colored dots in Figure 2.7) between P3 and P5 supports the notion of the onshore progressive nature of the waves. Using the time lag of the marked waves from P3 to P4 and from P4 to P5 and dividing it by the distance between the instruments (resulting in 2.96, 2.72 and

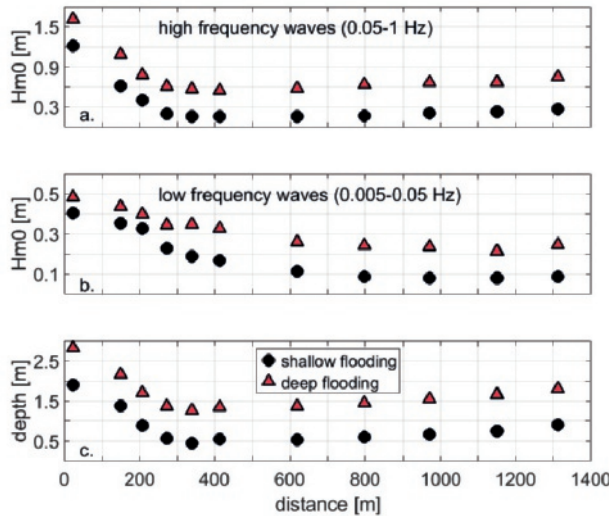


Figure 2.6: Significant wave heights for high- (a.) and low- frequencies (b.) compared to inundation depths (c.) for the shallow (black dots) and the deep flooding (red triangles) averaged over one hour at high tide. The North Sea is to the left of the graph and the Wadden Sea is to the right.

2.62 m/s between P3 and P4 and 2.02, 1.91, and 1.98 m/s between P4 and P5) gives a fairly

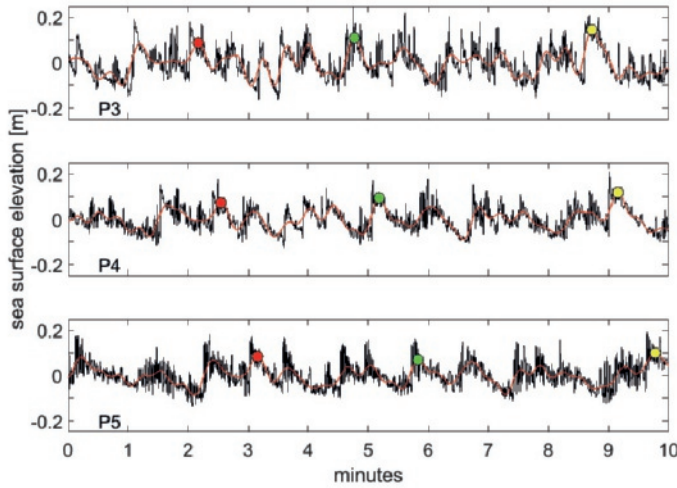


Figure 2.7: Time series of sea surface elevations (black curves) and low-pass filtered (0.005-0.05 Hz) infragravity waves (red curves) at stations P3-P5 (upper to lower panel) over ten minutes at high tide during the shallow flooding. The red, green and yellow dots are tracing single bores from instrument to instrument and are further discussed in the text.

good agreement with the calculated propagation speed (2.18 m/s between P3 and P4 and 2.17 m/s between P4 and P5) in the shallow water approximation \sqrt{gh} .

In the following, we explore the dissimilarity in energy losses for infragravity and high-frequency waves seen above in more detail, and aim to relate them to local aspects such as bottom slope and inundation depths. For this, growth rates were used (Equation 2.4) which are described below as P1-P2 for the growth rates between P1 and P2 up to P9-P10 for calculations between P9 and P10. Generally, negative growth rates indicate dissipation while positive growth rates indicate an increase in wave energy. However, due to the assumption that waves propagate onshore, from approximately P5-P6 towards the Wadden Sea, the positive growth in the frequency range ~ 0.25 -0.5 Hz from approximately P6-P7 to the Wadden Sea represents, in fact, dissipation of wave energy from the Wadden Sea, since waves in this frequency range propagated offshore.

Wave energy dissipation of high-frequency waves was strongest on the North Sea side (Figure 2.8) along the steepest parts of the slope (P1-P2 and P2-P3), indicative of depth-limited wave breaking (Herbers et al., 2000; de Bakker et al., 2015). However, it was also observed on the Wadden Sea side (P7-P8 and P9-P10, indicated by positive growth rates between 0.05 and ~ 0.5 Hz). On the other hand, dissipation of infragravity energy was strongest at P2-P3 and was noticeable until \sim P6-P7. Generally, dissipation was stronger across all frequencies for shallow water depths compared to deeper water depths (with the exception of P6-P7), highlighting the importance of inundation depths for energy dissipation. Note that for frequencies $\sim > 0.5$ Hz during the shallow flooding the positive growth onshore of the crest was probably caused by wind forcing. On the other hand, the observed growth at P1-P2 at higher (> 0.5 Hz) frequencies could have been caused by non-linear energy transfers from the spectral peak to higher frequencies (Herbers et al., 2000; de Bakker et al., 2015).

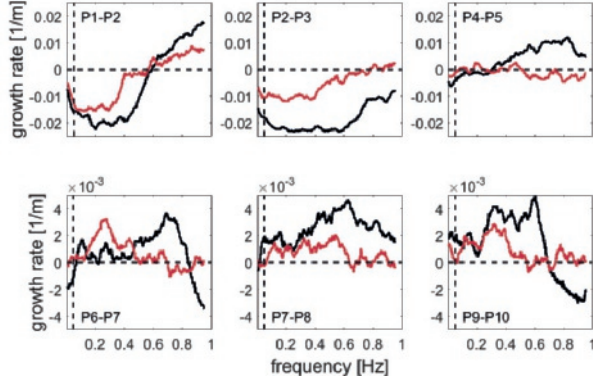


Figure 2.8: Growth rates are compared for the shallow (black curves) and the deep flooding (red curves) at various locations between the stand-alone pressure sensors from the North Sea side (upper left panel) to the Wadden Sea side (lower right panel). The vertical dashed line shows the cut-off between infragravity (0.005-0.05 Hz) and high-frequency waves. Note the different vertical scales.

To isolate the main dissipation mechanisms, dissipation by wave breaking and by bottom friction was investigated (Figure 2.9). The breaker coefficient B (Equation 2.7) was set to 1.5 for the shallow flooding for infragravity and high-frequency waves, while for the deep flooding B was set to 1.8 for infragravity and to 1.0 for high-frequency waves, respectively. B was tuned so that breaking is close to zero at the center of the instrument transect. Wave breaking was the dominant dissipation mechanism (see Equation 2.8 for dissipation by bottom friction) for high-frequency waves before the crest (located at ~ 300 m) and for infragravity waves until $\sim P_5$ (Figure 2.9). From P_7 to the Wadden Sea, dissipation values were too low to determine the dominant dissipation mechanism with certainty and are not shown.

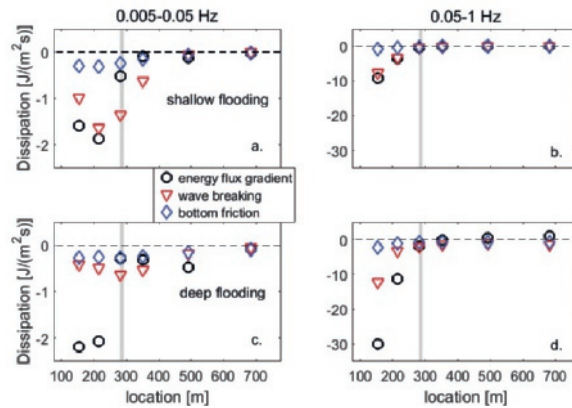


Figure 2.9: Comparison of energy flux gradients (black circles) and dissipation due to wave breaking (red triangles) and bottom friction (blue diamonds) at the center for the shallow flooding (a. and b.) and the deep flooding (c. and d.) for low-frequencies (a. and c.) and high-frequencies (b. and d.). The North Sea is to the left and the Wadden Sea (back-barrier basin) is to the right. The vertical gray line indicates the location of the crest.

Although processes were not captured well at all locations (e.g. the calculated dissipation for the deep flooding was too high at locations after the crest and too low before the crest compared to the energy flux gradient, see also Section 2.5.1, the importance of infragravity wave breaking becomes apparent. This is consistent with earlier results from laboratory studies (Van Dongeren et al., 2007), modeling studies (de Bakker et al., 2015) and shoreline observations (De Bakker et al., 2014).

2.4.2 Water level and current observations

Observations show that water levels were frequently higher in the Wadden Sea compared to the North Sea (positive values in Figure 2.10a). This trend was generally observed after high tide and caused the otherwise onshore directed large scale (North Sea-Wadden Sea) water-level gradients (for a definition see Section 2.3.1) to be seaward directed (Figure 2.10b). On occasions (e.g. floodings 9 and 10) water levels were higher in the Wadden Sea even before high tide (positive values in Figure 2.10a). However, this was only partially reflected in the local water-level gradients between P5 and P6 where the water-level gradient continued to be directed towards the Wadden Sea (negative values in Figure 2.10b). This suggests that the wave set-up around P5, which was induced by wave breaking, prevented locally a reversal of the water-level gradient. During times when the water-level gradients around the

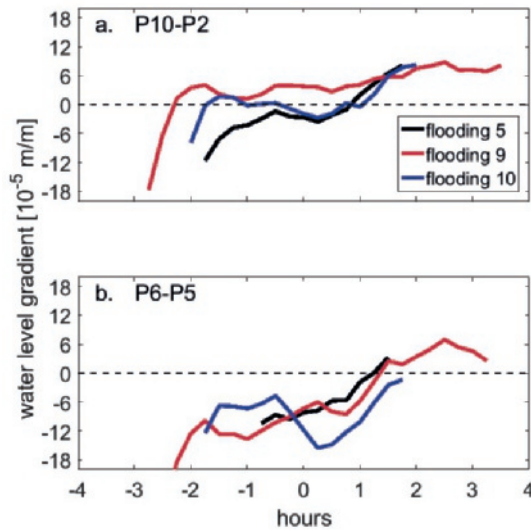


Figure 2.10: Water level gradients between the North Sea (P2) side and at the Wadden Sea (P10) side (a.) compared to water-level gradients between P5 and P6 (b.). Positive values indicate higher water levels at the onshore instrument (the instrument closer to the Wadden Sea side). Negative values indicate higher water levels at the offshore instrument (closer to the North Sea side). The time on the x-axis is set relative to high-tide (0 hours).

center ADV reversed towards the North Sea (positive values in Figure 2.11a), the measured cross-shore currents reversed, too, (Figure 2.11b) with the exception of the shallow flooding (see Section 2.5.3). However, while depth-averaged onshore velocities reached 0.8 m/s at the center ADV during the deep flooding and 0.2-0.4 m/s during other events, seaward directed flows did not exceed 0.2 m/s and were of much shorter duration. For the Wadden Sea ADV, flow direction reversals were less distinct and pressure gradients and currents (Figures 2.11c

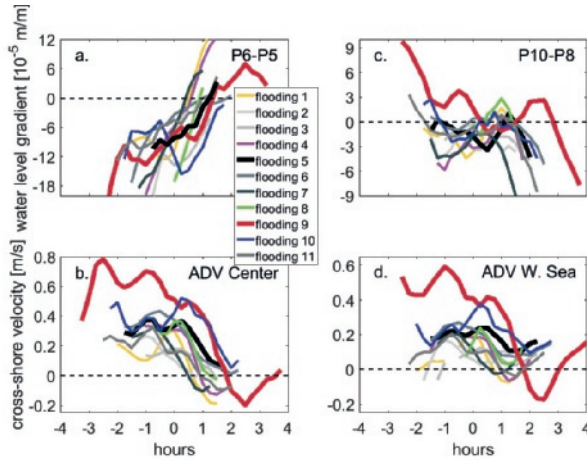


Figure 2.11: Comparison of water-level gradients between P6 and P5 (a.) and currents measured by the center ADV (b.) and the same comparison for the Wadden Sea between P10 and P8 (c. and d.) Positive water-level gradients indicate higher water levels towards the Wadden Sea while negative values indicate higher water levels towards the North Sea. Positive cross-shore currents are directed towards the Wadden Sea. Note that vertical scales are different for the center and the Wadden Sea. The time on the x-axis is set relative to high-tide (0 hours).

and d) were weaker. Here, the onshore directed currents did not exceed 0.2 m/s with the exception of the deep flooding (max ~ 0.5 m/s) and flooding 10 (max ~ 0.35 m/s). Additionally, currents frequently did not reverse even though the local pressure gradient was (briefly) directed offshore (see flooding 5, 8, 9, and 10). In fact, the flow at the Wadden Sea side appears to be closer correlated with the flow measured by the center ADV than with the local water-level gradient (the correlation factors vary between 0.77 and 0.98 for the correlation between the flow measured by the center ADV and the Wadden Sea ADV for all floodings). Variations in water levels at the Wadden Sea side might also have been caused by the influence of a channel located ~ 1 km south of the field site (for a discussion on the limitations of a 1D - cross-shore, see evaluation see Section 2.5.1). Due to the instrument deployment at different heights of the island, it is difficult to say with certainty if the flooding occurred first from the North Sea or from the Wadden Sea (or from both sides at once). However, the seaward direction of the cross-shore currents at the start of floodings at the Wadden Sea indicates for at least three occasions (negative values in Figure 2.11d) that the flooding at the Wadden Sea side occurred from the back-barrier basin.

2.4.3 Momentum balance

The evaluation of the momentum balance (Equation 2.11) suggests that during the shallow flooding, at high tide, the onshore-directed (positive) wave force (due to the radiation stress convergence) and the offshore-directed (negative) pressure force (caused by the water-level gradient) roughly balanced offshore off the crest (Figure 2.12a), suggesting that the offshore directed pressure gradient was induced by the breaking waves in the surfzone. Landward of the crest, the pressure gradient was onshore-directed and approximately balanced by bottom friction, suggesting that the onshore flow after the crest was mainly driven by the pressure gradient. This is supported by a comparison of the mean depth-averaged cross-shore velocities measured by the center ADV with velocities calculated (see section 3.3) from the momentum balance (Figure 2.13a). Contributing also to the forcing of the flow during the

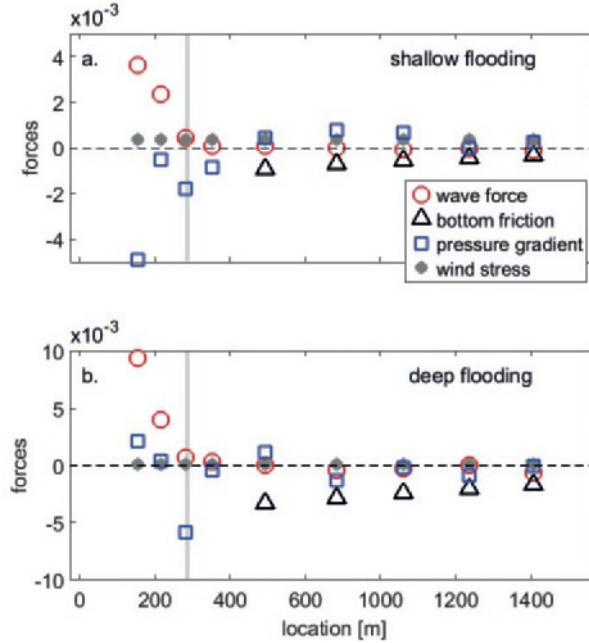


Figure 2.12: Wave force, bottom friction, pressure gradient and wind stress at half-way locations between adjacent pressure sensors during the shallow (a.) and the deep (b.) flooding at high-tide. The North Sea is to the left and the Wadden Sea is to the right. The vertical gray line indicates the location of the crest.

shallow flooding was the wind (15 m/s from 307 degree North) which increased onshore flow velocities by about 0.1 m/s (Figure 2.13a). Even though the wave forcing onshore of the crest was small compared to other forces, omitting the wave force in the calculation of the mean cross-shore velocity u leads to slightly smaller velocities for the onshore flow during the shallow flooding (Figure 2.13a). The wave forcing was dominated by infragravity wave dissipation (Figure 2.14a), while the forcing by high-frequency waves was close to zero at the center. At the Wadden Sea side, on the other hand, wave forcing was dominated by high-frequencies while the infragravity wave forcing was close to zero. While currents were not steady over the one hour at high tide considered here, the acceleration of the flow was small (about two magnitudes smaller than the pressure force), and cross-shore advection is about one magnitude smaller than the pressure force.

During the deep flooding (Figure 2.12b) at high tide, the pressure gradient fluctuated between offshore and onshore directed offshore of the crest. These fluctuations were probably caused by the more energetic conditions and the deeper water depths, allowing for wave breaking around the crest (Figure 2.9). The pressure gradient landward of the center frame, at ~ 500 m, was onshore directed, because the highest water level due to wave set-up during the deep flooding was located around the center frame (~ 450 m). Further toward the Wadden Sea, however, it was offshore directed (with the exception of the location closest to the Wadden Sea), caused by the higher water levels in the back barrier basin (Figure 2.10a). Nevertheless, the cross-shore velocities were onshore directed at the center ADV as well as at the Wadden Sea ADV during high tide (Figures 2.11b and d), causing the bottom fric-

tion to be negative. Obviously, during the deep flooding the forcing did not balance in most locations. A comparison between measured and calculated cross-shore velocities (again at the center ADV) shows (Figure 2.13b) that the onshore directed flow can only partly be explained by local forcing (the pressure gradient). The underestimation of the calculated velocity suggests that either the local pressure gradient is underestimated, or the mean flow is at least partly driven by wave breaking on the slope before the crest or even further offshore (Symonds et al., 1995). Additionally, during the deep flooding the magnitude of the along-shore current exceeded the magnitude of the cross-shore current which could have effected the balance (see Section 2.5.1.) During the deep flooding, the onshore directed (positive)

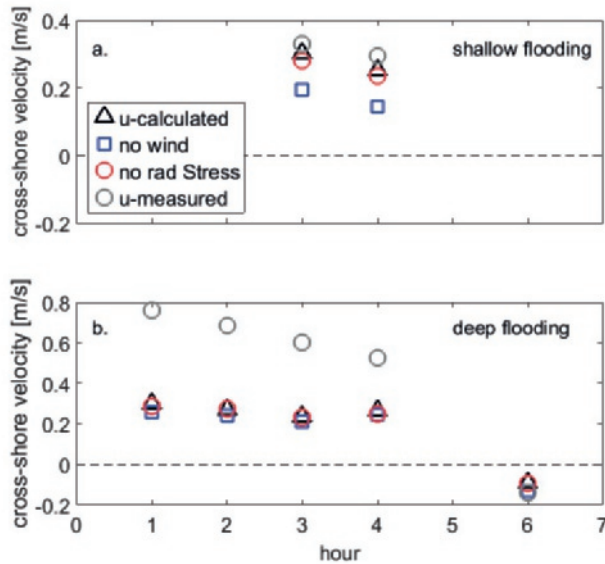


Figure 2.13: Velocities calculated from the momentum balance are compared to calculations without wind forcing (blue circles) and without wave forcing (red circles) for the shallow (a.) and the deep (b.) flooding. Shown are also the cross-shore currents measured by the center ADV (gray circles). Time on the x-axis is 3 hours before and after high tide.

low-frequency (0.005-0.05 Hz) wave forcing was equal in magnitude to the offshore directed (negative) high-frequency (0.05-1 Hz) wave forcing. Since offshore and onshore wave forcing are almost equal, omitting it in the cross-shore velocity calculation has no effect on the total velocity (Figure 2.14b), because u is calculated for the range 0.005-1 Hz. This, however, suggests that in the absence of waves from the Wadden Sea, wave forcing would have had a bigger impact, effectively increasing mean flow velocities. Wind forcing during the deep flooding was small due to the alongshore wind direction (wind speeds of 19 m/s from 260 degree North) and had only a minor impact on the cross-shore velocities (Figure 2.13b). The pressure force was certainly the most important driver of the flow after the crest during the shallow flooding, while during the deep flooding the mean cross-shore velocities might have been strongly enhanced by surfzone processes.

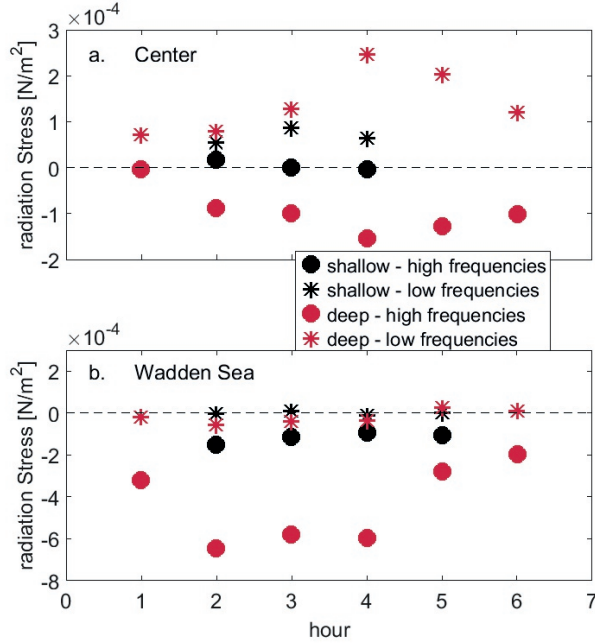


Figure 2.14: Low- and high frequency radiation stresses at the center and the Wadden Sea for the shallow and the deep flooding. Time on the x-axis is 3 hours before and after high tide.

2.5 Discussion

2.5.1 Cross-shore evaluation of wave and current processes

The observed wave and current processes during the inundation of the field site were variable in time and space. For instance, waves entered the field area from the North Sea and the Wadden Sea. Further, current directions were onshore directed before high-tide, but occasionally reversed direction after high tide. We used a 1D cross-shore approach to evaluate these processes, since the alongshore variations of the profile were assumed to be negligible in the vicinity of the instrument transect. However, the field site was bordered by a tidal inlet ~ 1.5 km to the east and another channel ~ 1 km to the South, so that the assumption of along-shore uniform water levels might not hold. Further, the measured current directions often had a strong alongshore component (not shown). A cross-shore evaluation in these conditions might be an over-simplification of the processes in the area and could explain some of the discrepancies between the observed energy fluxes and the calculated dissipation due to breaking and bottom friction, as well as for the mismatch between calculated and observed velocities for the deep flooding. During the deep flooding, alongshore velocities reached ~ 1 m/s at the center frame and 0.8 m/s at the Wadden Sea which exceeded the maximum measured cross-shore velocities of 0.8 and 0.6 m/s at these locations. In comparison, during the shallow flooding the alongshore velocities reached 0.25 m/s at the center frame and 0.1 m/s at the Wadden Sea compared to cross-shore velocities of 0.4 and 0.25 m/s. Additionally, since we are missing observations for the change in alongshore velocities, we ignored the advective acceleration, $v \frac{du}{dy}$. This might explain some of the discrepancies, even so we assume

that this term will be, like the cross-shore advection, rather small. Further, non-linear wave-wave interactions might have caused a deviation of wave energy from cross-shore (Guza and Feddersen, 2012). On the other hand, wave directions for the two cases evaluated here were dominantly cross-shore after the crest, allowing for a reasonable estimate of the wave processes. However, a possible explanation for the discrepancy between the energy flux gradient and the combined dissipation of breaking and bottom friction, which can be seen for the first two locations on the North Sea side during the deep flooding (Figure 2.9c and d), could be that the wave direction was not yet cross-shore directed (the offshore wave angle was 312°). This could have potentially lead to an overestimation of the energy flux gradient. Even though the cross-shore evaluation used here might have some limitations, we assume that the main processes during inundation were approximated well.

2.5.2 Wave transformation without boundaries

Observations of wave transformation during the inundation of the field area showed differences but also some similarities to wave processes on mild sloping (closed) beaches. In the absence of a beach, both infragravity and high-frequency waves were observed to propagate onshore over long stretches of the field site. While wave heights were strongly reduced, the waves did not completely lose all energy (Figures 2.4-2.6). This is, of course, different for a closed surfzone-beach-dune system, where wave energy is either dissipated or reflected. Unfortunately, current observations at the North Sea side are missing, and therefore the extent of infragravity wave reflection cannot be established. However, since the field site has a mild slope, it is assumed (Van Dongeren et al., 2007; De Bakker et al., 2014) that reflection is small or non-existing. Nonetheless, the observation of onshore propagating infragravity waves is in agreement with results by De Bakker et al. (2014), and Van Dongeren et al. (2007) for mild sloping beaches. Additionally, the dominant dissipation mechanism of infragravity wave energy was found to be wave breaking, which is also consistent with observations on mild sloping beaches (Van Dongeren et al., 2007; De Bakker et al., 2014; de Bakker et al., 2015).

Our observations during inundation show similarities with observations over a fringing reef by Pomeroy et al. (2012), for which infragravity waves were also found to be onshore progressive and increasingly important on the reef flat. Additionally, the authors found infragravity waves to decay over the reef flat, but to lose their energy at a slower rate than the high-frequency waves, something also observed in this study. Van Dongeren et al. (2013) used a numerical model to investigate the wave dynamics over the same fringing reef further. Their results suggest that the dissipation of infragravity waves, and consequently their depth modulation, was primarily due to frictional damping. Our observations showed that dissipation across all frequencies was increased during shallow water depths (Figure 2.8), which could have been caused either by an increase in bottom friction or by wave breaking. However, the bore-like shape and the higher breaking rates during the shallow flooding suggest that lower water depths enhanced the steepening of infragravity waves and consequently wave breaking. Of course, due to the nature of coral reefs, frictional dissipation will play a much more important role in these environments than over sandy, submerged barrier islands.

2.5.3 Importance of back-barrier processes

The influence of the back-barrier area on flow processes during overwash and inundation has been reported before. For example, observations of offshore flows, driven by higher water levels in the back-barrier area during ebb tide, were reported by Sherwood et al., 2014 for

a narrow, low-lying barrier island in Louisiana, USA. Model results based on their observations estimated a mean offshore velocity of 0.20 m/s . For the Netherlands, video-based field observations by Hoekstra et al. (2009) in an established washover complex on Schiermonnikoog also suggested that elevated water levels in the back-barrier area (Wadden Sea) drove a flow from the basin side across the island. Model results obtained by Van Dongeren and Van Ormondt (2007) were initiated with measured water levels during a storm in 2006. Water levels were higher in the Wadden Sea than in the North Sea for the entire high-tide period, and the model results predicted initial flooding from both sides, as well. A reversal of the mean flow was predicted at a single location (in the washover gap close to the North Sea) ~ 2.5 hours after high-tide. An explanation for the late reversal of the flow, despite the continuous large-scale (North to Wadden Sea) water-level gradient, could be that wave set-up was high due to large offshore wave heights (8.8 m). In the following, we summarize our findings for the processes that are driving the flow during inundation. Typically, the large-scale water-level gradient is onshore directed before high tide (case 1 in Figure 2.15) due to higher water levels in the North Sea. Additionally, wave set-up (generated by the breaking

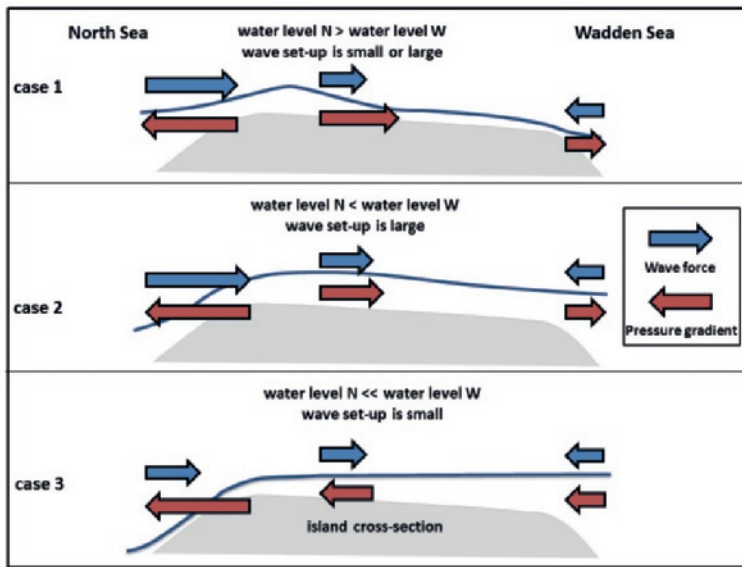


Figure 2.15: Summary of the main forces that drive the flow, such as pressure gradient (red arrows) and wave force (blue arrows), which depend on water levels (blue curves) in the North (N) and Wadden (W) Sea and the strength of wave set-up.

waves) is causing the water level to be highest onshore of the crest. This process creates a pressure force which is offshore directed on the North Sea side and onshore directed at the center and the Wadden Sea. Missing direct measurements, we hypothesize that the flow at the North Sea side will be onshore directed due to momentum and mass conservation. The flow at the center is onshore directed and its magnitude depends on the scale of the driving forces such as pressure gradient, wave force and bottom friction. On the Wadden Sea side, the flow generally follows the flow at the center (Section 2.4.2), even though the wave force is offshore directed due to the offshore propagating waves from the Wadden Sea. Processes are similar if the wave set-up is large, even when water levels are higher in the Wadden Sea

(case 2 in Figure 2.15) than in the North Sea. For example, during flooding the large-scale water-level gradient was offshore directed, while the local water-level gradient was continuously directed onshore (Figure 2.10). In fact, before high tide the gradient towards the Wadden Sea strengthened (Figure 2.11a), which was probably caused by an increase in the wave force. This suggests that the local reversal of water-level gradients (and therefore the pressure force) not only depends on the difference between basin and ocean water levels, but also on the offshore wave forcing. If the forcing is strong enough, it can prevent the reversal of the water-level gradient. The water-level gradient, and consequently the flow, reverses when wave set-up is small compared to the large-scale water-level gradient (case 3 in Figure 2.15). For instance, the water level in the Wadden Sea was higher for the entire time during the deep flooding (Figure 2.10), while the local water-level gradient at the center was still directed towards the Wadden Sea. This only changed about one hour after high tide, when the water levels in the North Sea dropped further, increasing the difference in large-scale water levels.

In addition, the elevated water levels in the Wadden Sea cannot only cause a reversal of the flow, but it is reasonable to assume that the main effect will be a deceleration of the cross-shore velocities since these decrease with decreasing water-level gradients (Figures 2.11a and b). Furthermore, during the shallow flooding, the flow did not reverse even though the water-level gradient locally reversed about an hour after high tide (Figures 2.11 a and b). Calculations of the cross-shore currents suggested that they were enhanced by wind forcing by ~ 0.10 m/s. Together with the small onshore contribution of the wave forcing, it might have prevented the flow reversal.

Processes in the Wadden Sea influenced the current and the wave field in our field area. Of course, the importance of these processes will be regionally different since they depend on local factors such as the size and alignment of the basin, and the tidal inlet(s). The generation of local wind waves in the Wadden Sea is made possible by the size and alignment of the basin which allows for wave growth during westerly and easterly winds.

2.6 Conclusions

Observations of water levels, waves and currents highlight the effect of the back-barrier basin on the hydrodynamics during inundation, as well as the similarities and differences to wave processes on mild sloping beach in a closed surfzone-beach-dune system. High-frequency storm waves and infragravity waves propagated onshore from the North Sea without dissipating all their energy, while waves generated in the Wadden Sea simultaneously propagated offshore. Infragravity waves were of the same magnitude as high-frequency waves onshore of the crest due to the depth-limited breaking of high-frequency waves on the slope. Infragravity wave breaking still continued further onshore on the shallow part of the transect. Generally, infragravity waves were onshore progressive, depth modulated and displayed a bore-like shape in shallow water depths. Wave breaking thus was the dominant dissipation mechanism for high-frequency as well as for infragravity waves, which is in agreement with findings on infragravity wave energy dissipation on mild sloping beaches in a closed boundary system. Water levels in the back-barrier basin were higher than in the North Sea after high tide and occasionally before (e.g. during the deep flooding), which induced a large-scale offshore directed gradient between Wadden and North Sea. However, due to the wave set-up onshore of the crest induced by the wave force, the local gradient at the center was occasionally still onshore directed. On occasions when the large-scale water-level gradient was great enough to overcome the wave set-up, the local water-level gradient was also directed offshore and the currents at the center reversed direction with the exception of the shallow flooding

when wind forcing was strong. The observation of an offshore flow, forced by elevated water levels in the back-barrier basin is consistent with findings of prior research. In addition to a reversal of the currents, elevated water levels in the back-barrier basin reduced the water-level gradient, effectively slowing the onshore currents. We find that the back-barrier basin is strongly influencing the wave field and current dynamics in our field area.

Acknowledgement

We are greatly indebted to Marcel van Maarseveen, Henk Markies, Chris Roosendaal and Arjan van Eijk for their excellent technical support. This work was improved by the constructive comments of three reviewers. We would also like to thank Natuurmonumenten for their assistance during the field work. We thank Tim Janssen and Pieter Smit for fruitful discussions and suggestions. This work is supported by the Netherlands Organisation for Scientific Research (NWO) under contract 850.13.051, as well as by Natuurmonumenten, the National Forest Service (Staatsbosbeheer, SBB), and the Wadden Academy. Daan Weselman is supported by Climate-KIC. The field data can be made available upon request from the first author (anitaengel@gmx.net).

Chapter 3

Sand suspension and transport during inundation of a Dutch barrier island

Based on: Engelstad, A., Ruessink, B. G., Hoekstra, P., van der Vegt, M. (2018). Sand suspension and transport during inundation of a dutch barrier island. *Journal of Geophysical Research: Earth Surface* 123 (12), 3292-3307.

Abstract

Overwash and inundation of barrier islands transport large amounts of sand landwards, which could potentially increase the aggradation of these islands in times of sea level rise. However, not much is known about the detailed processes of sand suspension and transport during inundation. Here, we analyze field data of suspended sand, water levels, waves, and currents which were collected during 5 inundation events on a barrier island in the Netherlands. We found that depth-integrated suspended sand concentrations and cross-shore sand transport showed high variability during and between inundation events at our location, where 80% of the combined transport from all inundation events was completed before high tide. This is primarily caused by variations in cross-shore flow velocities which were strongest (up to 1.2 m/s onshore) before high tide. However, episodically high depth-integrated suspended sand concentrations (defined as $> 2 \text{ kg/m}^2$) were observed on infragravity time scales ($\sim 20\text{-}200 \text{ s}$), suggesting that the contribution of infragravity waves to the combined bed shear stresses of waves and currents was important. High contributions of infragravity waves to the transport coincided with observed bore-like wave shapes, which might partly be attributed to higher short waves riding and suspending sand at the position of the crest. Two transport regimes were thus found to govern the transport during inundation: a flow-driven regime when flow velocities were high ($> 0.5 \text{ m/s}$) and the ratio of infragravity wave and current related Shields numbers was below 0.11 and an episodic regime when this ratio exceeded 0.11.

3.1 Introduction

Overwash and inundation of barrier islands can carry large amounts of sand landwards. Overwash is the overtopping of beaches or dune crests, while during inundation the area between ocean and back barrier basin is continuously submerged (Sallenger, A. H., Jr., 2000). These processes are commonly forced by elevated water levels resulting from storm surges and wave set-up during extreme meteorological events such as storms and hurricanes. The associated morphological responses include erosion and an increase in island instabilities, shoreline retreat and breaching (Donnelly et al., 2006; Safak et al., 2016), but also sand accretion such as gains in subaerial areas (Durán et al., 2016). During Hurricane Ivan on September 26, 2004, for example, washovers (the sand deposits of overwash) of 1.2-1.5 m thickness were deposited on Santa Rosa island, U.S.A. (Donnelly et al., 2006). In fact, overwash can

transport up to several hundreds of m^3 sand per meter beach width landward (Morton and Sallenger, 2003; Nielsen and Nielsen, 2006; Masselink and van Heteren, 2014). Specifically in mesotidal, mixed energy systems, this landwards transport can result in net sand accretion, particularly on the broader and higher barrier islands in the North Sea (Morton and Sallenger, 2003; Nielsen and Nielsen, 2006; Christiansen et al., 2004).

Studies investigating the morphological response to overwash and inundation and the underlying physical processes of sand suspension and transport focused mostly on pre- and post surveys of the affected areas (Morton and Sallenger, 2003; Nielsen and Nielsen, 2006; Matias et al., 2009), laboratory work (Edge et al., 2007; Matias et al., 2013), and numerical modeling (Van Dongeren and Van Ormondt, 2007; McCall et al., 2010; McCall et al., 2011; Harter and Figlus, 2017; Wesselman et al., 2017). Due to the difficulties of collecting field data during storms and hurricanes, onsite studies which combine hydrodynamics and morphological response during overwash and inundation (Fisher et al., 1974; Leatherman, 1976; Holland et al., 1991; Hoekstra et al., 2009; Matias et al., 2010; Van der Vegt and Hoekstra, 2012; Sherwood et al., 2014) are rare. However, field studies are vital to improve insight into sand transport processes during inundation and will be valuable to validate model studies. Models are needed, for example, to assess the risk of barrier island erosion and to estimate the response of barrier islands to sea level rise.

In general, sand suspension and transport is forced by the mean flow and the orbital motion of short (~ 0.05 -1 Hz) and infragravity (~ 0.005 -0.05 Hz) waves, (see Aagaard et al., 2013) for an extensive review. During inundation of gently sloping barriers, wave dynamics show similarities with dissipative beaches where incident storm waves break and infragravity waves dominate the inshore wave field. In contrary to a beach situation, however, not all wave energy is eventually dissipated or reflected as short and infragravity waves propagate onshore across the submerged part of the island and mean flows are predominantly landwards directed. The latter are driven by the wave forces induced by breaking waves and pressure gradients. Pressure gradients are caused by the water-level gradient between ocean and back barrier basin in addition to local wave set-up. Large-scale and local pressure gradients can oppose each other at times (Engelstad et al., 2017, Chapter 2). Further, higher water levels in the back barrier basin than on the ocean side were observed to generate seaward flows (Hoekstra et al., 2009; Sherwood et al., 2014; Engelstad et al., 2017, Chapter 2), which was also found in modeling studies (Sherwood et al., 2014; Harter and Figlus, 2017; Wesselman et al., 2017). In a combined observation-modeling study of barrier island inundation in the Gulf of Mexico, Sherwood et al. (2014) found that the seaward directed water-level gradient resulted in the deposition of a significant amount of sand on the ocean side. A modeling study by McCall et al. (2010) suggested that higher water levels in the back barrier relative to the surge levels in the ocean increased back barrier deposition and reduced deposition in the basin due to a decrease in flow velocity. This is in agreement with simulations by Wesselman et al. (2017) for the Dutch island of Schiermonnikoog. In addition, model results for their study suggested that while currents play a major part in sand stirring, stirring by incident and infragravity waves was found to be important, too.

The objective of this study is to investigate the respective contribution of mean flows and waves on sand suspension and cross-shore sand transport during barrier island inundation. While we expect the dominant force in sand suspension and transport to be the mean flow, it is of interest to examine the contribution of incident and infragravity waves on sand suspension and transport, especially at times when the magnitude of the mean cross-shore current decreases or even reverses. For this, hydro- and morphological data were collected during a 2-month field campaign on the Dutch island of Schiermonnikoog. Depth-integrated sand

concentrations were compared to the forcing by mean flows and waves, while the contributions of incident waves, infragravity waves and mean currents to the sand transport were analyzed. Field site, instrumentation, initial data processing, and boundary conditions is described in Section 3.2. In Section 3.3, the methodology used to analyze the sand suspension and transport processes are introduced. The results, based on six recorded inundation events, are presented in Section 3.4, followed by a discussion in Section 3.5. Finally, the work is concluded in Section 3.6.

3.2 Data collection and boundary conditions

3.2.1 Field Site and Instrumentation

Field data were collected during a two-month campaign (24 November 2016-2 February 2017) on the eastern tip of the Dutch barrier island Schiermonnikoog. Schiermonnikoog is part of a barrier island chain, separating the North Sea and the back barrier basin, named Wadden Sea (Figure 3.1). The island is ~ 18 km long and ~ 1.5 km wide at its narrow down-drift eastern end and is aligned at $\sim -10^\circ$ with true East. The system has a tidal range of ~ 1.5 -2.4 m, and the tidal wave propagates from West to East. Mean offshore significant wave heights range between 0.5 m in summer and 2 m in winter (Oost et al., 2012), while they can typically reach around 7 m during storms. Storm surges can severely increase water levels along the coast and the barrier islands, with the highest recorded water levels reaching ~ 3.5 -4 m above mean sea level (Hoekstra et al., 2009; Oost et al., 2012). The instrument transect



Figure 3.1: Barrier islands are fronting the coasts of the Netherlands and Germany. The Wadden Sea encompasses a series of back-barrier basins between the islands and the coast. The field site (marked by the white line) was located on the eastern tip of the barrier island Schiermonnikoog.

was placed in an area which is approximately alongshore uniform (Figure 3.2), but a tidal inlet is located ~ 1.5 km to the east. This area was chosen as a field site because it is open to flooding from the North Sea and the Wadden Sea side, and the low profile (maximum height of the beach crest is ~ 1.7 -1.8 m above mean sea level) allowed for a higher frequency

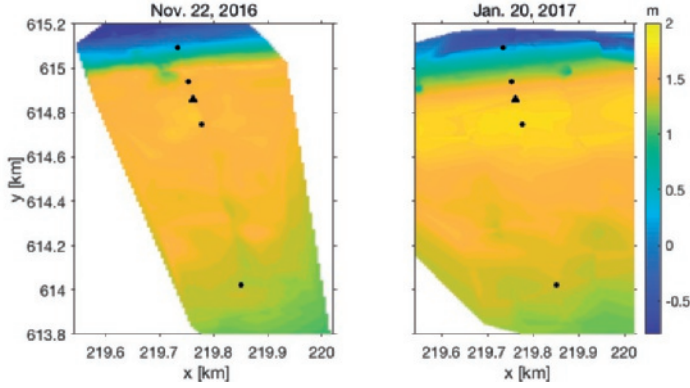


Figure 3.2: Topography of the field site with bed levels at the beginning of the campaign (left panel) and at the end (right panel). The height is given with respect to Mean Sea Level (MSL). Dots mark the stand-alone Ocean Sensor System pressure sensors, while the triangle marks the instrument frame (further described in Figure 3).

of inundation compared to other parts of Schiermonnikoog. The field site usually inundates only during northwesterly storms in conjunction with high tide, leaving it subaerial during low tide. Grain sizes at the instrument locations ranged between $\sim 100\text{--}400\text{ }\mu\text{m}$ with a median grain size of $\sim 200\text{ }\mu\text{m}$. Behind the crest, from $\sim 300\text{ m}$ to 900 m (Figure 3.3), embryo dunes with heights of up to 0.5 m were initially dispersed on the otherwise quite flat surroundings and were covered by sparse vegetation. To measure flow velocities, waves, water levels, and suspended sand concentrations, instruments were placed roughly cross-shore (Figure 3.2) across the island tip from the North Sea to the Wadden Sea over a distance of $\sim 1.1\text{ km}$ (Figure 3.3). Four standalone pressure sensors (Ocean Sensor System Wave Gauge, type OSSI-010-003C) sampled continuously at 10 Hz with an accuracy of $\sim 1\text{ mbar}$ (P1-P4 in Figure 3.3). Two of the pressure sensors were placed on the beach slope (steepness of $1:80$), one after the crest and another one at the Wadden Sea side. An instrument frame, similar to the one deployed by Ruessink (2010), was initially located just behind the beach crest. The location was chosen in an area free of vegetation and embryo dunes such as to not obstruct

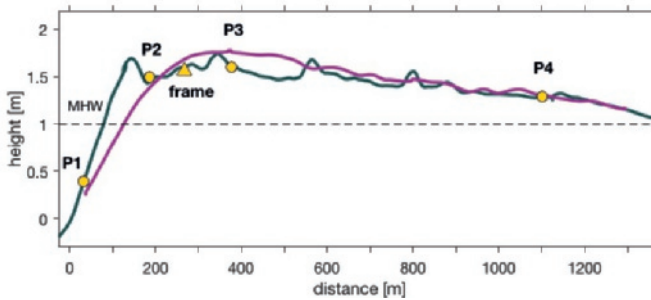


Figure 3.3: The cross-island profiles at the beginning (grey line) and the end (purple line) of the campaign are shown with the North Sea to the left and the back-barrier area (Wadden Sea) to the right. Yellow dots mark the stand-alone Ocean Sensor System pressure sensors. The yellow triangle marks the instrument frame equipped with Sontek ADV (pressure and currents), Seapoint STM (suspended sand), and Aquatec ABS.

the flow. It was equipped with a sideways oriented Sontek Acoustic Doppler Velocimeter Ocean (ADVO) probe, sampling at 10 Hz in bursts of 29 minutes and a break of 1 minute. A vertical array of seven Seapoint Turbidity Meters (STM) measuring suspended sand concentrations, and a Pressure Transducer (PT) measuring nearbed pressure were added to the frame. PT and STMs sampled at 4 Hz. The frame further contained an Aquatec AQUAs-cat1000R Acoustic Backscatter Sensor (ABS) with three transducers (1, 2, and 4 MHz), of which the 1 MHz transducer was used to estimate the distance to the bed, as in Ruessink (2010). The ADVO and ABS sampled in the same burst interval and were triggered externally to synchronize measurements. All instruments on the frame collected data only when submerged to save battery power. The initial distance to the bed was 0.16 m for P1 and varied between 0.07 and 0.1 m for P2-P4. The ADVO was located at 0.29 m above the bed, while the initial distance to the bed for the STMs was 0.06, 0.12, 0.18, 0.25, and 0.32 m.

The transect profile and the height of the instrument locations were measured with a Real Time Kinematic Global Positioning System (RTK-GPS) with an accuracy of ~ 0.02 m in the horizontal and ~ 0.03 - 0.05 m in the vertical at the start and end of the campaign.

3.2.2 Initial data processing

All data were processed in 15-minutes blocks for time series of water levels, wave heights, and velocities. Pressure data were rejected when sensor coverage was less than 0.04 m to avoid intermittent exposure to air. Pressure data were corrected for air pressure and converted to free surface elevation using linear wave theory. The free surface elevation was then low-pass (0.005-0.05 Hz) and high-pass (0.05-1 Hz) filtered, from which infragravity and short wave heights were calculated as four times the standard deviations of the filtered surface elevations. The velocity data were downsampled to 4 Hz to match the sampling rate of the other instruments on the frame and were objected to further quality controls following the guidelines by Elgar et al. (2005) and Mori et al. (2007). If less than 5% of the record did not pass the quality control, the data were interpolated, otherwise the block was rejected. Velocities for locations throughout the water column were calculated by separating the velocities into mean flow, \vec{U}_{mean} and oscillatory components, $\vec{U}_{osc}(t)$, for each 15-minute block and assuming that in the observed shallow water depths the oscillatory components of the velocity were constant throughout the water column. Velocities at depth z were found by using the Karman-Prandtl boundary equation and substituting $\vec{U}_{osc}(t)$ back into the equation

$$\vec{U}_{fit}(t, z) = \frac{\vec{U}_{*c}}{K} \ln \left(\frac{z}{z_o} \right) + \vec{U}_{osc}(t) \quad (3.1)$$

where \vec{U}_{*c} is the current related shear velocity vector, K is the Van Karman constant (0.41), z is the height of the instrument above the bed, and z_o is the roughness length calculated from the median grain diameter. The current related shear velocity vector \vec{U}_{*c} was found from \vec{U}_{mean} of the single point measurements and in turn was used to estimate the velocities at locations between the bed and the surface. Finally, $\vec{U}_{fit}(t, z)$ was depth-averaged to yield $\vec{u}(t)$. Cross- and alongshore velocities account for the island angle.

Instruments were intermittently buried by sand. Burial depths for the pressure sensor P3 were visually estimated from the raw data during times when the instruments were not inundated and measured only air- and pore pressure. To account for instrument burial in calculations of sea surface elevations, the correction factor of Raubenheimer et al. (1998) was used. Data presented in this chapter can be accessed through Engelstad et al. (2018a).

3.2.3 STM processing

The STMs were post-calibrated in a recirculation tank with sand samples collected from the bed at the frame location. Background noise in concentration time series was removed as the 5th percentile of each 15-minute block (Aagaard and Greenwood, 1994; De Bakker et al., 2016; Brinkkemper et al., 2017), and resulting values $< 0 \text{ kg/m}^3$ were set to zero. Substantially higher concentrations at sensors closer to the surface than near the bed suggest the presence of air bubbles. If these were single spikes in the record, the spikes were removed and the gaps were interpolated from adjacent data points. Continuously high values with respect to lower sensors were culled from the data set. If the number of unreliable values exceeded 5 % of data-points in the block, data from the sensor were discarded for the whole 15-minute block. All remaining blocks of sand concentrations were then visually inspected. Records with unreasonably high values, which might have been caused by objects such as e.g. algae, or (partial) burial, were removed. During some inundation events, the bed was highly mobile and varied as much as 0.1 m during a single flooding, causing sensors to be buried or unburied by sand. This led to a varying amount of STMs that could be used for analysis during a single inundation event.

3.2.4 Hydrodynamic conditions

The field site was inundated at least eight times during storms in the observational period. Every inundation that was measured is here treated as a single flooding event, even though several floodings might have occurred during a single storm. Here, five floodings, during which data covered at least 2 hours, were used for analysis. Wind speeds ranged from 11 to 20 m/s with wind directions from W to NW (Table 3.1), which were measured at the meteorological station Lauwersoog (Figure 3.1). Water levels, measured at the tidal stations Huibertgat and Schiermonnikoog, exceeded the threshold of the beach crest ($\sim 1.7 \text{ m}$) during these events and were higher in the Wadden Sea compared to the North Sea at high tide (Table 3.1) and, in fact, for most of the inundation duration. Inundation depths at P2 (Figure 3.4), which was initially located landward of the crest but was eventually located seaward of the crest, ranged between 0.85 and 1.5 m at high tide. Offshore significant wave heights, measured at the buoy Schiermonnikoog in approximately 20 m depth, ranged from 4.5 to 7.4 m during inundations with mean wave periods between 7 and 10 seconds and wave directions from the NW (Table 3.1). Wind data (Table 3.1) in addition to offshore wave and waterlevel data are available from Rijkswaterstaat (RWS), the Dutch Ministry for Infrastruc-

Table 3.1: Boundary conditions for observed floodings^a

flooding #	date	wind speed [m/s]	wind direction [°]	wave Hs [m]	wave T [s]	wave θ [°]	water level N. Sea [m]	water level W. Sea [m]
1	26.Dec.2016	16	270	6.20	8.7	307	2.34	2.52
2	27.Dec.2016	11	300	5.11	8.3	327	1.84	2.19
3	04.Jan.2017	15	310	4.55	7.2	321	2.05	2.16
4	04.Jan.2017	17	330	6.36	9.2	335	1.89	2.35
5	13.Jan.2017	20	330	7.43	10.1	326	2.50	2.92

^aIf dates are listed twice, two inundation events occurred on one day and were separated by a low tide. Wind speed and direction as well as significant wave height (Hs), periods (T) and wave angle (θ) were measured by an offshore meteorological station (Wierumergronden) and a wave buoy (Schiermonnikoog Noord) and were averaged over one hour at high tide. Water levels (wl) in the North Sea (N. Sea, measured at Huibertgat) and Wadden Sea (W. Sea, measured at Schiermonnikoog station) were also averaged over one hour at high tide.

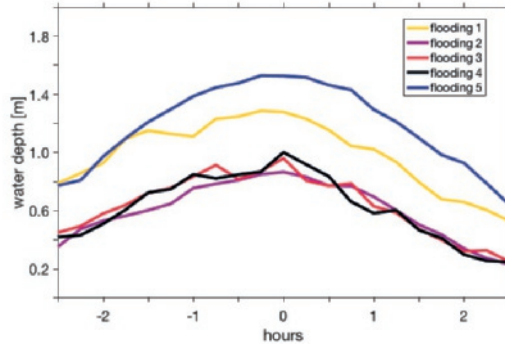


Figure 3.4: Water depths for all flooding events at P2. The x-axis shows the time relative to high tide (0 hours).

ture and Water Management. Waves had already lost most of their energy seaward of the field site, but short waves continued to break at least until the location of the frame, while infragravity waves appeared to be breaking up to m 700 in Figure 3.3. Short wave heights ranged between 0.3 and 0.65 m (Figure 3.5b) at the crest. Infragravity wave heights (Figure 3.5a) were similar to short wave heights and exceeded these during some floodings with low inundation depths (flooding 2 and 4). Depth-averaged mean cross-island flow velocities ranged from 0 to 1.2 m/s and at times reversed to a seaward flow of max -0.2 m/s (Figure 3.6a). The cross-shore velocities at the frame were forced by wave breaking seaward of the frame in addition to large scale and local water-level gradients (not shown) (Engelstad et al., 2017, Chapter 2). While the local water-level gradients were partly a function of the large-scale water levels in North- and Wadden Sea, they were strongly modified by wave set-up. This forced the local gradients to be landward directed, even though the gradients between North and Wadden Sea were predominately seaward directed even before high tide (inferred from measurements at P1 and P4, not shown). Depth-averaged mean alongshore velocities (Figure 3.6b) were of the same magnitude as the cross-shore velocities and even exceeded these at times (e.g. flooding 1 and 5). The high alongshore velocities were probably forced by incident wave angles (inducing pressure and radiation stress variations) and forcing by strong local alongshore winds. Cross-shore and alongshore velocities were markedly reduced after

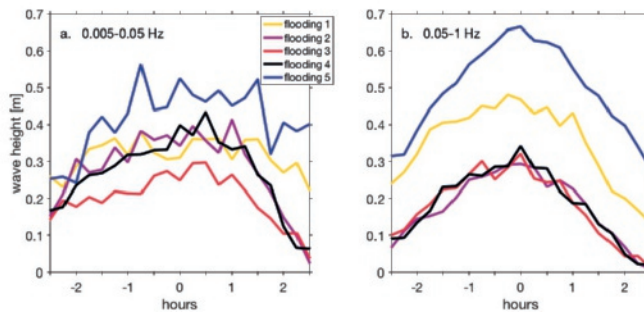


Figure 3.5: Infragravity (a) and short (b) wave heights for all inundation events at P2. The x-axis shows the time relative to high tide (0 hours).

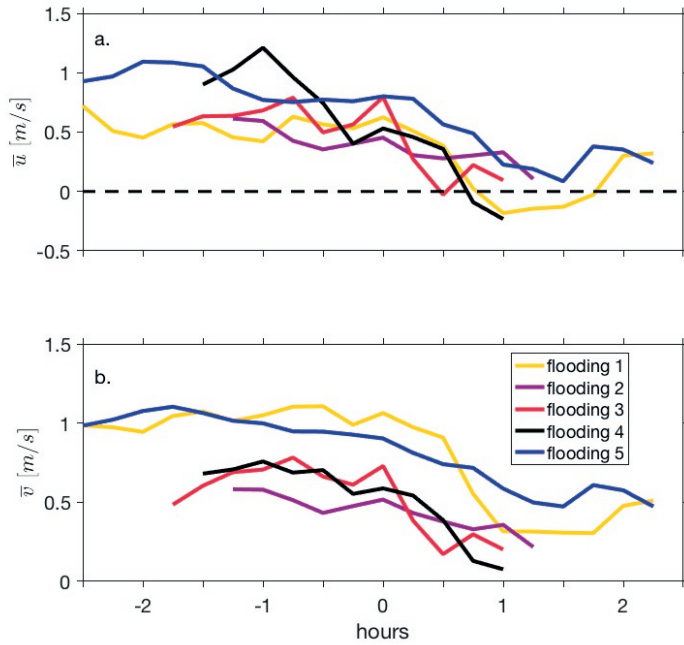


Figure 3.6: Depth-averaged mean cross-shore, \bar{u} , (a) and alongshore, \bar{v} , (b) velocities at the frame. Positive cross-shore velocities indicate landward flow and positive alongshore velocities are directed to the East. The x-axis shows the time relative to high tide (0 hours).

high tide. The reduction in cross-shore velocities can be explained by the falling tide in the North Sea, while longshore velocities might have been reduced by the tidal forcing and/or by a higher water level in the tidal inlet ~ 1.5 km to the East.

As mentioned, the area was sparsely covered with vegetation and embryo dunes at the beginning of the field campaign. While the embryo dunes were flattened out during the inundation events, most of the vegetation survived. The beach crest transitioned landwards during the duration of the field campaign (Figure 3.3). The beach slope changed from 1:80 (initially) to 1:160 (final), while the highest point of the profile (~ 1.74 m above mean sea level (MSL)) was initially located just seaward of P2 but moved landward and was ultimately located at P3 (~ 1.8 m above MSL).

3.3 Analysis of Sand Suspension and Transport

3.3.1 Sand suspension

To account for variations in STM height above the bed with time which can introduce large variations in measured sand concentrations, the varying amount of STMs, and to obtain estimates of the net suspended sand loads throughout the water column, the available concentrations were depth-integrated. For this, the vertical concentrations were linearly fitted to estimate concentrations from bottom to surface, so that instantaneous depth-integrated

suspended sand concentrations, $c(t)$ were calculated from

$$c(t) = \int_0^d C_{fit}(t, z) dz \quad (3.2)$$

where $C_{fit}(z, t)$ are the concentrations estimated from the linear fit. These were integrated from the bed ($z = 0$) to the top of the water column ($z = d$). Time averages of the depth-integrated concentrations will be denoted as C .

We acknowledge that a linear fit might be an oversimplification and that real values could be higher due to an increase in suspended sand concentrations close to the bed. In other words, the linear approach results in a conservative estimate of the sand concentrations which can be regarded as a lower error bound. Using an exponential fit on instantaneous field data is difficult. Greater distances from the bed (> 0.15 m), intermittently low (close to zero) instantaneous values for higher sensors, or higher values for higher sensors compared to the lowest sensor all can result in unreasonable high instantaneous concentrations ($> 10^4$ kg/m³), leading to serious over-predictions. The use of time-averaged (15 minute) concentrations at each sensor allowed to estimate mean concentrations with an exponential fit, here used as an upper error bound for the difference between the two approaches. While the difference between the two fits is small if only 2 sensors are available (transport based on the exponential fit is ~ 1.1 times greater than for the linear fit), the difference is greater for more sensors (on average the exponential fit is 1.5 times greater than the linear fit, in one case up to 2.5 times). We could not detect a consistent bias by using the linear fit in the analysis, since the difference between the two fits varied for time and for floodings. Differences in the volume transport estimates between lower (linear fit) and upper (exponential fit) bounds will be discussed in Section 3.5.2).

The suspension mechanisms can be evaluated using the Shields parameter

$$\theta = \frac{\tau}{(\rho_s - \rho_w)gd_{50}} \quad (3.3)$$

where ρ_s (here taken as 2650 kg/m³) and ρ_w (1025 kg/m³) are the sand and water densities, respectively, g is the gravitational acceleration (9.81 m/s²), and d_{50} is the medium grain size (203 μ m). The Shields parameters related to the mean currents, θ_c , and waves, θ_w , are dependent on the corresponding bed shear stresses τ_c (currents) and τ_w (waves) which are described below following Van Rijn (1993):

$$\tau_c = \frac{\rho_w g |\bar{\bar{U}}_{fit}|^2}{C_z^2} \quad (3.4)$$

with C_z being the Chézy coefficient for smooth turbulent flow conditions and the overbar indicates time averages. To account for the fact that alongshore velocities were of the same order as cross-shore velocities and contributed to the bed shear stresses, $\bar{\bar{U}}_{fit}$ is used. The Chézy coefficient is

$$C_z = 5.75g^{0.5} \log_{10} \left(\frac{12d}{\alpha d_{90} + 3.3 \frac{\nu}{|\bar{\bar{U}}_*|}} \right) \quad (3.5)$$

Here, α was set to 2, d_{90} is the grain diameter representing the 90 % cumulative percentile value, ν is the kinematic viscosity coefficient (here set to 1.55×10^{-6} m²s⁻¹), and $|\bar{\bar{U}}_*|$ is the magnitude of the bed-shear velocity. Instantaneous Shields parameters, $\theta_i(t)$, were calculated

with equations (3.4) and (3.5) by using instantaneous velocities. The bed shear stress due to the wave motion, τ_w , is estimated as

$$\tau_w = 0.25\rho_w f_w U_{osc}^2 \quad (3.6)$$

where the wave related friction coefficient, f_w is defined (Van Rijn, 1993) as

$$f_w = 0.09 \left(\frac{U_w A_w}{\nu} \right)^{-0.2} \quad (3.7)$$

which gives similar results as the wave friction factor defined by Swart (1974). The fluid particle excursion, A_w is described by

$$A_w = \frac{T_p}{2\pi} U_w \quad (3.8)$$

where T_p is the peak wave period and the peak orbital velocity, U_w , is defined as

$$U_w = \pi \frac{H_s}{T_p \sinh(kd)} \quad (3.9)$$

with H_s being the total significant wave height, which is used here in the limit 0.005-1 Hz to account for the importance of short as well as infragravity waves, and k the wave number. θ_w was further separated into the Shields parameter for short, θ_{short} , and infragravity, θ_{ig} , waves by applying equation (3.3) to the short and infragravity wave contributions. The critical Shields parameter for suspension, $\theta_{cr,suspension}$, was found to be 0.08 for the present sand, following Van Rijn (1993). Varying α and ν or using the parametrization for rough turbulent flow conditions altered θ slightly ($\pm 5 - 10\%$), but did not change the general findings.

3.3.2 Sand transport

The instantaneous depth-integrated suspended sand transport rate, $\vec{q}(t)$, is given by

$$\vec{q}(t) = \int_0^d \vec{U}_{fit}(t, z) C_{fit}(t, z) dz \quad (3.10)$$

and the net, time-averaged and depth-integrated, suspended sand transport rate is computed as

$$\vec{Q} = \frac{1}{T_b} \int_0^{T_b} \int_0^d \vec{U}_{fit}(t, z) C_{fit}(t, z) dz dt, \quad (3.11)$$

where T_b is the block duration (15 minutes). To investigate the contributions of waves and mean flow to the suspended cross-shore sand transport, Q_u , the cross-shore component of \vec{Q} , Q_u , can be separated (Jaffe et al., 1984) into the mean (Q_c) and oscillatory, wave transport (Q_w).

$$Q_u = Q_c + Q_w = \int_0^d \overline{U}_{fit}(z) \overline{C}_{fit}(z) dz + \frac{1}{T_b} \int_0^{T_b} \int_0^d U_{osc}(z) \tilde{C}_{fit}(t, z) dt dz \quad (3.12)$$

where U_{fit} is the instantaneous cross-shore velocity (estimated by equation 1), overbars indicate mean and tildes oscillating components. The transport by waves was computed from the co-spectrum (the real part of the cross-spectrum) of velocity $U_{fit}(t, z)$ and suspended sand

concentrations $C_{fit}(t, z)$ (Huntley and Hanes, 1987) at each height z . Due to the almost equal importance of short and infragravity waves (Figure 3.5), the wave transport was further subdivided into the short (0.05-1 Hz) and infragravity (0.005-0.05 Hz) range to investigate their respective contributions. The time-averaged and depth-integrated transport by infragravity waves is denoted as Q_{ig} and by short waves as Q_{short} . We assume that Q_c not only implicitly includes sand suspension by the flow, but that it can include sand brought into suspension by infragravity and short waves, while Q_{ig} can include sand brought into suspension by the short waves if short wave heights were not equally distributed during the onshore and offshore stroke. At the same time, Q_{short} could potentially include sand suspended by infragravity waves and the flow in addition to short wave suspension, albeit this contribution is assumed to be small and only effective for nonlinear short waves. The relative contribution of mean flow, infragravity and short waves to the time-averaged sand transport is found by dividing the respective value by the sum of all absolute contributions ($Q_{all} = |Q_c| + |Q_{ig}| + |Q_{short}|$).

3.4 Results

3.4.1 Suspended sand concentrations

Estimated time-averaged and depth-integrated suspended sand concentrations, C , varied significantly during each individual flooding, as well as between flooding events (Figure 3.7a). C were usually highest at the onset of inundation ($0.4 - 3.8 \text{ kg/m}^2$) and dropped considerably for most flooding events after high tide (Figure 3.7a), but minimum values still reached $\sim 0.1 \text{ kg/m}^2$.

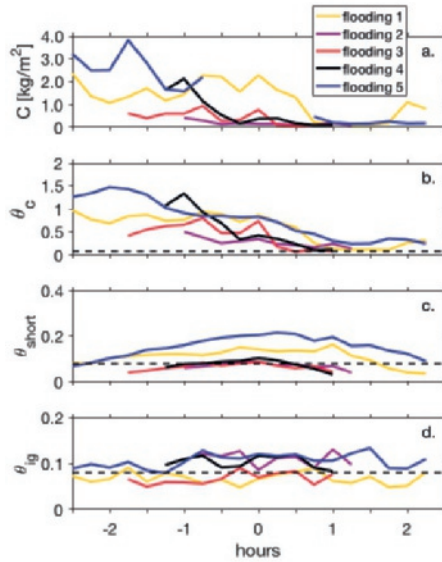


Figure 3.7: Depth-integrated, time-averaged suspended sand concentrations (a) compared to depth-averaged current, θ_c , (b) short-wave, θ_{short} (c) and infragravity, θ_{ig} , (d) Shields parameters. The black dashed line shows the critical Shields parameter for suspension, $\theta_{cr,suspension}=0.08$. The x-axis shows the time relative to high tide (0 hours). Values for flooding 5 around high tide in (a) are missing since STMs were buried. Note the different vertical scales for θ_c , θ_{short} , and θ_{ig} .

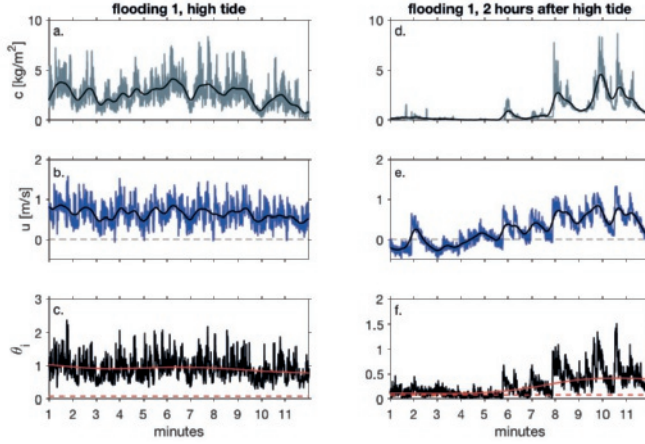


Figure 3.8: Instantaneous depth-integrated suspended sand concentrations (a and d), compared to depth-averaged cross-shore velocities (b and e) and Shields parameters (c and f) shown for flooding 1 at high tide (left column) and at the end of the flooding (right column). The solid black lines shows the low-pass (0.005-0.05 Hz) filtered suspended sand concentrations (c and d) and cross-shore velocities (b and e). The red dashed line in (f) indicates the critical Shields parameter, $\theta_{cr,suspension} = 0.08$ and the red solid line shows the running mean (4 minute window). Note the different vertical scales for θ_{uv} in (c) and (f).

Sand suspension appears to be foremost driven by the current related bed shear stresses (compare Figure 3.7a and b), here expressed by the non-dimensional Shields parameters, θ_c (see Section 3.3.2). The current related Shields parameters, θ_c , were highest (max of 1.5 during flooding 5) at the onset of floodings due to high mean flows (Figure 3.6). They continuously exceeded the critical Shields number for sand suspension, $\theta_{cr,suspension}$ of ~ 0.08 , and were > 0.25 during all floodings before high tide. Wave related Shields parameters were comparably lower, with a maximum of ~ 0.2 for short and ~ 0.13 for infragravity wave Shields parameters. While θ_{short} exceeded $\theta_{cr,suspension}$ for all floodings during high tide, they were highest for short waves exceeding 0.3 m. θ_{ig} for flooding 1 and 3 fluctuated around $\theta_{cr,suspension}$, suggesting that here the infragravity waves contributed less to the sand suspension, owing to either low infragravity wave heights (flooding 3, Figure 3.5a) or larger inundation depths (flooding 1, Figure 3.4).

Time-series of sand suspension show an episodic nature of sand suspension (Figures 3.8 and 3.9). A comparison of instantaneous depth-integrated concentrations, $c(t)$, depth-averaged cross-shore velocities, $u(t)$, and Shields parameters, θ_i , indicate that the suspension of sand was partly driven by short waves (see e.g. the strong, short-period fluctuations in Figure 3.8, left column). Moreover, higher concentrations (here defined as $> 2 \text{ kg/m}^2$) were observed particularly at infragravity timescales (Figure 3.8d and Figures 3.9a and d) during which sand usually stayed in suspension. Suspension events in correlation with infragravity bores showed sudden high instantaneous values of up to 9.5 kg/m^2 which coincided with the crest of bores where Shields numbers were highest. At times, short waves contributed to these high Shields numbers, since depth modulation by the free infragravity waves allow larger short waves to ride on the crest of infragravity waves, while smaller short waves are positioned in the trough. Thus, short waves are enhancing the suspended concentrations under infragravity wave crest further as described previously by De Bakker et al. (2016). Generally, infragravity waves appear to modulate the shear stress of the mean flow (here

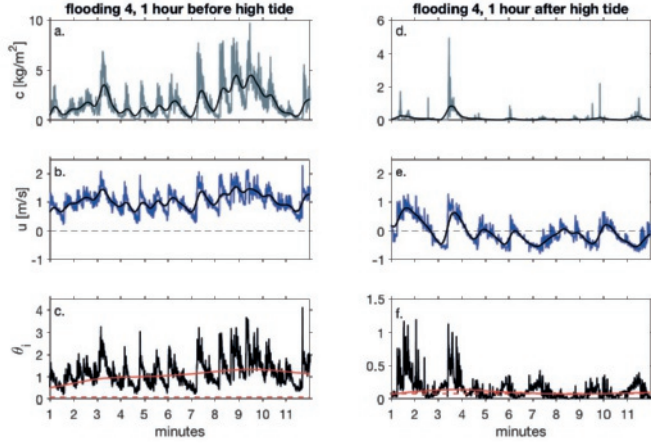


Figure 3.9: Instantaneous depth-integrated suspended sand concentrations (a and d), compared to depth-averaged cross-shore velocities (b and e) and shields parameters (c and f) for flooding 4 at the start (left column) and the end of the flooding (right column). The solid black lines shows the low-pass (0.005-0.05 Hz) filtered suspended sand concentrations (c and d) and cross-shore velocities (b and e). The red dashed line in (f) shows the critical Shields parameter, $\theta_{cr,suspension}=0.08$ and the red solid line shows the running mean (4 minute window). Note the different vertical scales.

estimated by a running mean with a 4 minute window, shown as a red solid curve in Figures 3.8 and 3.9) by enhancing it if the stroke is in the same direction as the mean flow (for example during the onshore infragravity wave stroke, compare Figure 3.9b and c or the offshore stroke, compare Figure 3.9e and f) or by reducing it if the stroke is in opposite directions. At times of low or offshore directed mean velocities, infragravity bores and short waves were not able to mobilize the very high concentrations seen in the presence of high mean flow velocities (see e.g. minute 1 in Figure 3.8d-f and minutes 5-11 in Figure 3.9 d-f). During the mean flow reversal, when short and infragravity waves were of about the same magnitude as an hour before high tide, the Shields parameter repeatedly dropped below the critical value for suspension and sand suspension was at a minimum (Figure 3.9, compare left and right panel). This suggests that the combined components of episodically high wave velocities and mean flow caused the high suspended concentrations.

3.4.2 Sand transport

The total, mean depth-integrated, cross-shore sand transport rate, Q_u , was highest at the start of inundations with a maximum of $\sim 3.8 \text{ kg m}^{-1}\text{s}^{-1}$ for flooding 5 and decreased significantly around and after high tide to values of $\sim 0.05 \text{ kg m}^{-1}\text{s}^{-1}$ (Figure 3.10). In fact, $\sim 80\%$ of the combined transport from all floodings was done before high tide. Not surprisingly, the sand transport was highest for flooding events with high mean flow velocities, such as floodings 1, 4 and 5, and the net transport followed the suspended sand concentrations closely (compare Figures 3.7a and 3.10). The net, depth-integrated, alongshore sand transport, Q_v , was similar or even higher (flooding 1) than Q_u due to the strong alongshore velocities (Figure 3.6). The direction of the depth-integrated total sand transport was almost entirely directed landward and towards the East (Figure 3.10). Mean offshore transport was only observed during flow reversal at times when the suspended sand concentrations and seaward directed velocities were low, so that the transport rate was rather small (maximum

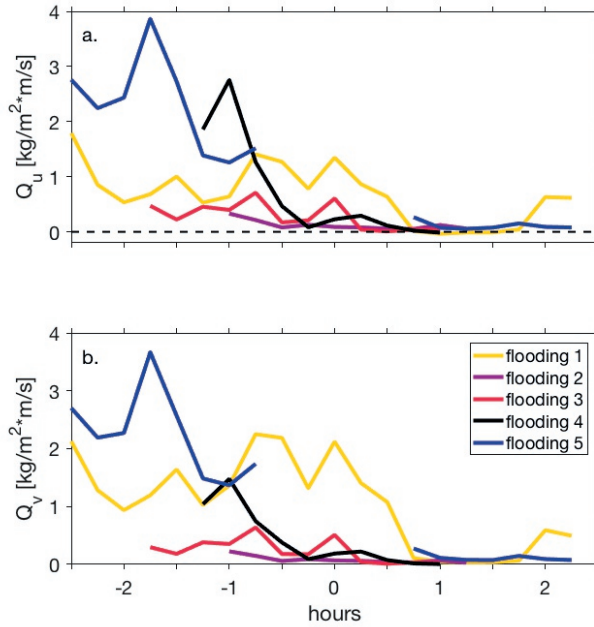


Figure 3.10: The net, depth-integrated sand transport in the cross-shore, (Q_u) (a), and alongshore, (Q_v) (b), direction. Positive cross-shore is landwards, while positive alongshore is approximately towards the East. The x-axis shows the time relative to high tide (0 hours). Values for flooding 5 around high tide are missing since STMs were buried.

seaward transport was $0.03 \text{ kg m}^{-1}\text{s}^{-1}$). Overall, the total sand transport was dominated by the mean flow transport, Q_c , (Figure 3.11) before high tide, which reached a maximum relative contribution of 0.98 during flooding 5. Contributions by infragravity waves, Q_{ig} , increased to > 0.2 when mean flow velocities were roughly $< 0.5 \text{ m/s}$ and reached maximum values of ~ 0.8 during flooding 1 and 2 after high tide. The infragravity transport was generally onshore directed (2 % of it was offshore directed). Contributions by short waves, Q_{short} , to the mean cross-shore transport were overall insignificant before high tide (between ~ 0.001 - 0.03) and increased somewhat after high tide (to a maximum of 0.17). (However, while short wave transport was small, short waves contributed to sand suspension.) When the mean flow was seaward directed, the transport by mean flow and infragravity waves opposed each other with the exception of one occasion during flooding 1 when the mean infragravity transport was also offshore directed. This instant of offshore directed infragravity transport was most likely caused by the fact that the infragravity waves had not developed into a bore-like shape (due to relative deep inundation depths) and short waves were distributed evenly on crests and troughs (not shown). Since in this situation the wave suspension is (more or less) the same under crests and troughs, the mean offshore flow can enhance the offshore-directed transport during the negative infragravity wave phase (De Bakker et al., 2016). On the other hand, when the mean flow was offshore directed during flooding 4, infragravity-bore shapes had developed with larger short waves riding on the crest than in the troughs, causing the transport to be onshore.

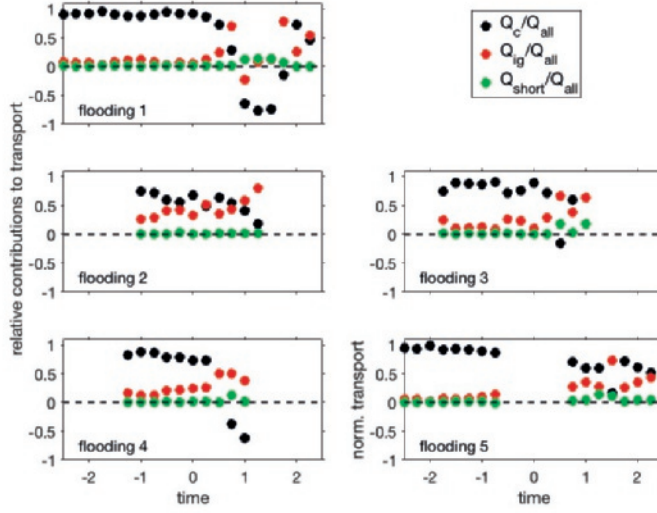


Figure 3.11: The relative contribution of mean flow, Q_c/Q_{all} , (black dots), infragravity, Q_{ig}/Q_{all} , (red dots) and short, Q_{short}/Q_{all} , (green dots) waves. Positive transport is landward, while negative transport is seaward directed. The x-axis shows the time relative to high tide (0 hours). Values for flooding 5 around high tide are missing since STMs were buried.

3.4.3 Episodicity of sand transport

Results in Section 3.4.1 and 3.4.2 suggest that sand transport at the field site was governed by two "regimes". During high mean flows, suspension and transport were largely driven by the mean flow resulting in an almost continuous transport. In low mean-flow conditions the importance of infragravity waves for sand suspension and transport increased and caused episodic transport. To further distinguish between flow-driven and episodic events (on an infragravity scale), we investigated the episodicity of sand transport. For this, the normalized cumulative transport is used since it highlights the importance of infragravity waves in sand transport.

The cumulative depth-integrated sand transport, Q_{cum} , was calculated for every 15-minute block by the cumulative sum of the instantaneous depth-integrated cross-shore transport, q_u , which was then normalized by the (absolute) maximum in cumulative transport for each block, yielding $Q_{cum}/Q_{cum-max}$. Flow driven events are visually assessed for each block and are here defined as $Q_{cum}/Q_{cum-max}$, showing a continuous increase in transport over time on time scales longer than 200 s (infragravity time scale) at least once in one block. Episodic events show sudden increases followed by a flat where the increase in $Q_{cum}/Q_{cum-max}$ is close to zero, indicating that transport by mean flow alone is very small or zero.

Flow-driven events, such as floodings 1 and 5 at the onset of the inundation and flooding 1 and 3 during high tide (Figure 3.12a and b), were characterized by high mean flows (> 0.5 m/s, Figure 3.6) and high current bed shear stresses ($\theta_c > 0.5$, Figure 3.7) while the bed shear stresses caused by infragravity waves were small ($\theta_{ig} < 0.1$). Episodic events, such as flooding 2 during all times or flooding 3 at the start of the inundation, can be observed when $\theta_c < 0.5$ even if θ_{ig} (and θ_{short}) were < 0.1 as for flooding 3 at the start of the inundation. In fact, computations of θ_{ig}/θ_c for all time steps showed that episodic events occurred for

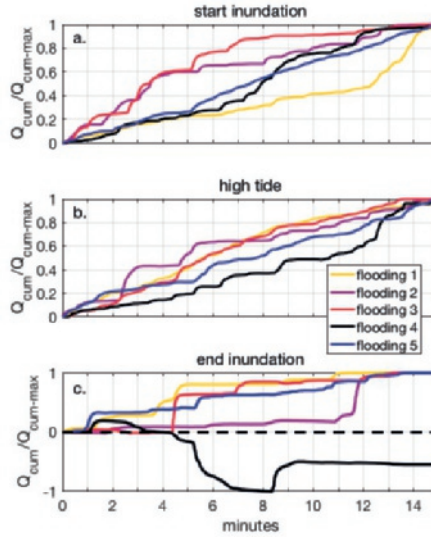


Figure 3.12: The cumulative depth-averaged sand transport at the beginning and end of each individual inundation (a. and c.) and at high tide (b.) for 15 minutes normalized by the maximum of the absolute cumulative transport for the 15 minute block. The beginning and end of each flooding relative to high tide can be seen in Figure 3.10.

θ_{ig}/θ_c above 0.11 (not shown). The episodic nature of the sand transport increased towards the end of all floodings, when the steps got steeper and the flat plateaus longer (Figure 3.12c) due to low cross-shore mean velocities. The exception is flooding 4 during which the flow reversed. Here, the episodic reduction of the seaward directed transport (expressed in less negative numbers than in the time before) suggest that landward directed infragravity transport reduced the net seaward transport, as was already suggested in Section 3.4.2. Visual inspection of $Q_{cum}/Q_{cum-max}$ for every time-step and ignoring times of (mean flow and infragravity) transport reversal, suggest that for all investigated floodings only about half of the time the transport is dominated by the flow.

3.5 Discussion

3.5.1 Profile change and sand transport

Observations showed that during our field campaign the beach and beach crest were eroded, while sand was accumulated landward of the crest. In order to determine how much of the total profile change is explained by the suspended cross-shore sand transport, the profile change was estimated from the dGPS surveys along the instrument array which were done at the beginning and end of the field campaign. The net volume change along the transect was estimated by the difference in height and integrated along the length of the transect and is given per 1 m width. To establish the change landward of the measurement frame, the change in height was integrated between the instrument frame and the Wadden Sea. We assume that all positive changes landward of the frame must have come from sand being transported from the seaward side of the instrument frame, and we assume no gradient in the

alongshore transport in our region. The net total change (increase) in volume between North and Wadden Sea was $\sim 2 \text{ m}^3/\text{m}$ over the whole observational period, suggesting that the net addition of sand to the beach from the North Sea is small during winter storms. Between the instrument frame and the Wadden Sea the volume increased by roughly $60 \text{ m}^3/\text{m}$, while the area between North Sea and frame lost $\sim 58 \text{ m}^3/\text{m}$. Volume changes at the Wadden Sea side were negligible and suggest that no sand was deposited in the Wadden Sea.

The volume of the net cross-shore sand transport across the crest was estimated by the time-integration of the instantaneous sand transport rate, q_u , over the duration of all flooding events and by including two floodings for which the STMs were intermittently located high ($> 0.2 \text{ m}$) in the water column. For these the transport is probably underestimated, but can be used for a rough estimate of the total sand transport. Missing values for flooding 5 were replaced by results from flooding 1, assuming them to be the lower limit for flooding 5 transport. The density of dry sand was taken to be 1600 kg/m^3 with a porosity of 0.4. Adding the sand transport for all events results in a volume transport of $\sim 32 \text{ m}^3/\text{m}$, which is roughly half of the observed change. Part of the underestimation is surely due to the conservative estimate of sand concentrations with the linear fit, which ignores substantially higher concentrations close to the bed. As a comparison, when Q_c , the mean flow transport, was estimated with a linear fit it resulted in roughly 25 m^3 , while the exponential fit, which we view as an upper bound (Section 3.3.1), yielded $\sim 39 \text{ m}^3$. Since about 80% of the volume is transported by the mean flow, waves would add $\sim 10 \text{ m}^3$ so that the total volume transport for an exponential fit would be around 48 m^3 . This shows that there is a relatively high uncertainty for a long record of sand concentrations measured in the field.

In addition, bedload transport and sheet flow could not be measured, but might have contributed to the transport (Harter and Figlus, 2017). Further underestimations of the cross-shore transport could stem from the fact that 9 short inundation events are not included in the calculation, since these were too short or shallow ($\leq 0.4 \text{ m}$) to get reliable estimates for the sand transport. These small inundation events will probably not have added much to the overall change. Further, sand transport during the overwash phase, which precedes and follows inundations, is assumed small and in all likelihood less than 1% of the net transport during inundation (Wesselman et al., 2017). However, due to the elevation of the mounted ADVs, measurements only started when inundation depths exceeded $\sim 0.4 \text{ m}$, so that we might have missed some potentially high values, especially at the onset of inundations. Imprecision in the calculation of the volume change might have been caused by inaccuracies in the dGPS measurements. Another reason for the imbalance between volume change and sand transport could be that the alongshore transport did converge due to increased water levels in the channel located to the east of our field site and contributed to the changes in the area after all. In addition, eolian transport might have contributed to the volume change. Despite these various additional transport processes and the general difficulties of measuring suspended sand concentrations in a stormy environment, we were able to account for half of the observed volume change.

3.5.2 Comparison with other transport studies

Generally, the observed erosion and the landward transport of beach and beach crest during inundation agrees well with findings of dune erosion and transport to the back barrier part of the island during inundation by McCall et al. (2010) and Harter and Figlus (2017). While the seaward sand transport observed and modeled in previous studies (Goff et al., 2010; Sherwood et al., 2014; Harter and Figlus, 2017; Wesselman et al., 2017), caused by higher water levels in the back barrier basin than on the ocean side, was also observed in this study, the

total observed seaward sand transport is negligible since it adds up to $\sim 0.05 \text{ m}^3$ entirely. Research by Sherwood et al. (2014) and Harter and Figlus (2017) found erosion and scour channels, driven by the seaward flow in the ebbing storm surge, which were not observed at our field location. In addition, their model simulations suggested significant seaward sand transport and ocean side deposition. Seaward sand deposition was also observed by Goff et al. (2010). Most of the mentioned research was done in hurricane conditions on low-lying narrow barrier islands and spits, where the strong seaward flow caused by the storm surge ebb after the passing of hurricanes may explain some of the differences in seaward sand transport. Wesselman et al. (2017) modeled the cross-shore sand transport at our field location (also at the beach crest). For this, they created water levels and wave conditions (wave heights, periods) from historic data sets and separated them by classes. These were based on the peak water levels in the North Sea, with increasing water levels and wave heights per class. Flooding 5, which had the highest water level (Table 3.1), corresponds to their class 5 which is defined for North Sea water levels between 2.50-2.75 m. While the observed pattern of high landward sand transport at the start of inundations, low transport around high tide and seaward transport agree qualitatively, the modeled landward transport was $\sim 80\%$ lower than what we observed and the modeled seaward transport of $\sim -0.4 \text{ kg m}^{-1}\text{s}^{-1}$ for class 5 was not observed for flooding 5. This is a result of lower modeled ($\sim 0.7 \text{ m/s}$) onshore velocities and the modeled seaward velocities of $\sim 0.6 \text{ m/s}$, which not only forced the seaward sand transport but also increased sand suspension considerably after high tide. The likely cause for this discrepancy could be that for class 5 the model was forced with offshore significant wave heights of 5.38 m, while observed offshore significant wave heights for flooding 5 were significantly larger (7.43 m). Generally, in equal (shallow) water depths an increase in wave height forces an increase in water level set-up which for our field site is located at the crest. This, in turn, increases cross-shore velocities in the case that the large scale water-level gradient between North- and Wadden Sea is directed toward the Wadden Sea. In cases where the large scale gradient is directed seaward, set-up can counteract the seaward directed velocities or even overcome the large scale water-level gradient altogether so that the flow is still landward directed. This suggests that the sand transport at our field site is not only affected by the large-scale water levels, but also by the offshore wave heights.

3.6 Conclusions

To improve our understanding of suspended sand transport processes during inundation, observations of suspended sand concentrations, flow velocities, waves and water levels were collected during several inundation events on a barrier island in the North Sea during a 2-month campaign. Sand suspension and cross-shore transport showed high variabilities and were highest at the onset of inundations while they decreased considerably after high tide. About 80% of the combined transport from all floodings was done before high tide. This is mainly caused by the difference in mean flow velocities, which on a large scale were determined by water levels in the North and Wadden Sea and on a smaller scale by wave breaking. While suspended sand concentrations were primarily forced by the mean flow, time series of sand concentrations suggest that episodically high depth-integrated suspended sand concentrations (defined as $> 2 \text{ kg/m}^2$) were generated by the combined bed shear stresses of infragravity waves, short waves and currents. High suspension events on infragravity time scales were oftentimes supported by large short waves riding on the crest of infragravity waves, while smaller short waves rode in the troughs. The maximum relative contribution of the mean flow to the total transport, Q_c/Q_{all} , reached 0.98 before high tide, while the maximum

contribution of the infragravity waves, Q_{ig}/Q_{all} , reached 0.8 towards the end of inundation events. These observations suggest the existence of two sand transport regimes at our field site: flow-driven regimes which were characterized by high mean flows (> 0.5 m/s) and high current bed shear stresses ($\theta_c > 0.5$) while bed shear stresses generated by infragravity waves were small ($\theta_{ig} < 0.1$), and episodic regimes which can be observed when $\theta_c < 0.5$ and the ratio of infragravity wave and current related Shields numbers $\theta_{ig}/\theta_c > 0.11$. About half of all 15 minute time-steps were episodic events, highlighting the importance of infragravity waves.

Acknowledgement

We thank Marcel van Maarseveen, Henk Markies, and Arjan van Eijk for their excellent technical support without which this work could not have been done. Thanks also go to Daan Wesselman for his support during the field work and discussions afterwards. We are grateful for the constructive comments made by two anonymous reviewers and Associate Editor Curt Storlazzi. Natuurmonumenten assisted us during the field work. This work is supported by the Netherlands Organisation for Scientific Research (NWO) under contract 850.13.051, as well as by Natuurmonumenten, the National Forest Service (Staatsbosbeheer, SBB), and the Wadden Academy. The observational data are available from Engelstad et al. (2018a).

Chapter 4

Sand transport processes during barrier island inundation under variations in cross-shore geometry and hydrodynamic forcing

*A revised version of this chapter has been published: Engelstad, A., Ruessink, B. G., Hoekstra, P., van der Vegt, M. (2019), Sediment transport processes during barrier island inundation under variations in cross-shore geometry and hydrodynamic forcing. *Journal of Marine Science and Engineering*, 7, 210.*

Abstract

Inundation of barrier islands can cause severe morphological changes, from the break-up of islands to sand accretion. The response will depend on island geometry and hydrodynamic forcing. To explore this dependence, the non-hydrostatic wave model SWASH was used to investigate the relative importance of bedload transport processes, such as transport by mean flow, short- (0.05-1 Hz) and infragravity (0.005-0.05 Hz) waves during barrier island inundation for different island configurations and hydrodynamic conditions. The boundary conditions for the model are based on field observations on a Dutch barrier island. Model results indicate that waves dominate the sand transport processes from outer surfzone until landwards of the island crest, either by transporting sand directly or by providing sand stirring for the mean flow transport. Transport by short waves was continuously landwards directed, while infragravity wave and mean flow transport was seaward or landward directed. Landward of the crest, sand transport was mostly dominated by the mean flow. It was forced by the water-level gradient, which determined the mean-flow transport direction and magnitude in the inner surfzone and on the island top. Simulations suggest that short wave and mean flow transport is generally larger on steeper slopes, since wave energy dissipation is less and mean flow velocities are higher. The slope of the island top and the width of the island foremost affect the mean flow transport, while variations in inundation depth will additionally affect transport by short-wave acceleration skewness.

4.1 Introduction

The response of barrier islands to overwash (water overtops the beach- or dune crest without directly returning to the sea (Donnelly et al., 2006)) and inundation (the area is continuously submerged (Sallenger, A. H., Jr., 2000)) differs strongly between islands. It can include erosion such as shoreline retreat and breaching (Donnelly et al., 2006; Safak et al., 2016), the landward migration of islands, also termed "roll-over" (Donnelly et al., 2006), and sand accretion such as gains in subaerial areas (Durán et al., 2016). A crucial component that determines the morphological change of barrier islands is the island geometry. Low profile, narrow islands can be found primarily in wave-dominated, microtidal systems (tidal range

$< 2\text{ m}$) such as in the Gulf of Mexico (USA). These barriers have a high risk of erosion, roll-over and break-up, since the barrier response to overwash and inundation depends at least partly on dune-elevation and barrier width in addition to hydrodynamic forcing (e.g. Salenger, A. H., Jr., 2000; Donnelly, 2007; Rosati and Stone, 2007). Generally, barrier island width appears to be a factor that determines subaerial deposition or the landward migration of barrier islands (Rosati and Stone, 2007). The wide and high barrier islands in mixed energy systems (tidal range 2–4 m), such as in the Wadden Sea, which is fronting Denmark, Germany, and the Netherlands, have a potential to accrete sand (Engelstad et al., 2018b, Chapter 3). Observations in the Netherlands on part of a barrier island with a width of $\sim 1.3\text{ km}$, which is subjected to winter cold fronts and regular inundation, suggested that the subaerial part of the study area accreted sand (Engelstad et al., 2017; Engelstad et al., 2018b, Chapters 2 and 3). Additional observations of hydrodynamics and suspended sand concentrations at the beach crest related this to landward transport. From these observations, (Engelstad et al., 2018b, Chapter 3) defined two transport regimes for the Dutch barrier island. If flow velocities were high ($> 0.5\text{ m/s}$), which was frequently the case before high tide when water levels at the island crest exceeded the water levels in the basin, the transport was dominated by the flow. When flow velocities were low, the sand suspension and transport was episodic on an infragravity time-scale. It is, however, unknown what the sand transport processes were seaward of the crest or how stirring and transport by waves and currents would differ on a steeper bed slope. Additionally, the question remained if the observed suspension on infragravity (IG) time scales was primarily caused by the IG waves themselves, or by larger short waves riding the crests of IG waves. Sand transport can also be influenced by the gradient in water levels between ocean and back barrier basin (lagoon). It has been shown to greatly affect magnitude and direction of sand transport on barrier islands in the Gulf of Mexico and in the Wadden Sea (Sherwood et al., 2014; Harter and Figlus, 2017; Hoekstra et al., 2009; Wesselman et al., 2017; Engelstad et al., 2018b, Chapter 3).

The relative contribution of IG waves, short waves and mean flow to the net sand transport will at least partly depend on the bed slope steepness, since it affects the wave shape and energy dissipation (Van Dongeren et al., 2007; De Bakker et al., 2014). For a closed beach system, De Bakker et al. (2016) showed that IG sand transport and direction is dependent on the beach slope steepness. In the inner surf zone, IG transport was onshore directed for a steeper slope (1:35) where it contributed less than 20% to the total cross-shore sand flux, and seaward directed for a gentle slope (1:80) with a contribution of up to 60%. Further, studies suggest that the wave field on steep slopes close to shore is dominated by short wave (0.05–1 Hz) motion, while on gentle slopes IG waves are dominant (e.g. Ruessink et al., 1998a; Stockdon et al., 2006; de Bakker et al., 2015). However, these processes might differ in an open boundary system as during inundation.

In the last years, design criteria for barrier island restoration, have been developed. Considerations include the island width, height and the potential for the consolidation of sand, as well as the storm forcing (Rosati and Stone, 2007; Rosati and Stone, 2009; Schupp et al., 2013). For example on Assateague Island, Maryland, USA, island elevation and stability was increased by cutting notches through the foredunes (Schupp et al., 2013), which allowed overwash to deposit sand in the interior of the island. In the Netherlands, efforts to mitigate the effects of the expected sea level rise are on the way. Large parts of the barrier coastline are now protected by artificial sand drift dikes, which prevent landward migration and the accumulation of sand landwards of the dikes. Hence, the partial reopening of dunes and dikes is considered, to allow natural dynamics such as overwash and inundation. A better

understanding of the effect that island geometries and hydrodynamic forcing have on sand transport, will optimize design criteria for restoration efforts.

The goal of this study is to improve our knowledge of sand stirring and transport processes from the outer surfzone to the back barrier basin during barrier island inundation and the effect that island slopes and hydrodynamic forcing have on these processes. For this, a numerical model (SWASH) was used under variations in island geometries and hydrodynamic forcing conditions. The boundary conditions, such as wave heights and water levels, were based on observations (Engelstad et al., 2018b, Chapter 3) to allow insight into Wadden Sea processes, while modifications represent extremes and can be also applied to other systems. SWASH is described in Section 4.2, and a validation of the model with observations (Engelstad et al., 2018b, Chapter 3) can be found in Appendix A. The sand transport model, data analysis and experiments will also be introduced in Section 4.2. Results for a comparison of sand transport mechanism between a 1:30 and a 1:120 slope will be shown in Section 4.3, in addition to results for changes in the hydrodynamic forcing. The implications of our results will be discussed in Section 4.4, and we will summarize the findings in Section 4.5.

4.2 Methods

4.2.1 Model description

In order to accurately model the hydrodynamics during inundation and to include wave-shape effects in the investigation of sand transport processes, the model approach was two-fold. The phase resolving, nonhydrostatic wave-model SWASH (Simulating WAVes till SHore) (Zijlema et al., 2011) was used to simulate the hydrodynamics (see below), since field observations showed that IG and short waves were highly nonlinear and broke on the submerged island during inundation (Engelstad et al., 2017, Chapter 2). Additionally, IG bores propagated onshore and high sand suspension was observed on IG time-scales, highlighting the possible importance of IG waves in sand suspension and transport (Engelstad et al., 2018b, Chapter 3). SWASH has been shown to accurately hindcast hydrodynamic bulk properties, such as wave heights and periods, and detailed nonlinear interactions in the laboratory (Rijnsdorp et al., 2014; Smit et al., 2014; de Bakker et al., 2015) and, as well as being able to represent conditions found in the field (Rijnsdorp et al., 2015; Fiedler et al., 2018). For this study, the boundary conditions are primarily based on field observations collected in 2017 (Engelstad et al., 2018b, Chapter 3) to give insight into sand transport processes during the inundation of barrier islands in the Wadden Sea region, and how these processes change with a change in forcing and island geometry. This in turn reflects also on conditions in other systems.

2-D simulations in SWASH are very time-consuming, and since we want to use the model in an exploratory way (by exploring the differences in island geometry and hydrodynamic forcing on wave and current stirring and transport), we used SWASH in 1-D mode. While this allowed us to run comparisons in a timely manner, it had the drawback of leading to an overestimation in IG wave heights of roughly 100 % when compared to observations (see Appendix A). This overestimation of IG wave energy by SWASH, also observed by e.g. De Bakker et al. (2014), Fiedler et al. (2018), and Rijnsdorp et al. (2012), is caused by the fact that directional spreading cannot be included in 1-D mode, leading to an overestimation for waves in the low-frequency range (Guza and Feddersen, 2012). While IG energy will be overestimated for all experiments, the effect of island geometry and hydrodynamic forcing on IG wave stirring and transport can still be estimated. We will, however, avoid comparing

transport processes, such as IG and short wave transport, with each other in an absolute sense.

Next in the model approach, an energetics based bedload sand transport model (Bagnold, 1966; Bailard, 1981) was used (described below) to estimate stirring and transport by mean flow and waves. To simplify the analysis, we assume that wave and current processes have the same (relative) importance for suspended load as for bedload processes, since both are a function of flow velocity (to the power of 3 for bedload and to the power of 4 for suspended load, Bailard (1981)), and so here we only consider the time-averaged cross-shore bedload transport and ignore suspended-load and gravity-driven transport. This then also ignores any effects of phase lags between the suspended sand concentrations and the velocity field. The effect of wave asymmetry was added by using the formulation of Drake and Calantoni (2001) and Hoefel and Elgar (2003) which estimates the effect of acceleration skewness through the bedload.

Hydrodynamic model - SWASH

SWASH is based on the nonlinear shallow water equations, which describe the conservation of mass and the momentum balance, and accounts for non-hydrostatic pressure. For a full model description see Zijlema et al. (2011). Since in this study SWASH is used in the cross-shore (unidirectional) mode, the governing equations are

$$\frac{\partial u}{\partial t} + \frac{\partial u^2}{\partial x} + \frac{\partial wu}{\partial z} = -\frac{1}{\rho} \frac{\partial(p_h + p_{nh})}{\partial x} + \frac{\partial \tau_{xz}}{\partial z} + \frac{\partial \tau_{xx}}{\partial x} \quad (4.1)$$

$$\frac{\partial w}{\partial t} + \frac{\partial uw}{\partial x} + \frac{\partial w^2}{\partial z} = -\frac{1}{\rho} \frac{\partial(p_{nh})}{\partial z} + \frac{\partial \tau_{zz}}{\partial z} + \frac{\partial \tau_{zx}}{\partial x} \quad (4.2)$$

$$\frac{\partial u}{\partial x} + \frac{\partial w}{\partial z} = 0 \quad (4.3)$$

where $u(x, z, t)$ and $w(x, z, t)$ are the horizontal and vertical velocities, respectively. ρ is the fluid density, p_h and p_{nh} are the hydrostatic and non-hydrostatic pressure contributions and τ describes the turbulent stresses. The evolution of the free surface ζ is given by

$$\frac{\partial \zeta}{\partial t} + \frac{\partial}{\partial x} \int_{-d}^{\zeta} u dz = 0 \quad (4.4)$$

where $z = -d$ indicates the bottom. The bottom friction term τ_b , used at the bottom boundary, is based on the quadratic friction law

$$\tau_b = c_f \frac{U|U|}{h} \quad (4.5)$$

where U is the depth averaged velocity and h is the water depth. The bottom friction coefficient, c_f , is calculated as

$$c_f = \frac{n^2 g}{h^{\frac{1}{3}}} \quad (4.6)$$

where g is acceleration due to gravity. Here, the Manning's roughness coefficient, n , was set to its default of 0.019. The vertical resolution for the model runs was set to 2 vertical layers. Therefore, dissipation by wave breaking was captured with the hydrostatic front approximation, HFA, which imposes a hydrostatic pressure distribution at the wave front and initiates

wave breaking (Smit et al., 2013). The steepness criterion for the rate of surface rise to initiate wave breaking, α , was set to 0.6 and the criterion for the persistence of wave breaking, β , was set to 0.3 for the experiments (following the recommendations by Smit et al. (2013) for 2 layers) and varied in the model-data comparison (see Appendix A.1). The stability of the computations was assured by setting the time-step, based on the Courant number, to 0.0125 s for all runs. Simulations were run over 2 hours to allow for sufficient spin-up time over the large domain (described below), and bulk parameters were averaged over the last hour. At the ocean side, the boundary type was chosen to be weakly reflective, while at the basin side a 500 m sponge layer was used to avoid wave reflection. Further model implementations, the model domain, and the boundary conditions are described in detail below.

Sand transport model

We used the modification by Drake and Calantoni (2001) of Bailard's (1981) bedload sand transport equation for the sand transport model. The mass sand bedload transport per unit width and per unit time, q , is given as

$$q_b = K_b (< |u(t)|^2 u(t) >) \quad (4.7)$$

where the brackets denote time averages and

$$K_b = \frac{\rho_s}{g(\rho_s - \rho_w)} \rho_w c_f \frac{\varepsilon_b}{\tan(\varphi)}. \quad (4.8)$$

ρ_s and ρ_w are the densities of sand and water, respectively, and are here taken as 2650 kg/m³ and 1025 kg/m³. The efficiency factor ε_b is set to 1.03 following Drake and Calantoni (2001). This factor is larger than $\varepsilon_b = 0.135$, which was used by Thornton et al. (1996) and Gallagher et al. (1998), and the difference between these factors will be discussed in Section 4.4.3. The angle of internal friction for sand grains, $\tan(\varphi)$, is set to 0.63 (Thornton et al., 1996). While most studies set $c_f = 0.003$ (Thornton et al., 1996; Gallagher et al., 1998; Drake and Calantoni, 2001), we used equation (4.6) to account for the effect of varying depths in bathymetry.

The instantaneous cross-shore velocity $u(t)$ is the sum of mean flow \bar{u} and oscillating components

$$u(t) = \bar{u} + u_{ig}(t) + u_{short}(t) \quad (4.9)$$

where $u_{ig}(t)$ and $u_{short}(t)$ are the IG (0.005-0.05 Hz) and short wave (0.05-1 Hz) contributions, respectively. The velocity moments in equation (7) can be expressed as

$$< |u|^2 u > = < |(\bar{u} + u_{ig} + u_{short})|^2 (\bar{u} + u_{ig} + u_{short}) > \quad (4.10)$$

The expansion of equation (10) yields

$$\begin{aligned} < |u|^2 u > = \bar{u}^3 (1) + 3\bar{u} < u_{ig}^2 > (2) + < u_{ig} u_{ig}^2 > (3) \\ & + 3 < u_{short} u_{ig}^2 > (4) + 3\bar{u} < u_{short}^2 > (5) \\ & + 3 < u_{ig} u_{short}^2 > (6) + < u_{short} u_{short}^2 > (7) \end{aligned} \quad (4.11)$$

where we omitted terms that do not contribute to sand transport such as for example $3 < u_{short} \bar{u}^2 >$ (since the mean of the oscillatory motion u_{short} is zero). The numbers in round brackets given in equation (11) are given for the following reference. Term (1) on the right side of the equation describes transport and stirring by the mean flow. Terms (2)-(4) represent sand stirring by infragravity waves and transport by the mean flow (2), IG- (3), and

short waves (4). Further, terms (5)-(7) describe transport which is stirred by short waves and, again, transported by the mean flow (5), IG- (6) and short waves (7). In this way, cubed terms for the short and IG waves represent transport by wave skewness. Then

$$q_{mean} = K_b(\bar{u}^3 + 3\bar{u} \langle u_{ig}^2 \rangle + 3\bar{u} \langle u_{short}^2 \rangle) \quad (4.12)$$

$$q_{short} = K_b(3 \langle u_{short} u_{ig}^2 \rangle + \langle u_{short}^3 \rangle) \quad (4.13)$$

$$q_{ig} = K_b(\langle u_{ig}^3 \rangle + 3 \langle u_{ig} u_{short}^2 \rangle) \quad (4.14)$$

where q_{mean} is the total bedload transport by the mean flow, q_{short} is the total bedload transport due to short waves and q_{ig} is the total bedload transport by IG waves.

The change in wave shape, as described by wave skewness (long elongated troughs and narrow steep wave crests) and wave asymmetry (steep wave fronts) was quantified as

$$Sk = \frac{\langle \eta^3 \rangle}{\langle \eta^2 \rangle^{\frac{3}{2}}} \quad (4.15)$$

$$As = \frac{\langle (hil(\eta))^3 \rangle}{\langle \eta^2 \rangle^{\frac{3}{2}}} \quad (4.16)$$

where Sk describes wave skewness and As wave asymmetry, while hil is the Hilbert transform. Velocity skewness and asymmetry can be estimated in the same manner, by replacing η with u . To estimate the effect of short-wave acceleration skewness on sand transport (IG-wave acceleration skewness is small and therefore ignored here), we used the formulations of Drake and Calantoni (2001) and Hoefel and Elgar (2003):

$$q_{shortA} = K_a(a_{spike} - sgn(a_{spike}) a_{crit}) \text{ for } |a_{spike}| \geq a_{crit} \quad (4.17)$$

and

$$q_{shortA} = 0 \text{ for } |a_{spike}| < a_{crit} \quad (4.18)$$

where the fluid-motion descriptor a_{spike} (Drake and Calantoni, 2001) is calculated as

$$a_{spike} = \frac{\langle a(t)^3 \rangle}{\langle a(t)^2 \rangle}. \quad (4.19)$$

$a(t)$ is the magnitude of the instantaneous fluid acceleration, $sgn(a_{spike})$ is the sign of the acceleration skewness which can be positive or negative, and a_{crit} is the critical threshold for the transport initiation. Drake and Calantoni (2001) found best results for $K_a = 0.07 \text{ kg s m}^{-2}$ and $a_{crit} = 1 \text{ m s}^{-2}$ from highly idealized discrete-particle simulations, while for field data Hoefel and Elgar (2003) found $K_a = 0.37 \text{ kg s m}^{-2}$ and $a_{crit} = 0.2 \text{ m s}^{-2}$, which are used here. Hoefel and Elgar (2003) attributed the difference between their values and those found by Drake and Calantoni (2001) to random waves, breaking induced turbulence and variations in grain size shapes and sizes. We will discuss the variability in results caused by variations in K_a in Section 4.4.3.

4.2.2 Model implementations and experiment set-up

In the following, the implementations of the boundary conditions for the model runs and the experiment set-up are described. A model-data comparison was done and can be found in Appendix A. The model-data comparison was made more difficult by our choice of using the 1-D version of the model, by local wave generation (which is not included in the model), and by strong alongshore components of the flow. In addition, the offshore wave direction was obliquely incident (θ was between 307 and 335 degree) at the field site which was oriented -10 degrees from true East. However, results showed high model skill and r^2 values for short wave heights, water levels, and flow velocities. In addition, the model was able to hindcast the water levels variations caused by the tidal cycle and elevated water levels in the Wadden Sea.

Field observations

Field observations were used to validate the SWASH model (see Appendix A for the model-data comparison) and as boundary conditions for the experiments. These observations were collected during several inundation events on the barrier island Schiermonnikoog (Figure 4.1), the Netherlands, during the winter of 2016/2017 (for details on data collection and analysis see Engelstad et al., 2018b, Chapter 3). The field area was located on the island



Figure 4.1: The barrier island of Schiermonnikoog is located in the North Sea and is separated from the Dutch coast by the Wadden Sea. The field site was located on the eastern tip of the island, indicated in red.

tail, which is approximately alongshore uniform and low-lying. The height of the island crest, which was the highest point in the profile (Figure 4.2a), increased from ~ 1.7 m to 1.8 m above mean sea level (MSL) during the observational period. The beach slope between 0 m MSL and the island crest changed from 1:80 (initial) to 1:160 (final) as the island crest transitioned landward during the field campaign. Data were collected by an instrument

transect that was positioned approximately cross-shore from the North Sea side to the backbarrier basin (Wadden Sea) (Figure 4.2a).

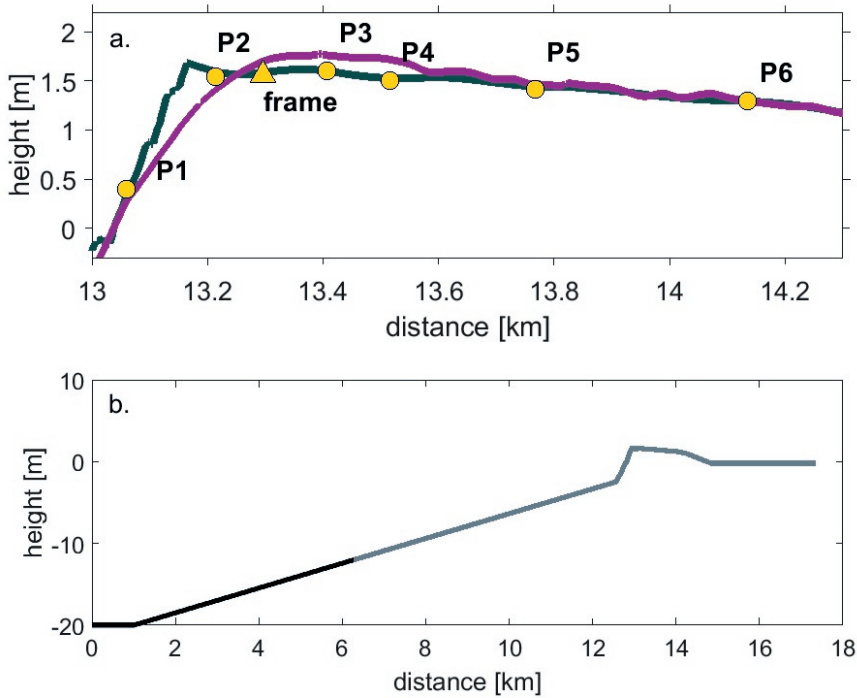


Figure 4.2: The initial (grey) and final (magenta) cross-shore profile for the observations (a.) The yellow dots show the location of the pressure sensors and the triangle indicates the instrument frame. The profile for the model-data comparison (b.) SWASH was first run to 12m water depth (dark grey profile) and in a second run from 12 m depth to the back barrier basin (see text for more explanation). The red line indicates the sponge layer.

The instruments consisted of six standalone pressure sensors and an instrument frame, which was equipped with a sideways oriented Sontek Acoustic Doppler Velocimeter Ocean (ADVO) probe to measure flow velocities and a Pressure Transducer (PT). Offshore wave heights and periods were measured hourly by a wave buoy (Schiermonnikoog Noord) located at a water depth of ~ 20 m approximately 15 km North-West of our field area. Water levels offshore were recorded every 10 minutes at a tidal station (Huibertgat) in ~ 5 m depth, approximately 6 km to the North-East, while water levels in the Wadden Sea were collected by the tidal station Schiermonnikoog located ~ 10 km to the West.

Boundary conditions

Wave and water level boundary conditions on the ocean side were implemented with observations from the offshore stations (Figure 4.1) as follows. First, wave heights and periods (Table A.1) were used to run the model from 20 m to 12 m water depth on a 2 m horizon-

tal grid (Figure 4.2b) with a JONSWAP spectrum to allow for the proper development of IG waves. This effectively shortened the modeling time for subsequent runs. Second, the simulated water-level time series in 12 m water depth were used as ocean side boundary conditions for consecutive model runs on a 0.5 m horizontal grid.

Observations showed that mean water levels in the Wadden Sea were oftentimes higher than in the North Sea during inundation events (Engelstad et al., 2017; Engelstad et al., 2018b, Chapters 2 and 3) even before high tide. This means that in order to adequately model the inundation of barrier islands in the Wadden Sea, water-level gradients need to be included in model runs. To be able to do this in SWASH, the water level in the basin was prescribed as a time series at the basin boundary. Since we only simulated snapshots in time, this "time series" was in reality only a repeated value, which was the difference in mean water levels between North and Wadden Sea (as an addition to the implemented still water level). The input file for the basin boundary was created so that it matched the input (water-level time series) file at the ocean side for which the frequency was 0.1 s over a period of 2 hours (to allow for enough spin-up time and propagation through the domain). For example, if the mean water level in the Wadden Sea was 0.15 m higher than in the North Sea, the input file at the basin boundary consisted of 72,000 values containing the number 0.15, which the model then added to the still water level at the basin boundary.

Introduction of scenarios for SWASH computations

For the experiments, first a reference case was chosen which was run on a variation of bed slopes to investigate the effect of island geometry on sand suspension and transport. Then the influence of hydrodynamic forcing and inundation depths on the transport processes were explored. The details are outlined below.

As the reference case for the simulations, we chose the most energetic inundation event observed with significant wave height $H_s = 7.45$ m and peak period $T_p = 10.1$ s (case *R*, Table 4.1), since it was identified as a flow driven event before high tide (Engelstad et al., 2018b, Chapter 3). The water level at the ocean side was chosen as 2.5 m, which was the water level at high tide and is an upper bound. The water in the basin was chosen to be 0.15 m higher than on the ocean side (2.65 m). This represents a somewhat conservative value for the basin, since water levels were observed to be on average 0.19 m higher in the Wadden Sea than in the North Sea during the two hours before high tide. The model was run on a simplified bottom profile (Figure 4.3) with a 1:120 slope seaward of the island crest, defined as gentle slope, and a very lightly ($\sim 1:2000$) down-sloping island top landward of the island

Table 4.1: Experiments ^a

	<i>R</i>	<i>S</i> ₁	<i>S</i> ₂	<i>H</i>	<i>R</i> ₅₅	<i>H</i> ₅₅	<i>L</i>
H_s (m)	7.45	7.45	7.45	4.55	7.45	4.55	7.45
T_p (s)	10.0	10.0	10.0	7.2	10.0	7.2	10.0
wl N-Sea (m)	2.5	2.5	2.5	2.5	2.5	2.5	2.0
wl W-Sea (m)	2.65	2.65	2.65	2.65	3.05	3.05	2.15
seaward slope	1:120	1:30	1:120	1:120	1:120	1:120	1:120
landward slope	1:2000	1:2000	0	1:2000	1:2000	1:2000	1:2000

^a Boundary conditions for the reference case *R*, slope variations *S*₁ and *S*₂, moderate wave height *H*, higher basin water levels *R*₅₅ and *H*₅₅, and lower inundation depth *L*. These were defined by significant wave heights (H_s), periods (T), water levels in the North Sea (wl N-Sea) and Wadden Sea (wl W-Sea), and slope configurations (see Figure 4.3).

crest. The choice of a 1:120 seaward slope was made as an average lower bound for slope steepness on barrier islands in the Netherlands, while the landward sloping island top was typical at the field location (Figure 4.3).

In order to evaluate the effects of slope steepness on sand stirring and transport, the seaward slope was first changed to 1:30 as an upper bound for beach steepness in the Netherlands, while all other parameters were kept the same (case S_1 , Table 4.1). Second, the slope steepness was again set to 1:120 while the island was changed from a down-sloping island top to a straight top (no tilt), to estimate the effect of island geometry (case S_2 , Table 4.1).

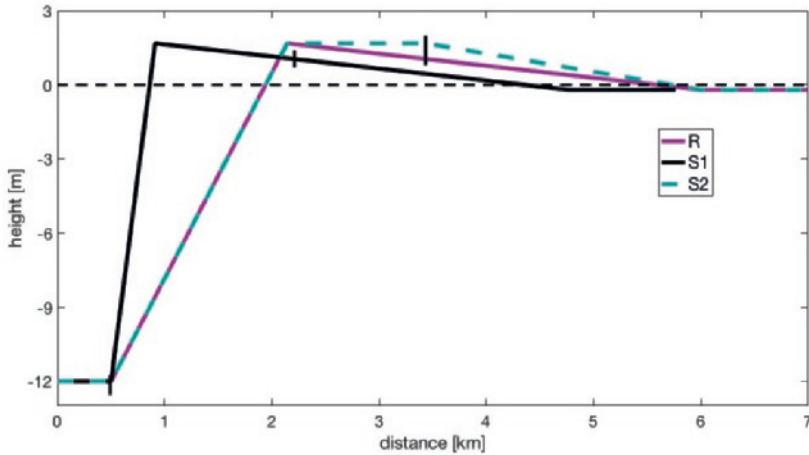


Figure 4.3: The seaward and landward slope configurations for R , S_1 , and S_2 used for the simulations. The vertical black bars indicate the extend of the normalized grid, used in the ensuing figures in Section 4.3, from the start of the slope until 1.3 km after the crest.

Observations showed that the sand transport after high tide oftentimes developed into an episodic regime during which sand suspension and transport was observed on infragravity wave time scales, due to a further increase in water levels in the Wadden Sea which decreased flow velocities. To investigate this, the reference case R was compared to conditions with a basin water level which is 0.55 m higher than the water level on the ocean side (case R_{55} , all other parameters being the same as R). This value was the maximum observed difference between North and Wadden Sea and is here used as an upper bound.

The significance of the wave forcing was evaluated by comparing R to wave conditions observed during the inundation with the lowest measured wave heights ($H_s = 4.55$, $T_p = 7.2$ s, case H , Table 4.1 and A.1). All other parameters were kept the same as those for R so that sand transport under variations in wave forcing could be evaluated independent of water levels or gradients therein. Also note that while on average offshore wave heights and water levels in the basin increase with storm size in the North Sea (Wesselman et al., 2017), larger waves do not necessarily coincide with stronger gradients (compare flooding 1 and flooding 2 in Table A.1). H was, like R , compared to the maximum water level in the basin (case H_{55}) to investigate the difference in moderate and strong wave forcing on the local water-level gradient. Finally, the water level on the ocean side was lowered by 0.5 m in case L , but otherwise parameters were kept the same as those for R , to explore the influence of

inundation depth on sand suspension and transport. Shallow inundation depths occur either during the tidal cycle or if the storm surge level is lower.

4.3 Results

4.3.1 Reference case

For an easier comparison of variations in slope steepness, all experiments will be presented on a "normalized" grid, xx , for which output locations are chosen to be at the same depth with respect to mean sea level (MSL). The exception is S2 for which the water depth stays the same after the crest. For example, $xx = 0$ corresponds to $z = -12$ m (MSL) and $xx = 1$, the location of the crest, is at 1.8 m. For S2 this height will stay constant, while for all other slopes the island height drops to 1 m ($xx = 3.7$). After the crest xx has the same distance from the crest for all cases (see also Figure 4.3).

The transport processes differed considerably from the outer surf zone (starting at $xx = 0$ in a water depth of ~ 14 m) to the back barrier basin ($xx = 3.7$, water depth = 1.7 m) for reference case R (Figure 4.4a). On the outer slope, the consistently landward directed transport by short wave skewness q_{short} and asymmetry q_{shortA} was opposed by the seaward directed mean flow q_{mean} and infragravity wave transport q_{ig} . However, landwards of $xx = 0.75$ in a water depth of ~ 3.5 m all transport was onshore directed. The transport terms will be discussed in detail below. Due to the uncertainty in coefficients and the overestimation of IG waves, we will not discuss absolute values and focus in the remainder of this chapter on changes and comparisons in a relative sense.

The term q_{short} increased from the start of the slope ($xx = 0$) to a maximum on the outer slope (Figure 4.4a) at the onset of wave breaking in a water depth of 9.8 m, corresponding to the shoaling of short waves (Figure 4.5d) which caused an increase in wave skewness (Figure 4.6a). Due to wave breaking, q_{short} was significantly smaller at the crest and close to zero after it ($xx = 1.5$). q_{short} was mostly stirred by the short waves themselves (Figure 4.7b), with the exception of a small contribution to the stirring by IG waves (max $\sim 30\%$ of total short wave transport after the crest when short wave stirring is small, not shown).

Transport due to short-wave acceleration skewness q_{shortA} developed on the outer slope ($\sim xx = 0.5$), caused by an increase in velocity asymmetry (Figure 4.6b). While short-wave height at the crest is only about 1/10 of the outer surfzone values, short-wave asymmetry is at a maximum (Figure 4.6b) due to the limited water depths over the crest. Since accelerations are largest under the steep wave crest where orbital velocities are onshore directed, the net transport by acceleration skewness will be onshore directed (Hoefel and Elgar, 2003). q_{shortA} exceeded q_{short} at the crest by far, which could at least partly depend on our choice of parameters. However, the trend is consistent with the change in wave shape, which showed a decline in short wave skewness and the before mentioned maximum in asymmetry at the crest (Figure 4.6a and b). The term q_{ig} was offshore directed on the outer slope (Figure 4.4), and onshore thereafter ($\sim xx = 0.5$). The maximum of the seaward directed q_{ig} was located almost at the same location as the maximum for q_{short} ($xx \sim 0.3$) and was caused by the more intense short-wave stirring at this location (Figure 4.7b). q_{ig} decreased around the crest, probably because of a decrease in short wave stirring. The change in transport direction for q_{ig} suggests that in the shoaling zone, where IG waves are bound to the wave group, the larger short waves coincide with the seaward stroke of the IG waves (e.g. Ruessink et al., 1998b; De Bakker et al., 2016). After the bound IG wave is released during short wave breaking, the larger short waves coincide with the positive stroke of the IG waves, which is

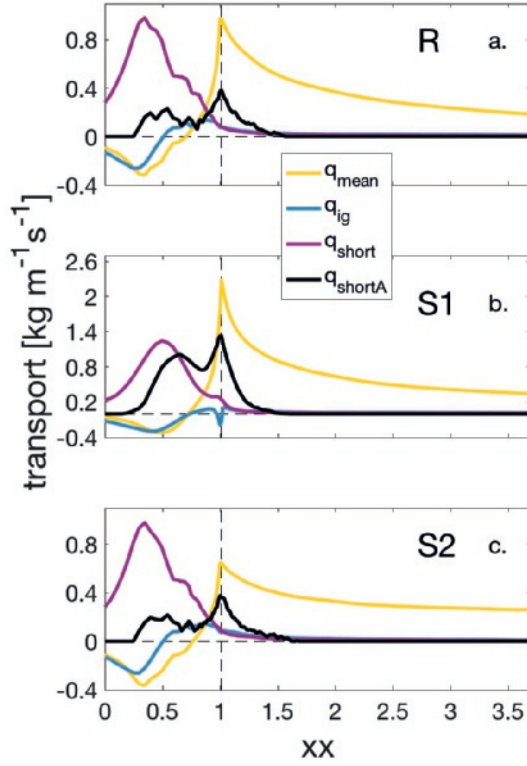


Figure 4.4: Transport processes q_{mean} , q_{short} , q_{ig} , and q_{shortA} are shown for slopes R (a.), S1 (b.) and S2 (c.) on a normalized grid (xx) from the beginning of the seaward slopes ($xx = 0$) to the back barrier basin ($xx = 3.7$). Grid locations before the crest (indicated by the vertical dashed line) indicate output in the same water depth (but not the same distance in reference to the crest, while they are equidistant after the crest (and at the same depth for R and S1, but not for S2, see Figure 4.3). Note that vertical scales are different.

probably caused by depth modulation of the infragravity waves (Janssen et al., 2003; Tissier et al., 2015; De Bakker et al., 2016). The large reduction in IG wave heights of $\sim 60\%$ between the maximum q_{ig} on the seaward slope and values at the crest suggests IG wave breaking (De Bakker et al., 2014), but could also have been at least partly caused by bed friction. Estimates of IG wave dissipation during inundation – based on our field experiments (Engelstad et al., 2017, Chapter 2) – suggested that IG wave breaking before the crest was roughly 2-9 times higher than IG wave dissipation by bed friction, depending on the water depth. The contribution of IG wave stirring to q_{ig} is close to zero (Figure 4.7b), since IG waves skewness is small (Figure 4.6c), even though asymmetry is high (Figure 4.6d).

The term q_{mean} was largest around the crest and was reduced to $\sim 25\%$ of the crest value at the basin side. While flow velocities were highest after the crest ($xx \sim 1.5$), the maximum in q_{mean} at the crest was caused by short and IG wave stirring (Figure 4.7a) which continued to be

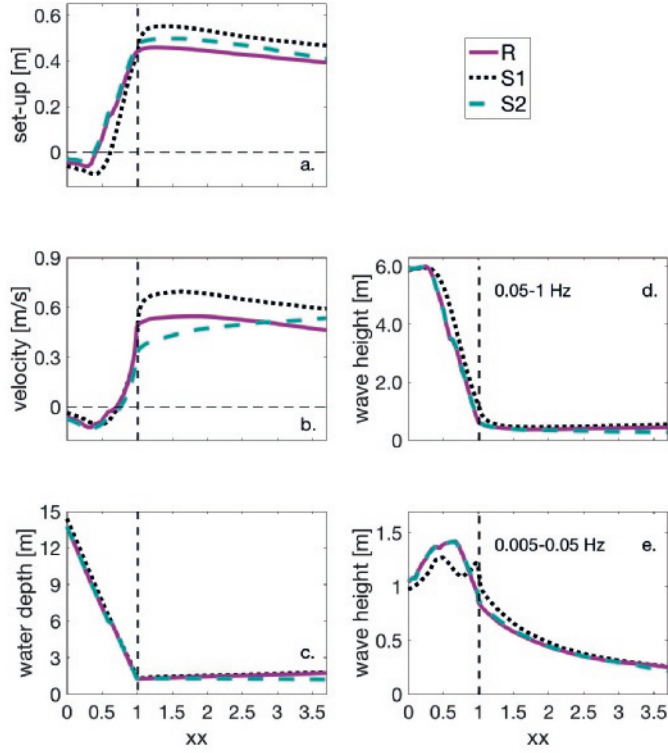


Figure 4.5: Modeled water level set-up (a.) which includes elevated water levels in the basin, mean flow velocity (b.), water depth (c., including storm surge and wave set-up), short (d.) and IG (e.) wave heights and water depth for slopes R, S1 and S2 on a normalized grid (xx) from the beginning of the seaward slopes ($xx = 0$) to the back barrier basin ($xx = 3.7$). Grid locations before the crest (indicated by the vertical dashed line) indicate output in the same water depth (but not the same distance in reference to the crest), while they are equidistant and at the same depth after the crest for R and S1 (but not for S2 for which the island top has the same height as the crest).

an important contributor even after the crest. As mentioned before, q_{mean} changed direction from seaward (where it was solely stirred by short waves) to landward directed about mid-surfzone at $xx = 0.75$. On a closed beach, the mean seaward directed flow (undertow) is generated to balance the landwards directed mass flux under the breaking wave crests. Symonds et al. (1995) found for a reef situation (which is similar to inundation on a barrier island in that the landward boundary is open) that the radiation stress gradient, caused by the breaking waves, is partitioned between setting up the water level and driving a cross-shore flow. Here, it appears that the (small) offshore directed flow is a result of the strongest short wave breaking in the outer surfzone which created a steep seaward directed pressure gradient and forced the seaward flow. After the crest, wave breaking ceased and the flow was forced by the landward directed pressure gradient (Figure 4.5b).

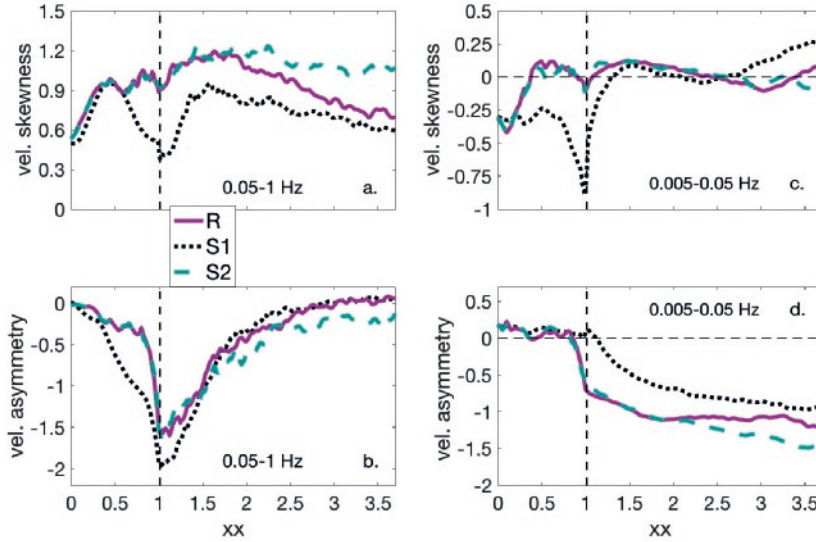


Figure 4.6: Modeled short wave velocity skewness (a.) and asymmetry (b.), and IG wave velocity skewness (c.) and asymmetry (d.) for slopes R , $S1$ and $S2$ on a normalized grid (xx) from the beginning of the seaward slopes ($xx = 0$) to the back barrier basin ($xx = 3.7$). Grid locations before the crest (indicated by the vertical dashed line) indicate output in the same water depth (but not the same distance in reference to the crest), while they are equidistant and at the same depth after the crest for R and $S1$ (but not for $S2$ for which the island top has the same height as the crest).

Stirring for q_{mean} before the crest was exclusively provided by short and IG waves and continued to be relevant even after the crest (Figure 4.7a), since wave energy was not completely dissipated (Figure 4.5c, d and e). Even though IG wave stirring is surely overestimated, these results agree with observations for which increases in sand suspension on IG time scales was observed (Engelstad et al., 2018b, Chapter 3).

4.3.2 Slope comparisons

The comparison of reference case R with $S1$ (slope of 1:30, everything else being the same as R), suggests that transport was generally higher for the steeper slope. The maximum for q_{short} on $S1$ was located more shorewards in a water depth that was approximately 3 m lower than for R . q_{short} was about 30 % higher for the steeper slope compared to the gentle slope due to higher short waves (Figure 4.5d). On the crest, however, where short waves on the steep slope were almost twice as high as on the gentle slope (1 m compared to 0.6 m), q_{short} was about 3 times as high for $S1$ as it was for R . This was reflected in the higher stirring for the short wave transport (Figure 4.7b and d) which was again almost entirely forced by the short waves (the very small contribution of IG wave stirring is not shown). The difference in transport and stirring for q_{short} can be explained by the effect of slope steepness on wave transformation, as was shown in previous studies (e.g. Aagaard et al., 2013). Since on a steeper slope less wave energy will be dissipated (Figure 4.5d), short-wave heights were much larger for $S1$. Lower skewness and higher asymmetry for $S1$ values suggest (Figure 4.6 a and b) that while short waves dissipated less energy, they were more pitched forward. This was reflected in

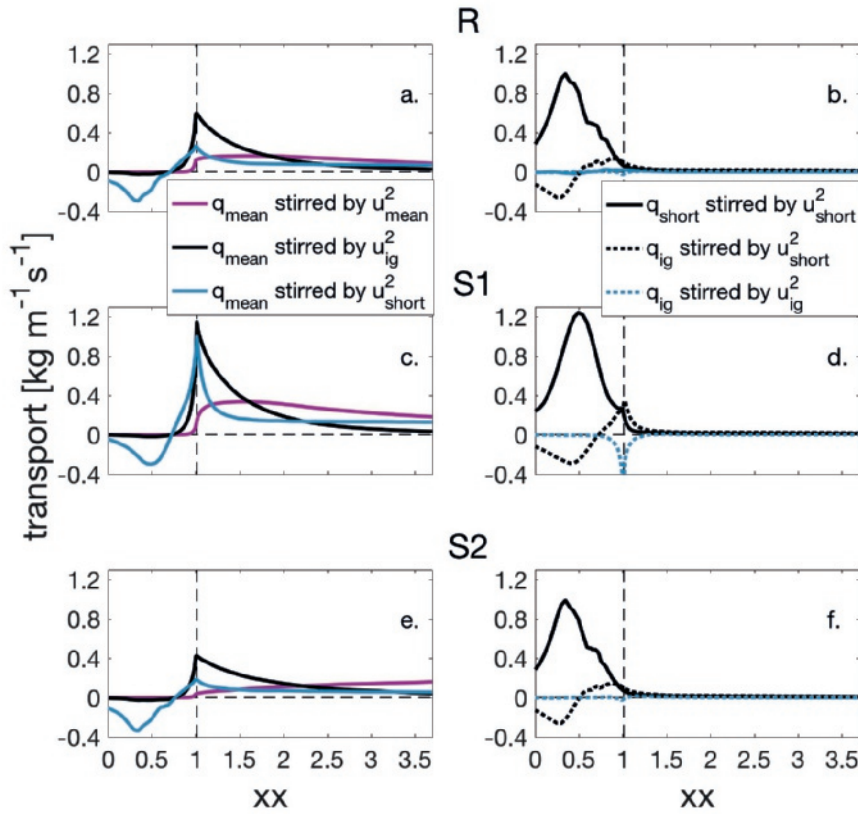


Figure 4.7: Stirring processes for q_{mean} (a., c. and e.), q_{short} (b., d. and f.) and q_{ig} (b., d. and f.) for R (a. and b.), S1 (c. and d.) and S2 (e. and f.) on a normalized grid (xx) from the beginning of the seaward slopes ($xx = 0$) to the back barrier basin ($xx = 3.7$). Grid locations before the crest (indicated by the vertical dashed line) indicate output in the same water depth (but not the same distance in reference to the crest), while they are equidistant and at the same depth after the crest for R and S1 (but not for S2 for which the island top has the same height as the crest).

q_{shortA} which was about 4-5 times higher on the steep slope compared to the gentle slope (Figure 4.4b). Generally, the results suggest that short waves transport more sand from the surfzone over the crest onto the island top for steeper slopes.

The evolution of q_{ig} was obviously different between the slopes. While on the gentle slope q_{ig} was landward directed from $\sim xx = 0.5$ (Figure 4.4), on the steeper slope most of the transport in the inner surfzone and at the crest was seaward directed. The seaward directed q_{ig} , stirred by IG waves, at the S1 crest contrasted with R (Figure 4.7d), which was close to zero. At the same location, landward directed q_{ig} stirred by short waves was about 3 times higher than for R. The difference in q_{ig} between R and S1, again, was caused by the difference in wave transformation on the gentle and the steep slope. IG waves grew more on the gentler outer seaward slope compared to the steeper slope, probably because energy transfers be-

tween IG waves lead to a steepening of these waves followed by wave breaking (de Bakker et al., 2015). Further, IG waves apparently broke only right before the crest on the steeper slope and were higher by roughly 10% at the crest than IG waves on R . For S_1 , strong (-0.8) negative IG wave skewness (Figure 4.6c) was predicted at the crest, which indicates that IG waves had broader, shallower crests and steeper narrower troughs. During negative IG wave skewness the seaward stroke velocity was faster than during the landward stroke, which might explain the seaward contribution of IG suspended q_{ig} transport. Butt and Russell (1999) found negative skewness in the swash during high energy conditions and related potentially offshore directed transport to it. Negative IG wave skewness was also predicted for R around the crest (albeit close to zero) and was observed for field measurements (Figure A.1). The landward directed component of short wave suspended q_{ig} can, again, be related to higher short waves suspending more sand during the landward stroke of IG waves.

Prediction for the seaward directed mean flow transport q_{mean} in the outer surfzone were similar for R and S_1 (compare Figure 4.4 a and b), but the landward q_{mean} increased at a higher rate for S_1 and was more than double at the crest and on the island top. Since flow velocities were the same on the slope, the higher values before and at the crest can be foremost attributed to increased IG and short wave stirring (Figure 4.7c) caused by the larger wave heights (especially for IG waves, Figure 4.5c and d). Higher q_{mean} for S_1 on the island top was forced by continuous wave breaking over the crest, which moved the location of maximum set-up for S_1 landwards to around $xx = 1.25$ and increased it roughly 25 % compared to R . Further, mean velocities were $\sim 30\%$ higher after the crest. In general, mean flow velocities at an open boundary were forced by breaking waves and pressure gradients. The similar flow velocities before and at the crest might have been a result of a balance between the seaward directed pressure gradient which was steeper for S_1 , inducing a stronger seaward flow component for S_1 , and higher onshore velocities induced by wave breaking.

In comparison, q_{mean} on S_2 (with a straight island top instead of a downward slope) was predicted as only $\sim 60\%$ of R at the crest, but $\sim 130\%$ of R at the basin side (Figure 4.4a and c). This coincided with smaller mean flow velocities at and after the crest as for R ; however, velocities increased from crest to back barrier basin for S_2 , while they decreased for R . These differences were likely caused by the relative higher decrease in water depth towards the basin (since the elevation of the top stayed the same) compared to R , which forced flow velocity to increase to conserve discharge. Since the mean flow was increasing toward the basin side, this suggest that more sand will be transported into the basin compared to a sloping top. In return, this would indicate that under the same wave forcing and beach slope steepness, more sand can be accreted on the island for steeper sloping island tops.

Results suggest that waves directly dominate the sand transport processes before and at the crest through transport and by providing the necessary stirring for q_{mean} . On the island top, the transport is dominated by the mean flow which is primarily forced by the pressure gradient. In addition, variations in transport can be introduced by island geometry, such as stronger dissipation on a gentler slope compared to a steeper slope and a decrease in the landward transport for down-sloping island tops through the increase in water depth which reduces flow velocities.

4.3.3 Variations in hydrodynamic forcing and inundation depths

Section 4.3.2 discussed the predicted differences in sand transport under different island geometries. In the following, the influence of hydrodynamic forcing will be explored. Not surprisingly, when offshore wave heights were reduced by 60% of R values (case H), it caused an overall decrease in transport compared to R (compare Figure 4.8a and b). While q_{ig} , q_{shortA} ,

and q_{short} for H were roughly $1/3$ to $1/2$ of R values, q_{mean} was severely reduced to about $1/6$ of its value in R . The smaller set-up for H (Figure 4.9a), due to the smaller wave forcing, balanced the water levels in the back barrier basin. Therefore, forcing by the pressure gradient on the landward side was missing and transport was small, since flow velocities were close to zero (0.05 m/s, Figure 4.9b). Further, the maximum seaward transport on the slope exceeded the maximum landward directed transport (Figure 4.8b), due to slightly higher flow velocities (-0.08 m/s) and more intense short wave stirring on the slope compared to the crest (not shown). Stirring for q_{mean} was only provided by IG and short waves since the flow velocity was close to zero (not shown). Generally, transport for H on the slope was initiated higher up on the slope than for R , due to the lower wave height over depth ratio which caused a later onset of wave non-linearities.

To explore the balance between wave-induced set-up and higher water levels in the back barrier basin further (and its impact on sand transport) water levels in the back barrier basin were increased for R and H so that they were 0.55 m higher than on the ocean side (cases R_{55} and H_{55}). The increase in water levels for case R_{55} affected mostly q_{mean} and caused it to be seaward directed between the outer surfzone and $\sim xx = 1.25$. Maximum seaward directed q_{mean} values were almost twice as high for R_{55} as for R (compare Figure 4.8a and c) in the outer surfzone. Wave set-up did not exceed the higher water levels in the basin and was a couple of centimeters smaller so that the water-level gradient was offshore directed

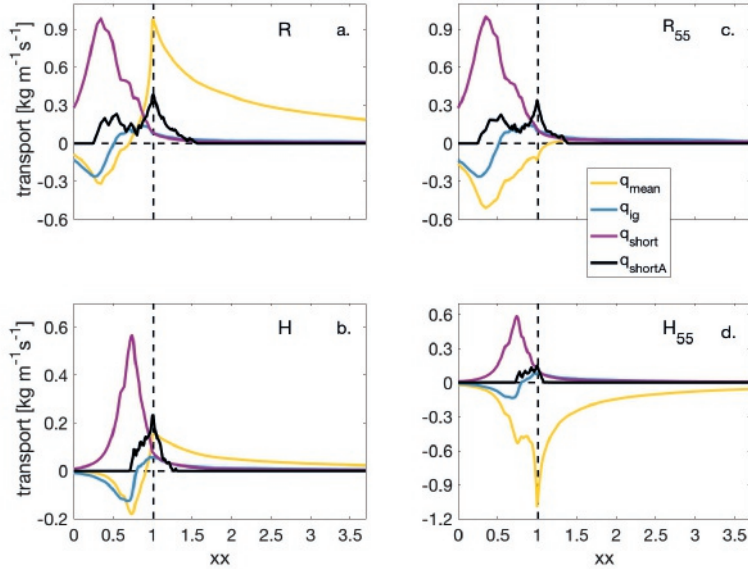


Figure 4.8: Transport processes q_{mean} , q_{short} , q_{ig} , and q_{shortA} are shown for reference case R ($H_s = 7.45\text{m}$) (a.) and H ($H_s = 4.55\text{m}$) (b.). For R and H the water level in the basin was 0.15 m higher than offshore while it was 0.55 m higher for R_{55} (c.) and H_{55} (d.). The x-axis is the normalized grid (xx) from the beginning of the seaward slopes ($xx = 0$) to the back barrier basin ($xx = 3.7$). Here, the slopes are the same (1:120) and output at all grid locations is in the same water depth. The vertical dashed line indicates the location of the crest.

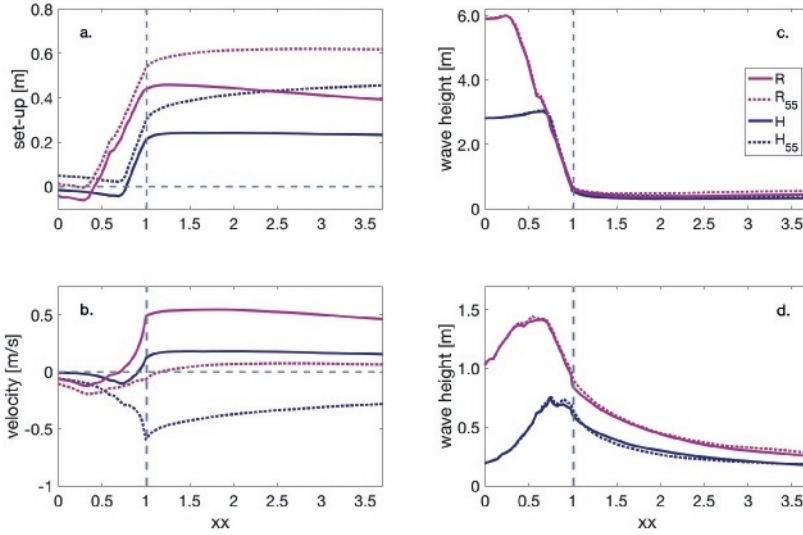


Figure 4.9: Simulated water level set-up (which includes higher water levels in the basin) (a.), mean flow velocities (b.), short- (c.) and IG wave heights (d.) for R , H , R_{55} , and H_{55} . The extension 55 refers to a water level that is 0.55m higher in the back barrier basin. The x-axis is the normalized grid (xx) from the beginning of the seaward slopes ($xx = 0$) to the back barrier basin ($xx = 3.7$). Here, the slopes are the same (1:120) and output at all grid locations is in the same water depth. The vertical dashed line indicates the location of the crest.

(Figure 4.9a). Even though, the flow did not reverse to a seaward direction landwards of the crest and was close to zero (Figure 4.9b). The small landward directed mean flow velocity was probably forced by the skewed orbital motions, while the IG radiation stress gradient might have contributed. q_{mean} completely reversed to a seaward direction for lower wave heights, as can be seen for H_{55} (Figure 4.8d). Here, the wave set-up was too small (Figure 4.9a) to oppose the higher water levels in the basin and a continuous seaward directed water-level gradient was created, driving strong seaward flow throughout the domain.

Model simulations suggest that a critical threshold exists between water level set-up and higher basin levels which determines the mean-flow transport direction, and this threshold depends on the offshore wave forcing. This is in agreement with observations and model results of cross-shore flow velocities during inundation (Engelstad et al., 2017; Wesselman et al., 2017). Clearly, in situations when the water level in the basin is lower than in the ocean, as can be observed at times during the rising tide in the Netherlands due to a phase lag between ocean and basin, q_{mean} will always be landwards directed (as was observed).

Striking is that q_{shortA} was reduced by approximately 35% for H_{55} on the crest in comparison to H (compare Figure 4.8b and d), while it is only reduced by $\sim 10\%$ for R_{55} . This is in line with a reduction in short wave asymmetry which was ~ -1.2 and -0.8 for H and H_{55} , while for R and R_{55} wave heights asymmetries were -1.5 and -1.3 , respectively. This difference in wave shape transformation might be explained by the water depth to wave height ratio, since set-up was greater for the higher wave case.

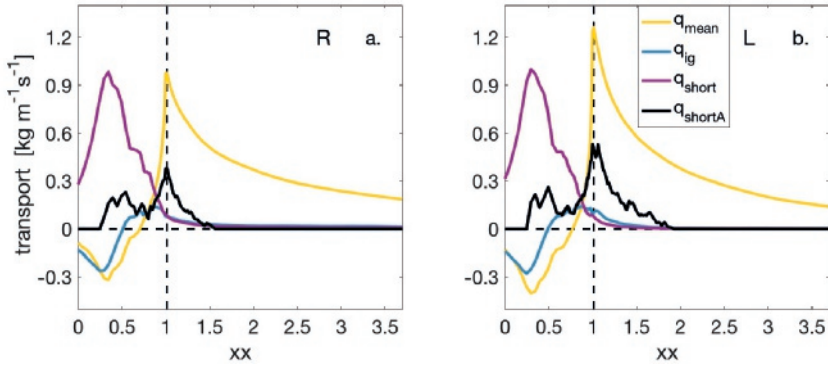


Figure 4.10: Transport processes q_{mean} , q_{short} , q_{ig} , and q_{shortA} are shown for reference case R (a.) and case L (b.) for which the water level at the ocean side was lowered by 0.5 m. The x-axis is the normalized grid (xx) from the beginning of the seaward slopes ($xx = 0$) to the back barrier basin ($xx = 3.7$). Here, the slopes are the same (1:120) and output at all grid locations is in the same water depth. The vertical dashed line indicates the location of the crest.

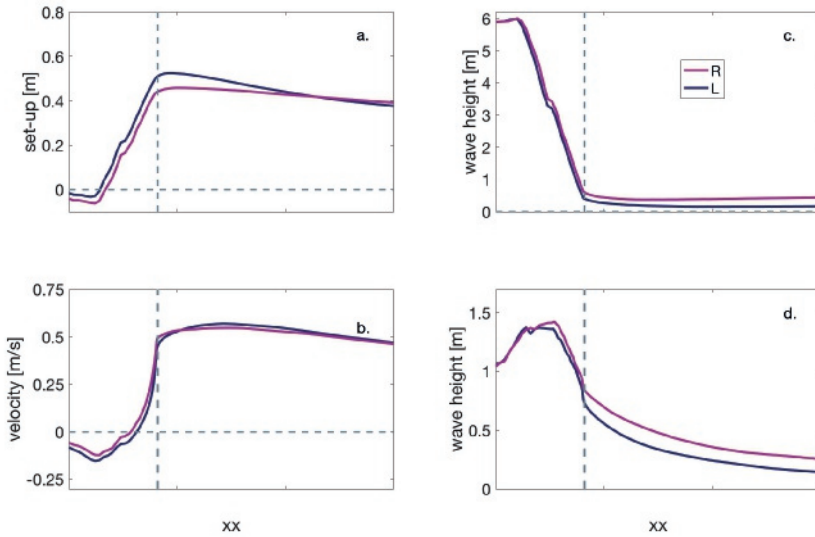


Figure 4.11: Predicted water level set-up (which includes higher water levels in the basin) (a.), mean flow velocities (b.), short- (c.) and IG wave heights (d.) for R and L. The x-axis is the normalized grid (xx) from the beginning of the seaward slopes ($xx = 0$) to the back barrier basin ($xx = 3.7$). Here, the slopes are the same (1:120) and output at all grid locations is in the same water depth. The vertical dashed line indicates the location of the crest.

Generally, lowering the ocean side water level (case L) while keeping the basin side level 0.15 m higher in the basin, also shows an overall increase in q_{shortA} (Figure 4.10) which was roughly 30% higher at the crest than R . Here, short wave height asymmetries were as high as 2.1 (not shown). In addition to q_{shortA} , q_{mean} also increased for lower inundation depths (25% higher at the crest). The increase in seaward directed q_{mean} before the crest was forced by slightly higher seaward directed velocities (Figure 4.11b). While the set-up for L was higher (Figure 4.11a) due to the lower water depth, velocities on the island top were only slightly larger than for R and smaller at the crest. The $\sim 20\%$ higher q_{mean} for L was caused by an increase in IG stirring (not shown), which could have been forced by slightly higher wave skewness at the crest (0.06 for R and 0.12 for L) or by a higher radiation stress gradient, since IG wave heights were slightly lower for L . q_{mean} stirred by short wave on the other hand was slightly lower after the crest, since wave heights for L were close to zero due to the low inundation depths (~ 0.8 m at the crest).

4.4 Discussion

4.4.1 Role of waves and mean flow throughout the domain

Model results suggest that stirring and transport by short waves is most important in the outer slope, after which q_{short} decreases significantly. On the other hand, q_{shortA} usually increases from the outer slope and is maximum at the crest. While most terms increase with an increase in slope steepness, q_{ig} varies most in magnitude and direction. The switch from a seaward to a landward transport direction between outer to inner surfzone had been noted before by De Bakker et al. (2016) for short-wave stirred IG transport on a closed beach. The seaward directed q_{ig} at the crest of the steep slope is likely an effect of the negative IG wave skewness, which is much higher on the steeper slope. While negative skewness was observed by others and appears to be related to potential offshore IG transport (Aagaard and Greenwood, 1994; Butt and Russell, 1999), the nonlinear processes which are causing it and their slope dependence need to be further investigated. While in most cases, these processes will generally be rather small compared to q_{mean} and q_{shortA} (especially in light of the IG wave overprediction), negative IG skewness might determine the net seaward or landward transport direction when mean flow velocities are small, such as for R_{55} .

(Engelstad et al., 2018b, Chapter 3) found two transport regimes at their field site, located at the island crest of a barrier island in the North Sea: a flow driven regime during high flow velocities (> 0.5 m/s), and an episodic regime for low flow velocities, where sand suspension and suspended transport was observed on an IG wave time scale. Results suggest that this finding might be generally applied, since the mean-flow rarely stirs sand if it is < 0.5 m/s (compare Figures 4.2 and 4.5), and most of the stirring is provided by IG and short waves. The difference in the velocity threshold for the slopes is caused by the fact that waves dissipate less energy on the steeper slope and continue to provide much of the stirring for q_{mean} after the crest. While it was unclear in that study if the observed high values of suspended sand under IG waves were caused by the IG waves themselves or forced by larger short waves riding the crest of IG waves, model results suggest that IG wave stirring is important, especially landwards of the crest when most of the short wave energy has dissipated.

4.4.2 Implications for barrier islands

The wave climate, tidal- and storm forcing, and island geometry vary for locations. In the North Sea region, winter storms regularly cause elevated water levels in the Wadden Sea. Observations, however, showed that seaward flow and sand transport on the island top was

small (Engelstad et al., 2017; Engelstad et al., 2018b, Chapters 2 and 3), since wave heights were large enough to create significant wave set-up opposing the seaward directed large scale water-level gradients. This was also reflected in model results where large wave heights were able to prevent the flow reversal on the island top, even though the magnitude of the seaward directed water-level gradient was the highest measured (0.55 m) during the observational period (see e.g. R and R_{55} in Figure 4.9). In a system with smaller wave heights, such as in the Gulf of Mexico during cold fronts, tropical storms or even weak hurricanes where offshore wave heights rarely exceed 4 m (Rosati and Stone, 2009), wave set-up will be rather small (Figure 4.9). This will generally decrease deposition on the island top, but also in the basin. However, if the water level in the basin is large enough, such as during the surge-ebb caused by passing hurricanes, erosion of the island top and seaward deposition will occur (see H and H_{55} in Figure 4.8), as predicted and observed by Goff et al. (2010), Sherwood et al. (2014), and Harter and Figlus (2017). This suggests that islands which are exposed to small wave forcing, and large seaward directed water-level gradients will be more vulnerable to erosion.

Generally, the results imply that while the cross-shore geometry is important for the island response to inundation, considerations for the restoration of barrier island and overwash processes need to consider the local wave climate and surge levels in the back barrier basin as well.

4.4.3 Model performance and sensitivity of results to model implementations

The model captured observed changes in water levels and short wave heights well (for a detailed model-data comparison see Appendix A), but flow velocities were underpredicted while infragravity wave heights were overpredicted. Further, asymmetry and skewness were not captured well, which can be foremost ascribed to the comparison of field data with the 1D mode of SWASH. Especially the transformation of IG skewness is unsatisfactory, likely since the skewness changes further seaward in the model results compared to the observations from negative to positive, in addition to strong observed variations in the observed skewness. These were likely caused by local factors in the field. Short wave asymmetry and skewness were limited to the frequency range 0.05-0.3 Hz, since observations showed that short waves generated in the Wadden Sea were propagating seaward. These might have affected the wave shape and sand stirring; however since no significant morphological changes were observed at the Wadden Sea side, their effect is probably small. Discrepancies between model and observations should not effect the general conclusions of our results, since we only compare each transport term in a relative sense for changes in island geometry and forcing. However, it would be of interest to be able to compare the magnitude of each forcing term with each other to find the relative importance of each term. Hopefully this will be addressed in future research.

Our results were affected by the choices we made a.) in the SWASH implementations, and b.) in the use of parameters for the transport models. SWASH in 1-D mode leads, as mentioned earlier, to an overestimation of IG waves, and therefore transport and stirring by infragravity waves is surely overestimated. Further, since we had no means to fit the parameters for the transport model, we chose values from the literature and combined them to find reasonable predictions for the transport processes. However, the choice of $\varepsilon_b = 1.03$ and $K_a = 0.37 \text{ kg s m}^{-2}$ is open for debate. Bagnold (1966) initially suggested a value of 0.13 for ε_b , while Bailard (1981) set $\varepsilon_b = 0.21$ after calibration to field data. Drake and Calantoni (2001) found $\varepsilon_b = 1.03$ for their discrete particle model which is about eight times the value Bagnold (1966) originally proposed for steady unidirectional flow. On the other

hand, Drake and Calantoni (2001) determined $Ka = 0.07 \text{ kg s m}^{-2}$, while Hoefel and Elgar (2003) attained $Ka = 0.37 \text{ kg s m}^{-2}$ when comparing model with observational data, which is higher by a factor of 5. This clearly shows that there is uncertainty in the absolute numbers, and any use of the transport model to estimate the actual transport would require careful calibration. However, the acceleration under the steep faces of asymmetric waves is assumed to contribute significantly to sand transport over bars and in the shallow surf-zone (Elgar et al., 2001; Hoefel and Elgar, 2003; Ruessink et al., 2009; Brinkkemper et al., 2018), and Brinkkemper et al. (2018) found short wave sand transport not be related to the short wave skewness in low-energy conditions in the shallow surf zone. Therefore, while the relative importance of the transport terms might be not a hundred percent accurate, their relationship seems realistic, which allowed us to investigate how sand transport processes are influenced by bed slopes and hydrodynamic forcing.

Lastly, our choice of using only the bedload part of the Bailard (1981) equation ignores the suspended sand transport, which was shown to be important during the inundation of a barrier island in the Wadden Sea (Engelstad et al., 2018b, Chapter 3). During suspended sand transport, the transport direction can be affected by phase lags between the suspended sand and the wave velocity. For example, sand suspended into the water column under the crest (landwards directed velocity) can be transported seaward under the trough if settling is slow (Hoefel and Elgar, 2003; Grasso et al., 2011; Ruessink et al., 2011). This was not observed in the field (Engelstad et al., 2018b, Chapter 3), probably because the bed was very smooth and ripples small. This might be different for uneven terrain. Therefore, suspended sand transport and the possible reversal of transport should be addressed for these cases in future research.

4.5 Conclusions

The non-hydrostatic wave model SWASH was used to investigate the relative importance of bedload transport processes, such as transport by mean flow, short- and IG waves, and acceleration skewness, during barrier island inundation for various island configurations and hydrodynamic forcing. Simulations suggested that the sand transport processes from the outer surfzone until landwards of the island crest are dominated by the waves. These either transported sand directly or stirred the sand for the mean flow transport. Transport by short waves was continuously landwards directed, while IG wave transport was seaward directed in the outer surfzone and landward directed in the inner surfzone, consistent with earlier observations. Landwards of the crest, bedload transport was mostly dominated by the mean flow, which was forced by the water-level gradient. A critical threshold exists between wave set-up, which depends on the offshore wave forcing and inundation depths, and basin water levels. These determine the mean-flow transport direction and magnitude in the inner surfzone and on the island top.

Model results suggest that short wave and mean flow transport is enhanced on steeper slopes throughout the domain, since they cause less energy dissipation and higher flow velocities. Further modifications of the island geometries suggested that the the slope of the island top and the width of the island foremost affect the mean-flow transport, while changes in inundation depth will also affect transport by short-wave acceleration skewness.

Chapter 5

Synthesis

This thesis aims to increase our understanding of the hydrodynamics and sand transport processes on intra-wave to tidal time scales during the inundation of a Wadden Sea barrier island. To this end, the hydrodynamic forcing mechanisms were investigated using collected field data (Chapter 2). Next, sand suspension and transport mechanism at the beach crest were explored, again by using collected field data (Chapter 3). Finally, a numerical model, SWASH, combined with a bedload velocity-moment approach, was used (Chapter 4) to assess the effect of island geometry and hydrodynamic forcing on sand stirring and transport. Below, the main conclusions are outlined and a general picture of the hydrodynamic and sand transport processes across a Wadden Sea barrier island is drawn. Lastly, the generality of the present results for other barrier islands is discussed and suggestions for future research are given.

5.1 Main findings

1. *What are the hydrodynamic processes during inundation?*

Barrier islands in the Wadden Sea are generally wide (> 1 km) with high (~ 10 m) fore-dunes, but especially the island tails can be low-lying. The shallow back barrier basin is aligned west to east (allowing for wind wave growth). Tidal inlets are separating the islands, causing tidal phase differences between the North and the Wadden Sea. Storm surges can cause elevated water levels in the Wadden Sea and can force overwash and inundation, predominantly around high tide. To get a better understanding of the hydrodynamic processes during inundation in this system, field data were collected on the sandy (median grain size of $\sim 200 \mu\text{m}$), low-lying island tail of Schiermonnikoog (Chapter 2). The area was essentially alongshore uniform, and the cross-shore beach slope was gentle (1:120).

The field area was inundated eleven times during the first field campaign from November 2014 until January 2015 (Chapter 2) and at least eight times during the second campaign from November 2016 until January 2017 (Chapter 3). Offshore wave heights, in about 20 m water depth, ranged from 3-7.5 m while wave periods varied between 7 and 10 s. Inundation depths at the crest of the barrier island, which was the shallowest point in the profile (1.7 m over mean water level, MWL), ranged from 0.3 to 1.5 m (Chapter 2 and 3). Short (0.05-1 Hz) and infragravity waves (0.005-0.05 Hz) propagated across the inundated island without completely losing their energy, which was also found in numerical modeling results (Chapter 4). Observed short wave heights ranged from 0.15 to 0.65 m at the crest during high tide. They increased slightly towards the Wadden Sea side (by \sim

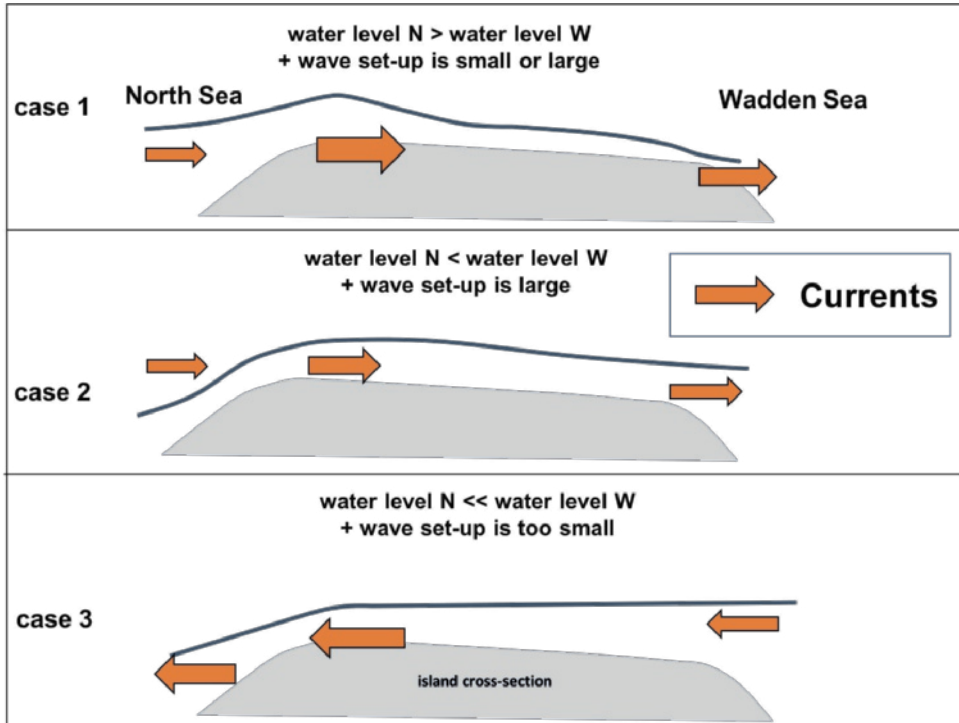


Figure 5.1: Summary of the mean flow directions for variations in water levels.

0.15 m), which was caused by short waves generated in the Wadden Sea propagating seawards. Infragravity wave heights were similar in height to the short waves, indicating their importance during inundation. Infragravity waves were regularly observed to propagate as bores, especially in shallow water depths, indicating wave breaking. In fact, as for short waves, the main dissipation mechanism for infragravity waves was determined to be wave breaking, consistent with observations on gentle sloping closed beaches (Van Dongeren et al., 2013; De Bakker et al., 2014). While in the field area the beach slope was gentle and varied between 1:80 and 1:120, many natural beaches and barriers have a steeper seaward slope. Numerical modeling results suggested (Chapter 4) that infragravity and short waves dissipate less energy on a steeper (1:30) slope compared to a gentler (1:120) slope, resulting in higher waves.

Mean cross-shore flow velocities landwards of the crest were generally highest before high tide (max 0.2 - 1.2 m/s, Chapters 2 and 3), but strongly decreased after high tide and at times even reversed (max -0.2 m/s). Mean alongshore flow velocities were of equal magnitude as cross-shore flow velocities and exceeded these at times (Chapter 3). Mean cross-shore flow velocities landwards of the crest were largely driven by the difference in water levels. Water levels in the North and Wadden Sea are forced by the tide and the storm surge and can result in a water-level gradient, here considered as the large scale water-level gradient. Additionally, wave breaking increases water levels around the beach crest, causing a local water-level gradient between crest and Wadden Sea. We identified three cases based on observations and model results (Chapters 2-4) that explain the variation in

cross-shore flow velocities. If water levels were higher in the North- than in the Wadden Sea, the mean flow was directed towards the Wadden Sea (case 1, Figure 5.1), and largest just landwards of the crest. This was usually the case before high tide if water levels in the Wadden Sea were not elevated by the storm surge. However, frequently water levels in the Wadden Sea were higher than in the North Sea even before high tide (case 2, Figure 5.1) due to the storm surge. Oftentimes, the local water levels at the crest were able to exceed the Wadden Sea water levels, even though the water level in the North Sea was lower. This was caused by the before-mentioned wave set-up. This forced the mean cross-shore flow to be still landwards directed, although the higher Wadden Sea water level decreased the cross-shore flow velocity. After high tide, the water levels in the North Sea dropped faster due to tidal phase differences, increasing the large-scale water-level gradient (case 3, Figure 5.1). If it increased enough, the wave set-up was no longer able to compensate for the higher water level in the Wadden Sea and the mean flow direction reversed. The balance between wave set-up and the large-scale water-level gradient induced by the tide and storm surge, depends on the offshore wave forcing and the inundation depth (determining the wave set-up) and the storm surge (determining the gradient). The inundation depth determines the location of wave breaking and therefore the amount of wave energy at the beach crest. Additionally, model results suggest that, due to the higher waves and continued breaking after the crest, wave set-up is higher for a steeper slope.

Observations and model results (Chapters 2-4) showed that the hydrodynamic processes during inundation are affected by the processes in the Wadden Sea, especially the modification of the cross-shore flow through elevated water levels. While significant flow reversal was limited for the field area (max seaward velocity was 0.2 m/s), the main effect is the slowing of flow velocities especially after high tide.

2. *What are the sand transport processes during inundation and how are these affected by variations in island geometry and hydrodynamic forcing?*

Observations (Chapter 2) showed that short and infragravity wave energy was not completely dissipated as waves propagated over the submerged field site, and that mean flow velocities varied greatly during the tide stage and between inundation events. In order to assess sand suspension and cross-shore transport in these conditions, first field data were collected (Chapter 3) in the same location as for Chapter 2. Since observational data were available at location of the crest only, the analysis was then extended to include the region from the shoaling zone to the back barrier basin under varying cross-shore geometries and hydrodynamic forcing, using the numerical model SWASH coupled to a bedload velocity-moment model (Chapter 4).

- a) *What is the relative importance of waves and currents in sand stirring and transport and what is the transport direction?*

Observations showed (Chapter 3) that the net depth-integrated suspended sand transport was highest (max 3.8 kg m s^{-1}) before high tide, and that $\sim 80\%$ of the sand transport was completed before high tide. The duration of the recorded sand transport varied between 2-5 hours around high tide, depending on inundation depth and instrument availability. The transport was landwards directed for almost the entire time (the maximum seaward directed transport was 0.03 kg m s^{-1}), even though water levels in the Wadden Sea were frequently higher than in the North Sea. Variations in the transport magnitude during the tidal cycle were related to the difference in mean flow velocities, as discussed above and in Chapter 2. While

the mean flow transport was certainly the most important transport mechanism (relative contributions of up to 0.98), the relative importance of infragravity waves to the total net transport increased to more than 0.2 when mean flow velocities were low ($< \sim 0.5$ m/s) up to a maximum of ~ 0.8 , which was generally the case after high tide. The contribution of short waves to the sand transport, on the other hand, was negligible (max 0.17). While the relative importance of waves to the total sand transport over the duration of the inundation was thus small, they were important to the suspension of sand. Episodically high depth-integrated suspended sand concentrations (defined as > 2 kg/m²) were commonly found to coincide with the crest of infragravity bores. Since the deeper water depths under infragravity wave crests allow for higher short waves (Abdelrahman, 1986; Tissier et al., 2015), these high concentrations were probably forced by the combined bed shear stresses of mean flow, short and infragravity waves. From the observations, we hypothesized that two transport regimes govern the transport during inundation: a flow-driven regime when flow velocities are high (> 0.5 m/s) and infragravity wave related bed shear stresses are low, and an episodic regime when these bed shear stresses are high and mean flow velocities are relatively low (< 0.5 m/s).

b) *What are the effects of island geometry and hydrodynamic forcing on sand transport?*

Research on closed beaches has shown that sand transport processes differ for variations in beach slope steepness (for a review see Aagaard et al., 2013). In addition, our observations showed that offshore wave heights and water levels in the basin varied greatly (Chapter 2 and Chapter 3). To explore these effects further, and to gain a synoptic view of spatially varying transport processes from the shoaling zone to the back barrier basin, the numerical model SWASH was used in Chapter 4 to simulate the hydrodynamics. This also allowed us to change the island cross-shore geometry and the hydrodynamic forcing so that we could explore the effect that changes therein have on sand transport. To estimate stirring and bedload transport for waves and mean flow, a bedload transport model (Baillard, 1981) was used. Even though results in Chapter 3 showed the importance of suspended sand transport in our field area, this simplified the analysis. We assume that wave and current processes have the same (relative) importance for suspended load as for bedload processes, since both are a function of flow velocity (to the power of 3 for bed load and to the power of 4 for suspended load), and so here we only considered the time-averaged cross-shore bedload transport and ignored suspended-load and gravity-driven transport.

Model results indicated that short and infragravity waves dominate the sand transport from the shoaling zone until shortly after the crest, either by directly transporting sand or by stirring the sand which was transported by the mean flow. Mean flow transport was most important around the crest and dominated the transport on the island top. Results further suggested that the short wave transport was entirely on-shore directed, while the infragravity wave transport and the mean flow transport was offshore directed in the shoaling and outer surfzone, but changed direction to a landwards transport in the inner surfzone. While wave transport directions were consistent with observations in closed beach systems (e.g. Elgar et al., 2001; Ruessink et al., 2011; Drake and Calantoni, 2001; De Bakker et al., 2016), mean flow transport in the closed surfzone is generally seawards directed (e.g. Gallagher et al., 1998; Ruessink et al., 1998a). All transport over the beach crest (the highest point in the profile) and on the submerged island was landwards directed as long as the water level in the basin was only slightly higher (here 0.15 m) than on the ocean side. Increases in the

basin water level (to 0.55 m) showed that while high offshore wave forcing (7.45 m) prevented the reversal of the mean flow landwards of the crest, smaller wave forcing (4.55 m) lead to seaward directed mean flow transport throughout the domain since wave set-up was reduced. Model results indicated that all transport terms were increased during higher offshore wave forcing, since stirring, cross-shore velocities and wave set-up was increased. On a steeper (1:30) slope, compared to a gentler (1:120) slope, less short- and infragravity wave energy was dissipated. This resulted in continued breaking landwards of the crest, higher wave set-up and mean flow velocities. Simulations indicated that sand transport was more than twice as high for the steeper slope. Reducing the slope of the island top and the width of the island foremost increased the mean flow transport across the island top, according to model results. Mean-flow and acceleration skewness transport increased seaward and decreased landward of the crest, reflecting the erosion and deposition pattern (landward translation) in the observed profile change during the second field campaign (compare lines for November 2016 and January 2017 Figure 5.2).

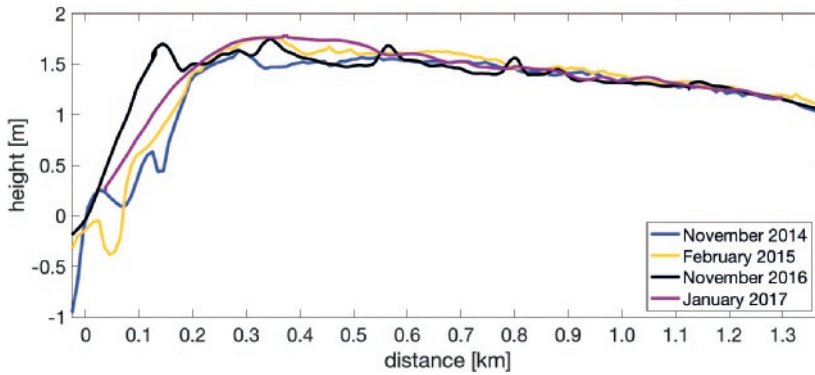


Figure 5.2: Initial barrier island cross-shore profile at the beginning (blue line) and the end (yellow line) of the first field campaign and the beginning (black line) and end (magenta line) of the second campaign. The vertical datum is NAP (Dutch Ordnance Datum), where 0 m NAP corresponds to mean sea level.

The main findings for transport across an inundated barrier island from Chapter 3 and 4 are summarized in Figure 5.3. Note that the arrow size is not to scale and just shows a general trend. If the water level in the Wadden Sea is lower than in the North Sea the landward transport by the mean flow is large, while transport by waves is relatively small (Figure 5.3a). Even with elevated water levels in the basin, the mean flow transport on the island can be directed landwards (Figure 5.3b), but the mean flow transport will be reduced and the relative importance of (infragravity) wave transport increases. However, if wave heights are too small (Figure 5.3c) or the water-level gradient is too large (Figure 5.3d), the mean transport will be seaward directed. Smaller wave heights additionally reduce the wave transport and the stirring for transport by the mean flow. A steeper ocean side slope will increase the wave and mean flow transport (compare Figure 5.3b and e), since waves dissipate less energy. On the other hand, a reduction in the basin side slope (e.g. a flat top) will increase the mean flow transport on the basin side (Figure 5.3f). While for wider islands the transport decreases on the island top (causing accretion), narrow islands will experience transport into the basin (note the dark gray line in Figures 5.3a, b, c and d)

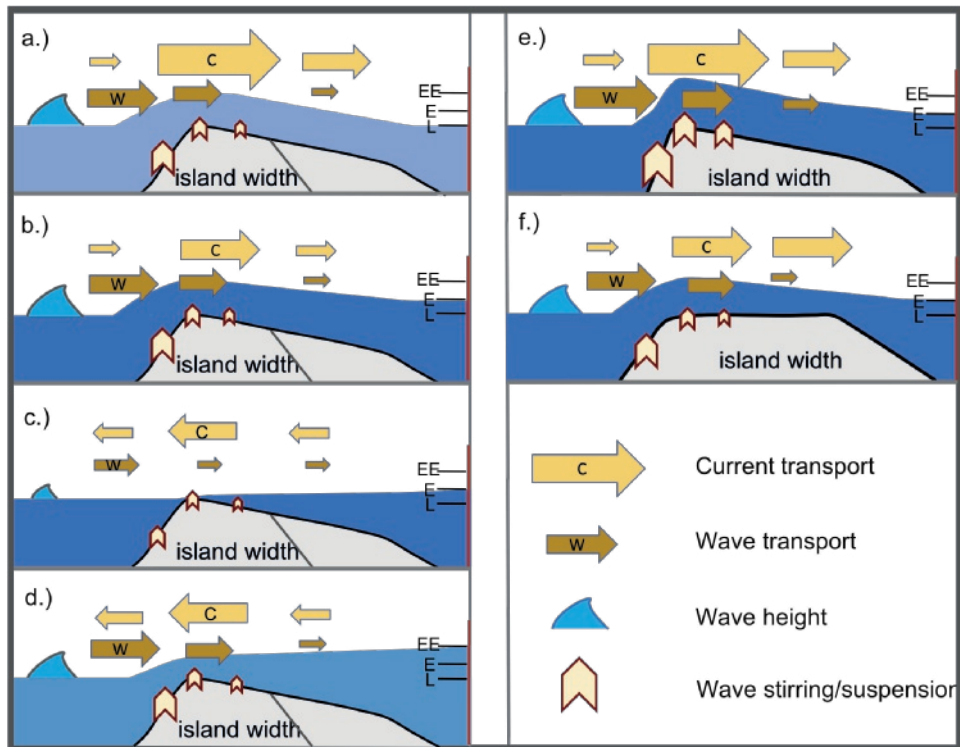


Figure 5.3: Summary of sand transport for a gentle (a., b., c., d., and f.) and a steep (e.) beach slope, under different wave forcing (a., b., d., e. and f. compared to c.) and for a straight island top (f.). Differences in water levels (blue) between ocean (left side of figure) and basin (right side) are the same for b., c., e., and f. with elevated water levels in the basin (shown in the same shade of blue and indicated by E on the axis to the right) while the water level is at the same level for a. on both sides (L on axis), and extremely elevated on the basin side in d. (EE on axis). The island is shown as a cross-section, where the gray line indicates a narrower island.

5.2 Discussion and perspectives

5.2.1 Wadden Sea barrier island response compared to other systems

The tidal system, storm forcing and island geometry determine the barrier islands response to inundation in the Wadden Sea and differs from those found in other systems, such as in the US. The barrier islands in the Wadden Sea are unique since the island shape is usually short and wide (drumstick shape) compared to the narrow, elongated barriers found in other systems, while storm-forced wave heights are large (Chapter 1). Even though water levels in the Wadden Sea were frequently higher than in the North Sea (Chapters 2 and 3), offshore wave heights were generally large enough to force a wave set-up which elevated the water level at the crest enough so that the mean flow direction was mostly landwards directed. The observations suggest that barrier islands in the Wadden Sea, which are subjected to relatively large offshore wave forcing during inundation (observed 3-7.4 m) in combination with moderately elevated water levels (max 0.55 m observed where the largest values roughly coincide with the largest wave forcing) are not prone to large-scale seaward transport which can potentially remove sand from the area (e.g. Goff et al., 2010). This is different for barrier islands along the US East coast which are frequently impacted by hurricanes. These experience

severe seaward transport during the storm surge ebb (Kahn and Roberts, 1982; Goff et al., 2010; Sherwood et al., 2014; Harter and Figlus, 2017) due to the water-level gradient between basin and ocean, which can be caused by strong offshore winds, inland flooding or fast falling ocean water levels (see Sherwood et al. (2014) for a summary of processes). We hypothesize that the basin side water levels can drop faster in the Wadden Sea, since the narrow spacing and large cross-sectional area of the tidal inlets (due to significant tidal prisms) allows for a relative fast draining of water levels through the inlets. For long elongated islands, where inlets are few and spaced far apart, a strong offshore directed water-level gradient forces the flow across the island, resulting in the observed (Kahn and Roberts, 1982; Goff et al., 2010; Sherwood et al., 2014; Harter and Figlus, 2017) channels and offshore deposits.

Further, observations and model results showed that the mean flow was the main driver of sand transport over the submerged barrier island during inundation in the Wadden Sea. About 80% of the sand was transported before high tide, owing to large cross-shore velocities during this time. This suggests that the tidal regime in the Wadden Sea, with a tidal range of about 1.5 - 2.3 m, is an important factor in governing the sand transport. Microtidal systems (tidal range < 2 m), and barrier islands subjected to hurricane surges are likely not experiencing these variations to such an extent. While the mean flow was the main driver of sand transport in the crest region, observations and model results suggest that the mean flow transport would be considerably less without infragravity and short waves stirring and suspending the sand. Storms with lower wave forcing, such as in the US during storms and weak hurricanes, where offshore wave heights typically range between 3-4 m (Rosati and Stone, 2009), will result in less infragravity wave energy and therefore less stirring. Additionally wave set-up is reduced, resulting in less landward transport if the water-level gradient is directed towards the basin. This implies that an increase in offshore wave forcing results in more landward transport (by increasing a landward directed water-level gradient and sand stirring) and less seaward directed transport (by decreasing a seaward directed gradient).

In addition, the cross-shore distance over which sand accretion could be observed (Figure 5.2) and the modeling results from Chapter 4 indicate that wide islands, like the ones in the Wadden Sea, have a better chance to accrete sand (or to migrate slowly landwards) than narrow islands, which are more likely to experience sand transport into the basin during landward transport (Donnelly et al., 2006; Rosati and Stone, 2007; McCall et al., 2010). Observations showed no substantial sand deposition on the Wadden Sea site after ~ 0.8 km (Figure 5.2) which suggests that no sand was transported into the Wadden Sea. Instead, the net subaerial volume from North to Wadden Sea (~ 0.05 - 1.35 km in Figure 5.2) increased by $2 \text{ m}^3/\text{m}$ during the second field campaign (Chapter 3). This is probably aided by the island profile which is sloping down to the Wadden Sea. Model results indicate that for a flat island top, mean flow transport would reach the basin, since velocities increased landwards.

The observed change in the profile from 2016 to 2017 suggest further that the gain in sand landwards of the initial beach crest (compare November 2016 and January 2017 in Figure 5.2) was provided by sand from the beach and the initial location of the beach crest. This sand was available through significant sand accretion in the time between the two field campaigns during which the beach-crest area accumulated sand (~ 0.8 m, compare February 2015 and November 2016 in Figure 5.2). Since in the winter 2015/2016 the storm climate was mild, the accretion was likely caused by onshore and alongshore transport and by aeolian processes. While Schiermonnikoog for now has a sufficient supply of sand, probably due to readjustments in the tidal system as a response to recent man-made changes, other islands in the Netherlands are nourished to avoid shoreline retreat.

The unique setting of the Wadden Sea islands suggest that they have a higher potential to accrete sand than narrow, elongated islands in micro-tidal systems, especially compared to those affected by hurricanes.

5.2.2 Suggestions for future research

This study was dedicated to the investigation of cross-shore hydrodynamic and sand transport processes on intra-wave to tidal time scales. This improved our knowledge of sand transport processes during barrier island inundation; however, it can be expected that these processes will be more complex when considering (alongshore) profile variations and sand transport over cross- and alongshore directions. Observations showed that velocities and net transport in the alongshore directions were of the same magnitude as in the cross-shore (Chapter 3). This was accounted for in the evaluation of observed Shields parameters, which were used to investigate sand suspension, but it was ignored for example in the mean flow stirring in the numerical model (Chapter 4). Additionally, alongshore convergence might have contributed to changes in the observed sand volume. Further, the study side was chosen to be alongshore uniform to simplify the data analysis. However, Wesselman et al., 2019 described the importance of washover gaps (openings between high dunes) for barrier islands overwash and inundation in the Wadden Sea, which force higher flow velocities (contraction) through the gaps. This results in different transport patterns (such as erosion immediately before and in the gap and deposition thereafter) than observed in this study. It would be advisable for future studies to turn to area modeling to improve our knowledge of sand transport during inundation by including alongshore transport and profile variations.

The numerical model (SWASH) was run in 1-D mode to enable us to run several simulations in limited time. Our results suggest that short as well as infragravity waves need to be included in numerical models evaluating sand transport during inundation, especially given their importance in sand stirring and suspension (Chapters 3 and 4). However, it was not possible to determine the relative importance of short and infragravity waves in sand stirring and transport throughout the domain, given the overestimation of infragravity waves in 1-D mode. The overestimation of infragravity waves can be reduced by focusing on area modeling as mentioned above. Additionally, estimates of sand transport could be improved by including bedload and suspended load transport, since observations (Chapter 3) demonstrated the importance of suspended sand.

The above discussed beach accretion between the two field campaigns and the formation of small dunes (including vegetation) between February 2015 and November 2016 (Figure 5.2) suggest that aeolian transport is an important factor for the redistribution of sand in the field area. However, the importance of aeolian transport in the landward transport of sand is unknown. While the results of the field campaign and the modeling study suggest that barrier islands in the Wadden Sea have a good potential to accrete sand, the work presented here will certainly be improved by extending it to include morphological feedback, beach recovery, and aeolian transport.

More insight could be gained by carrying out pilot projects on barrier islands to increase the natural dynamics as it is considered for the Boschplaat on Terschelling, the Netherlands (<https://www.boschplaatvisie.nl>, in Dutch only). The vision for this project is that by restoring dynamics, for example by creating gaps in the sand drift dikes and thereby allowing wind and water to move sand again, biodiversity will be improved and sand starved parts of the island can grow again vertically. Of course, such interventions need to be closely monitored, but they will certainly provide valuable insight into the barrier systems processes and can ver-

ify if dynamic sections will indeed accrete sand. Further, such an intervention would allow for research on the interplay of aeolian transport and overwash and inundation processes.

Even for natural dynamic systems the question remains if sand accretion will be sufficient to keep up with rising sea levels. The projected change in sea levels for the Wadden Sea ranges from 0.41 m to 0.76 m (Vermeersen et al., 2018) depending on the climate change scenario for the period between 2018 and 2100, which could force the drowning of individual tidal flats when a critical value is reached (van der Spek, 2018; Wang et al., 2018). This is projected for the more severe sea level rise scenarios (van der Spek, 2018; Wang et al., 2018), but it is unclear if there is also a threshold for the survival of the barrier islands in the Wadden Sea. A review by Eitner (1996) of several scenarios for barrier response due to rising sea levels, highlighted the potential for East Frisian Wadden Sea islands to migrate landwards, either while keeping their original size or with a reduction in island width. All of these scenarios assume that the islands could move freely, which is not given for most islands. However, FitzGerald et al. (2018) pointed out that in order to be able to predict the fate of barriers, it is necessary to have a better understanding of the local transport paths of sand, such as losses to the offshore, alongshore, and into the tidal deltas, while the impact of these losses needs to be established by comparison with adjacent barrier volumes. Future studies will hopefully investigate this further, and could also take the potential of sand nourishments for barrier survival into account.

Appendix A

Validation of SWASH results

This is part of the publication: Engelstad, A., Ruessink, B. G., Hoekstra, P., van der Vegt, M. (2019). Sediment transport processes during barrier island inundation under variations in cross-shore geometry and hydrodynamic forcing. Submitted to Journal of Marine Science and Engineering.

In Chapter 4 we simulated the hydrodynamics using the SWASH model. Here we show results for a model-data comparison, including the boundary conditions and model settings.

A.1 Boundary conditions and model settings

For the model-data comparison four of the five observed inundation events were used (there was doubt about the measured water levels during the fifth event; Table A.1). Observational data were averaged over the first 15 minutes of each full hour from 2 hours before until 2 hours after high tide to have 5 data-points if records were long enough (flooding 1 and 4). Otherwise, 3 data-points (1 hour before to 1 hour after high tide) were used (flooding 2 and 3). The 15-minute average was chosen because conditions were not stationary due to the tidally induced changes in water levels.

Table A.1: Boundary conditions for observed floodings at high tide ^a

flooding #	wind speed [m/s]	wind direction [°]	wave Hs [m]	wave T [s]	wave θ [°]	water level N. Sea [m]	water level W. Sea [m]
1	16	270	6.20	8.7	307	2.34	2.52
2	11	300	5.11	8.3	327	1.84	2.19
3	15	310	4.55	7.2	321	2.05	2.16
4	20	330	7.43	10.1	326	2.50	2.92

^a Wind speed and direction as well as significant wave height (Hs), periods (T) and wave angle (θ) were measured by an offshore meteorological station (Wierumergronden) and a wave buoy (Schiermonnikoog Noord) and were averaged over one hour at high tide. Water levels (wl) in the North Sea (N. Sea, measured at Huibertgat) and Wadden Sea (W. Sea, measured at Schiermonnikoog station) were also averaged over one hour at high tide. The coastline is aligned ~ 10 degrees with true East.

Water levels created the largest uncertainty in the model-data comparison, since offshore water levels were only available relatively close to shore (as mentioned above) in a water depth of roughly 5 m and for the basin at a distance of about 10 km to the west of the field side.

While the tidal station Schiermonnikoog is close to the tidal inlet west of the island, the field site was close to the inlet to the east and water levels might not have been the same.

The bottom profile for the model-data comparison (Chapter 4, Figure 4.2b) is a combination of the measured island profile during the instrument deployment and offshore measurements available from Rijkswaterstaat (RWS). The existing bar-trough morphology was simplified to a straight line from 20 to 2.5 m depth and was extended at the seaward and the basin side of the transect (km 0-1 and \sim km 14-17), resulting in a total domain length of \sim 17.5 km. A profile measured at the beginning of the campaign (Chapter 4, Figure 4.2a) was used for flooding 1-3, while the final profile survey was used for flooding 4.

In the model data comparison, the best agreement for flooding 1-3 was found with breaking parameter α set to 0.5 and the criterion for the persistence of wave breaking, $\beta = 0.25$, while for flooding 4 $\alpha = 0.4$ and $\beta = 0.2$ provided best agreement. To account for the high observed cross-shore velocities, Manning's roughness coefficient, n was set to 0.14 and 0.1 for floodings 1-3 and flooding 4, respectively.

A.2 Model-data comparison

To investigate the ability of the SWASH model to hindcast the hydrodynamic conditions observed in the field, we compared observed and modeled water levels, cross-shore velocities, IG and short wave heights during the rising and falling tide for flooding 1 along the instrument transect (Figure A.1). Despite the uncertainty in water levels, modeled and observed water levels agree well (Figure A.1a, e, and i) during different tidal stages. The model accounts for the fact that even if water levels are higher in the Wadden Sea, wave set-up can still create a water level gradient that is directed towards the Wadden Sea. A comparison for all floodings shows (Figure A.2a) a maximum offset of 0.14 m and an r^2 value of 0.95 with no bias.

Predicted mean velocities show satisfactory agreement with the observations for flooding 1 (Figure A.1), albeit they were underestimated during high tide by \sim 0.13 m/s. Generally, the model underestimated higher mean flow velocities (> 0.3 m/s) up to 0.3 m/s (Figure A.2b), either because the implemented water levels were not correct, or the model was misrepresenting some local or physical processes.

While predicted short-wave heights showed good agreement with the observations for the first 3-4 locations on the North Sea side (Figure A.1c, g, and k), they were increasingly underpredicted towards the Wadden Sea, which can be seen in Figure A.2c for all floodings (with a maximum underestimation of \sim 0.29 m). This was expected since waves generated in the Wadden Sea were observed to propagate seawards (Engelstad et al., 2017, Chapter 2), which was ignored in the model implementation. Infragravity-wave heights, on the other hand, were consistently overestimated (Figure A.1d, h, and l and Figure A.2d), especially on the North Sea, side by roughly a factor of 2. This was caused by our choice of using a 1-D model (see Section 4.2.1) and hence the neglect of wave spreading on IG waves. The overestimation of IG waves might also have contributed to the underestimation of mean flow velocities by increasing the bottom friction which slows the flow.

In order to compare the wave shape, short-wave asymmetries and skewness were limited to the frequency range 0.05-0.3 Hz to exclude waves propagating seaward from the Wadden Sea (Engelstad et al., 2017, Chapter 2) and locally generated wind waves. Predictions of wave asymmetry and skewness show that the model is able of capturing the general trends (Figure A.3). While short-wave asymmetry was overpredicted by far (Figure A.4), the locations

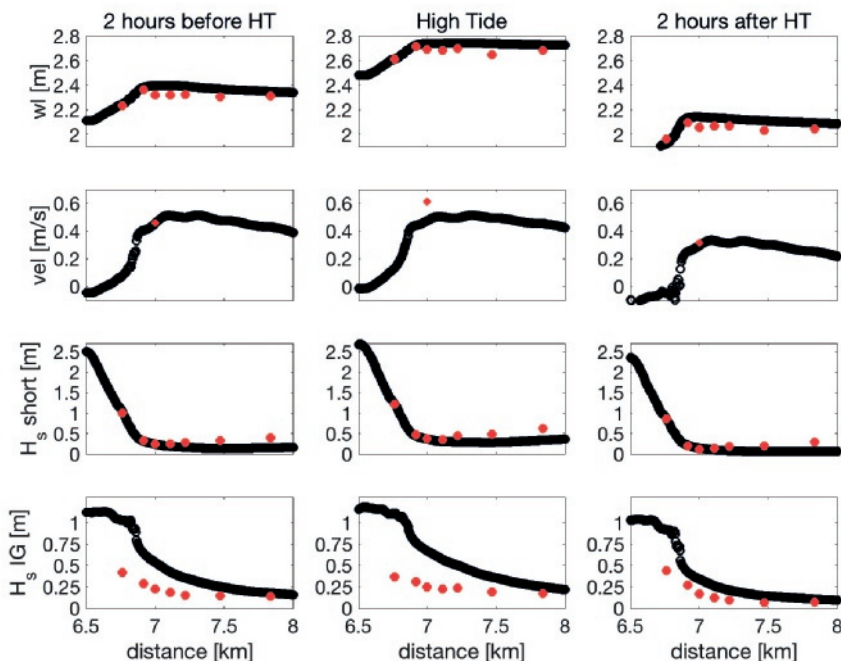


Figure A.1: Observed (red) and modeled (black) water levels (wl, a, e, and i.), cross-shore velocities (vel, b, f, and j.), short (c, g, and k.) and IG (d, h, and l.) significant wave heights (H_s) from 2 hours before to 2 hours after high tide (HT) for flooding 1. The North Sea is to the left and the Wadden Sea to the right in this graph.

of the highest asymmetry (between $x = 6.9$ and $x = 7.2$ km, Figure A.3a, c, and e) were captured, as well as the changes during the tidal stages with the lowest asymmetries during high tide and the highest at two hours after high tide. Short-wave skewness was captured well.

IG wave asymmetry was, as for short waves, highly overpredicted (Figure A.3b, d and f), which was possibly caused by the overprediction of IG wave heights. However, the slight continuous increase two hours before high tide (Figure A.3b), as well as the decrease at the location closest to the basin (Figure A.3f) were captured by the model. The observed negative IG wave skewness and the following increases and decreases in positive IG skewness on the island were captured well for flooding 1, with the exception of the location closest to the Wadden Sea for which the observed skewness suddenly increased again. However, the r^2 value (0.075) show little relationship between observed and modeled IG skewness (Figure A.4d), even though we only considered the first three locations to avoid any interference from the Wadden Sea processes. This is probably caused by a later (more landward) transformation of the observed IG skewness from negative to positive (see e.g. Figure A.3b and d), in addition to local variations in observed IG skewness (see Figure A.3a, the third location from the North Sea). Generally, observed wave asymmetry and skewness fluctuated strongly from one instrument location to the other, especially for IG asymmetry and skewness (Figure A.3b, d and f).

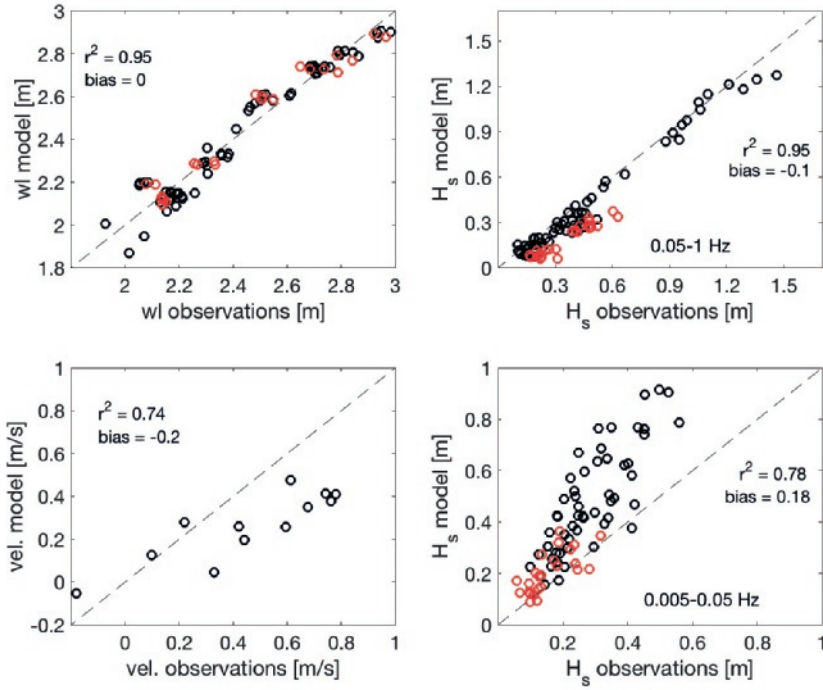


Figure A.2: Observed and modeled water levels (wl, a.), cross-shore velocities (vel, b.), and short- (c.) and IG (d.) significant wave heights (H_s) for all 4 floodings from 1 hour before until 1 hour after high tide (hourly output). The red circles indicate measurements at P5 and P6, the instruments closest to the Wadden Sea.

SWASH was able to reproduce the varying water levels including wave set-up and increased water levels in the Wadden Sea, short wave heights and cross-shore velocities reasonably well over a wide range of observed hydrodynamic conditions and tidal stages. While IG wave heights and wave asymmetries were largely overpredicted, SWASH reproduced the general trends seen in the observations, including the negative skewness. This suggests that the SWASH model is suited for an exploratory investigation of wave and current related sand transport processes when focusing on the changes of each process (current-, IG- and short wave related bedload transport), under varying island geometries and hydrodynamic forcing.

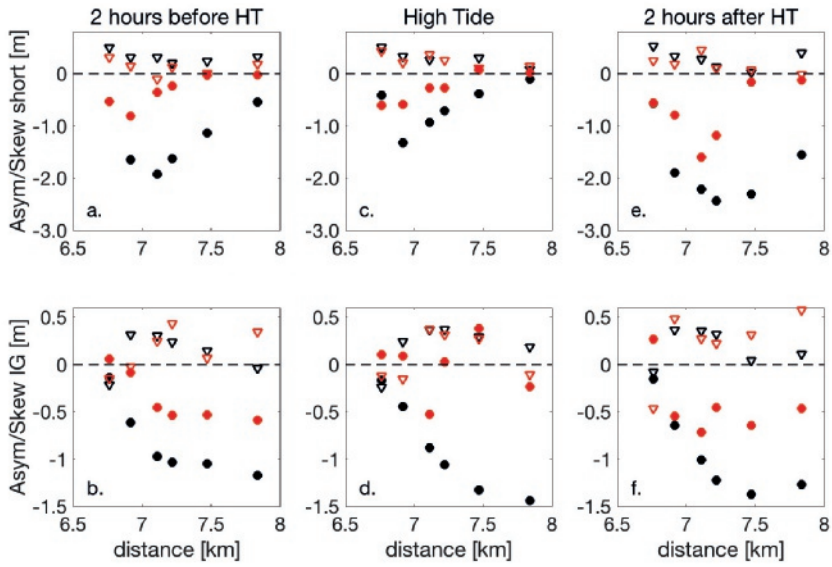


Figure A.3: Observed (red) and modeled (black) wave asymmetry (dots) and skewness (triangles) from 2 hours before (a. and b.) high tide (HT), at HT (c. and d.) and 2 hour after HT (e. and f.) for flooding 1. The North Sea is to the left and the Wadden Sea to the right in this graph.

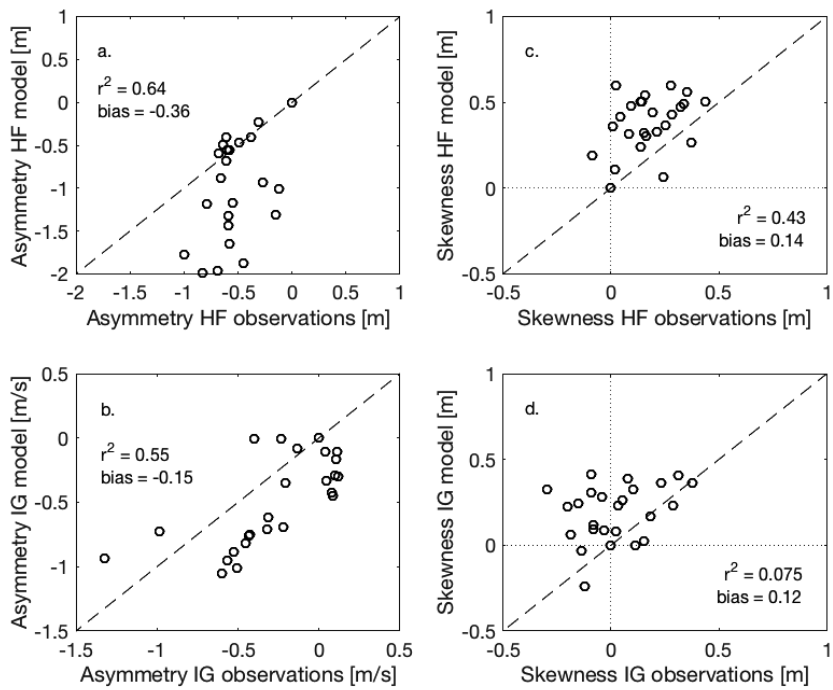


Figure A.4: Observed and modeled short (HF, a. and c.) and infragravity (IG, b. and d.) wave asymmetry (a. and b.) and skewness (c. and d.) for all 4 floodings from 1 hour before until 1 hour after high tide (hourly output) for the first three instrument locations on the North Sea side.

References

- Aagaard, T. and B. Greenwood (1994). Suspended sediment transport and the role of infragravity waves in a barred surf zone. *Marine Geology* 118, pp. 23–48. DOI:10.1016/0025-3227(94)90111-2.
- Aagaard, T., B. Greenwood, and M. Hughes (2013). Sediment transport on dissipative, intermediate and reflective beaches. *Earth-Science Reviews* 124, pp. 32–50. DOI:10.1016/j.earscirev.2013.05.002.
- Abdelrahman, S. M. M. (1986). *Short wave modulation due to infragravity waves in the nearshore zone, with applications*.
- Bagnold, R. A. (1966). An Approach to the Sediment Transport Problem from General Physics. *U.S. Geological Survey Professional Paper* 422-I. DOI:10.1017/S0016756800049074.
- Bailard, J. A. (1981). An energetics total load sediment transport model for a plane sloping beach. *Journal of Geophysical Research: Oceans* 86.C11, pp. 10938–10954. DOI:10.1029/JCo86iC11p10938.
- Bodde, W., A. Pomeroy, A. van Dongeren, R. Lowe, and J. van Thiel de Vries (2014). Hydrodynamic drivers of sediment transport across a fringing reef. *Coastal Engineering Proceedings* 1.34, p. 37. DOI:10.9753/ICCE.V34.CURRENTS.37.
- Brinkkemper, J. A., A. T. M. de Bakker, and B. G. Ruessink (2017). Intrawave sand suspension in the shoaling and surf zone of a field-scale laboratory beach. *Journal of Geophysical Research: Earth Surface* 122.1. 2016JF004061, pp. 356–370. DOI:10.1002/2016JF004061.
- Brinkkemper, J. A., T. Aagaard, A. T. M. de Bakker, and B. G. Ruessink (2018). Shortwave Sand Transport in the Shallow Surf Zone. *Journal of Geophysical Research: Earth Surface* 123.5, pp. 1145–1159. DOI:10.1029/2017JF004425.
- Butt, T. and P. Russell (1999). Suspended sediment transport mechanisms in high-energy swash. *Marine Geology* 161.2, pp. 361–375. DOI:10.1016/S0025-3227(99)00043-2.
- Christiansen, C., T. Aagaard, J. Bartholdy, M. Christiansen, J. Nielsen, N. Nielsen, J. B. Pedersen, and N. Vinther (2004). Total sediment budget of a transgressive barrier-spit, Skallingen, SW Denmark: A review. *Geografisk Tidsskrift-Danish Journal of Geography* 104.1, pp. 107–126. DOI:10.1080/00167223.2004.10649508.
- De Bakker, A. T. M., M. F. S. Tissier, and B. G. Ruessink (2015). Beach steepness effects on nonlinear infragravity-wave interactions: A numerical study. *Journal of Geophysical Research: Oceans* 121.1, pp. 554–570. DOI:10.1002/2015JC011268.
- De Bakker, A. T. M., M. F. S. Tissier, and B. G. Ruessink (2014). Shoreline dissipation of infragravity waves. *Continental Shelf Research* 72, pp. 73–82. DOI:10.1016/j.csr.2013.11.013.
- De Bakker, A. T. M., J. A. Brinkkemper, F. van der Steen, M. F. S. Tissier, and B. G. Ruessink (2016). Cross-shore sand transport by infragravity waves as a function of beach steepness. *Journal of Geophysical Research: Earth Surface* 121.10. 2016JF003878, pp. 1786–1799. DOI:10.1002/2016JF003878.
- Dolan, R., H. Lins, and U. S. N. P. Service (1985). *The Outer Banks of North Carolina*. Geological Survey professional paper. U.S. Government Printing Office.
- Donnelly, C. (2007). Morphologic Change by Overwash: Establishing and Evaluating Predictors. *Journal of Coastal Research* SI 50 (special issue), pp. 520–526.
- Donnelly, C., N. Kraus, and M. Larson (2006). State of Knowledge on Measurement and Modeling of Coastal Overwash. *Journal of Coastal Research* 22.4, pp. 965–991. DOI:10.2112/04-0431.1.

- Drake, T. G. and J. Calantoni (2001). Discrete particle model for sheet flow sediment transport in the nearshore. *Journal of Geophysical Research: Oceans* 106.C9, pp. 19859–19868. DOI:10.1029/2000JC000611.
- Durán, R., J. Guillén, A. Ruiz, J. A. Jiménez, and E. Sagristà (2016). Morphological changes, beach inundation and overwash caused by an extreme storm on a low-lying embayed beach bounded by a dune system (NW Mediterranean). *Geomorphology* 274.Supplement C, pp. 129–142. DOI:10.1016/j.geomorph.2016.09.012.
- Edge, B. L., Y. H. Park, and M. Overton (2007). Experimental study of overwash. In: *Proceedings Coastal Sediments*. Vol. 7, pp. 2074–2083. DOI:10.1061/40926(239)163.
- Eitner, V. (1996). Geomorphological response of the East Frisian barrier islands to sea-level rise: an investigation of past and future evolution. *Geomorphology* 15.1, pp. 57–65. DOI:10.1016/0169-555X(95)00116-M.
- Elgar, S. and R. T. Guza (1985). Observations of bispectra of shoaling surface gravity waves. *Journal of Fluid Mechanics* 161, 425–448. DOI:10.1017/S0022112085003007.
- Elgar, S., T. H. C. Herbers, and R. T. Guza (1994). Reflection of Ocean Surface Gravity Waves from a Natural Beach. *Journal of Physical Oceanography* 24.7, pp. 1503–1511. DOI:10.1175/1520-0485(1994)024<1503:ROOSGW>2.0.CO;2.
- Elgar, S., E. L. Gallagher, and R. T. Guza (2001). Nearshore sandbar migration. *Journal of Geophysical Research: Oceans* 106.C6, pp. 11623–11627. DOI:10.1029/2000JC000389.
- Elgar, S., B. Raubenheimer, and R. T. Guza (2005). Quality control of acoustic Doppler velocimeter data in the surfzone. *Measurement Science and Technology* 16.10, p. 1889. DOI:10.1088/0957-0233/16/10/002.
- Engelstad, A., B. Ruessink, D. Wesselman, P. Hoekstra, A. Oost, and M. van der Vegt (2017). Observations of waves and currents during barrier island inundation. *Journal of Geophysical Research: Oceans* 122.4, pp. 3152–3169. DOI:10.1002/2016JC012545.
- Engelstad, A., B. Ruessink, P. Hoekstra, and M. van der Vegt (2018a). Observational data set: sediment transport during barrier island inundation. DOI:10.1002/2016JC012545.
- Engelstad, A., B. G. Ruessink, P. Hoekstra, and M. van der Vegt (2018b). Sand Suspension and Transport During Inundation of a Dutch Barrier Island. *Journal of Geophysical Research: Earth Surface* 123.12, pp. 3292–3307. DOI:10.1029/2018JF004736.
- Fiedler, J. W., P. B. Smit, K. L. Brodie, J. McNinch, and R. T. Guza (2018). Numerical modeling of wave runup on steep and mildly sloping natural beaches. *Coastal Engineering* 131. n/a, pp. 106–113. DOI:10.1016/j.coastaleng.2017.09.004.
- Fisher, J. S., S. P. Leatherman, and F. C. Perry (1974). Overwash processes on Assateague Island. In: *Proceedings of 14th Conference on Coastal Engineering*. ASCE Copenhagen, Denmark, pp. 1194–1211. DOI:10.1061/9780872621138.073.
- FitzGerald, D. M. and E. Pendleton (2002). Inlet formation and evolution of the sediment bypassing system: New Inlet, Cape Cod, Massachusetts. *Journal of Coastal Research* 36, pp. 290–299. DOI:10.1029/CE044P0158.
- FitzGerald, D. M., C. J. Hein, Z. Hughes, M. Kulp, I. Georgiou, and M. Miner (2018). Runaway Barrier Island Transgression Concept: Global Case Studies. In: *Barrier Dynamics and Response to Changing Climate*. Ed. by L. J. Moore and A. B. Murray. Cham: Springer International Publishing, pp. 3–56. DOI:10.1007/978-3-319-68086-6_1.
- Gallagher, E. L., S. Elgar, and R. Guza (1998). Observations of sand bar evolution on a natural beach. *Journal of Geophysical Research: Oceans* 103.C2, pp. 3203–3215. DOI:10.1029/97JC02765.
- Georgiou, I. Y., D. M. FitzGerald, and G. W. Stone (2005). The Impact of Physical Processes along the Louisiana Coast. *Journal of Coastal Research*, pp. 72–89.
- Goff, J. A., M. A. Allison, and S. P. S. Gulick (Apr. 2010). Offshore transport of sediment during cyclonic storms: Hurricane Ike (2008), Texas Gulf Coast, USA. *Geology* 38.4, pp. 351–354. DOI:10.1130/G30632.1.

- Grasso, F., H. Michallet, and E. Barthelemy (2011). Sediment transport associated with morphological beach changes forced by irregular asymmetric, skewed waves. *Journal of Geophysical Research: Oceans* 116.C03020. DOI:10.1029/2010JC006550.
- Grunnet, N. M., D.-J. R. Walstra, and B. G. Ruessink (2004). Process-based modelling of a shoreface nourishment. *Coastal Engineering* 51.7, pp. 581–607. DOI:10.1016/J.COASTALENG.2004.07.016.
- Guza, R. T. and F. Feddersen (2012). Effect of wave frequency and directional spread on shoreline runup. *Geophysical Research Letters* 39.11. DOI:10.1029/2012GL051959.
- Guza, R. T. and E. B. Thornton (Mar. 20, 1985). Observations of surf beat. *Journal of Geophysical Research: Oceans* 90 (C2), pp. 3161–3172. DOI:10.1029/JC090iC02p03161.
- Hanes, D. M. (1991). Suspension of sand due to wave groups. *Journal of Geophysical Research: Oceans* 96.C5, pp. 8911–8915. DOI:10.1029/91JC00571.
- Hanes, D. M. and D. A. Huntley (1986). Continuous measurements of suspended sand concentration in a wave dominated nearshore environment. *Continental Shelf Research* 6.4, pp. 585–596. DOI:HTTPS://DOI.ORG/10.1016/0278-4343(86)90024-5.
- Harter, C. and J. Figlus (2017). Numerical modeling of the morphodynamic response of a low-lying barrier island beach and foredune system inundated during Hurricane Ike using XBeach and CSHORE". *Coastal Engineering* 120, pp. 64–74. DOI:HTTPS://DOI.ORG/10.1016/J.COASTALENG.2016.11.005.
- Herbers, T. H. C., S. Elgar, R. T. Guza, and W. C. O'Reilly (June 1, 1995). Infragravity-Frequency (0.005–0.05 Hz) Motions on the Shelf. Part II: Free Waves. *Journal of Physical Oceanography* 25.6, pp. 1063–1079. DOI:10.1175/1520-0485(1995)025<1063:IFHMOT>2.0.CO;2.
- Herbers, T. H. C., N. R. Russnogle, and S. Elgar (2000). Spectral Energy Balance of Breaking Waves within the Surf Zone. *Journal of Physical Oceanography* 30.11, pp. 2723–2737. DOI:10.1175/1520-0485(2000)030<2723:SEBOBW>2.0.CO;2.
- Hoefel, F. and S. Elgar (2003). Wave-induced sediment transport and sandbar migration. *Science* 299.5614, pp. 1885–1887. DOI:10.1126/SCIENCE.1081448.
- Hoekstra, P., M. ten Haaf, P. Buijs, A. Oost, R. Klein Breteler, K. van der Giessen, and M. van der Vegt (2009). Washover development on mixed-energy, mesotidal barrier island systems. In: *Coastal Dynamics*. Vol. 83. World Scientific, pp. 25–32. DOI:10.1142/9789814282475_0085.
- Holland, K. T., R. A. Holman, and A. H. Sallenger (1991). Estimation of overwash bore velocities using video techniques. In: *Coastal Sediments*. ASCE, pp. 489–497. DOI:10.5670/OCEANOG.1993.02.
- Houser, C. and B. Greenwood (2007). Onshore Migration of a Swash Bar During a Storm. *Journal of Coastal Research*, pp. 1–14. DOI:10.2112/03-0135.1.
- Huntley, D. A. and D. M. Hanes (1987). Direct measurement of suspended sediment transport. In: *Proceedings Coastal Sediments '87*. ASCE, pp. 723–737.
- IPCC (2013). *Climate Change 2013: The Physical Science Basis. Contribution of Working Group I to the Fifth Assessment Report of the Intergovernmental Panel on Climate Change*. Cambridge, United Kingdom and New York, NY, USA: Cambridge University Press, p. 1535. DOI:10.1017/CBO9781107415324.
- Jaffe, B. E., R. W. Sternberg, and A. H. Sallenger (1984). The role of suspended sediment in shore-normal beach profile change. In: *Proc. 19th Int. Coastal Eng. Conf.* ASCE, pp. 1983–1996. DOI:10.1061/9780872624382.134.
- Janssen, T. T., J. A. Battjes, and A. R. van Dongeren (2003). Long waves induced by short-wave groups over a sloping bottom. *Journal of Geophysical Research: Oceans* 108 (C8), p. 3252. DOI:10.1029/2002JC001515.
- Kahn, J. and H. Roberts (1982). Variations in storm response along a microtidal transgressive barrier-island arc. *Sedimentary Geology* 33.2, pp. 129–146. DOI:HTTPS://DOI.ORG/10.1016/0037-0738(82)90046-X.
- Kularatne, S. and C. Pattiaratchi (Aug. 2014). The Role of Infragravity Waves in Near-Bed Cross-Shore Sediment Flux in the Breaker Zone. *Journal of Marine Science and Engineering* 2, pp. 568–592. DOI:10.3390/JMSE2030568.

- Leatherman, S. P. (1976). Barrier island dynamics: overwash processes and eolian transport. *Coastal Engineering Proceedings* 1.15, pp. 1958–1974. DOI:10.1061/9780872620834.114.
- Loeffler, M. A. M., C. C. de Leeuw, M. E. ten Haaf, S. K. Verbeek, A. P. Oost, A. P. Grootjans, E. J. Lammerms, and R. M. K. Haring (2011). *Back to Basics*. Het Tij Geleerd (Waddenvereniging, SBB, Natuurmonumenten, Rijkswaterstaat, It Fryske Gea) ru-Groningen, Radboud Universiteit Nijmegen, RU-Utrecht. ERA, p. 44.
- Long, J. W., A. T. M. de Bakker, and N. G. Plant (2014). Scaling coastal dune elevation changes across storm-impact regimes. *Geophysical Research Letters* 41.8, pp. 2899–2906. DOI:10.1002/2014GL059616.
- Longuet-Higgins, M. S. and R. W. Stewart (1964). Radiation stresses in water waves; a physical discussion, with applications. In: *Deep Sea Research and Oceanographic Abstracts*. Vol. 11. 4. Elsevier, pp. 529–562. DOI:10.1016/0011-7471(64)90001-4.
- Lorenzo-Trueba, J. and A. D. Ashton (2014). Rollover, drowning, and discontinuous retreat: Distinct modes of barrier response to sea-level rise arising from a simple morphodynamic model. *Journal of Geophysical Research: Earth Surface* 119.4, pp. 779–801. DOI:10.1002/2013JF002941.
- Masselink, G. and S. van Heteren (2014). Response of wave-dominated and mixed-energy barriers to storms. *Marine Geology* 352, pp. 321–347. DOI:10.1016/J.MARGEO.2013.11.004.
- Matias, A., Ó. Ferreira, A. Vila-Concejo, T. Garcia, and J. A. Dias (2008). Classification of washover dynamics in barrier islands. *Geomorphology* 97.3, pp. 655–674. DOI:10.1016/J.GEOMORPH.2007.09.010.
- Matias, A., Ó. Ferreira, A. Vila-Concejo, B. Morris, J. Dias, F. A., and B. Dias (Jan. 2009). Foreshore and hydrodynamic factors governing overwash. *Journal of Coastal Research SI* 56, pp. 636–640.
- Matias, A., Ó. Ferreira, A. Vila-Concejo, B. Morris, and J. A. Dias (2010). Short-term morphodynamics of non-storm overwash. *Marine Geology* 274.1, pp. 69–84. DOI:10.1016/J.MARGEO.2010.03.006.
- Matias, A., G. Masselink, A. Kroon, C. E. Blenkinsopp, and I. L. Turner (2013). Overwash experiment on a sandy barrier. *Journal of Coastal Research* 1.65, p. 778. DOI:10.2112/SI65-132.1.
- McCall, R. T., J. S. M. Van Thiel De Vries, N. G. Plant, A. R. Van Dongeren, J. A. Roelvink, D. M. Thompson, and A. J. H. M. Reniers (2010). Two-dimensional time dependent hurricane overwash and erosion modeling at Santa Rosa Island. *Coastal Engineering* 57.7, pp. 668–683. DOI:10.1016/J.COASTALENG.2010.02.006.
- McCall, R. T., N. Plant, and J. Van Thiel de Vries (2011). The effect of longshore topographic variation on overwash modelling. *Coastal Engineering Proceedings* 1.32, p. 36. DOI:10.9753/ICCE.V32.SEDIMENT.36.
- Mori, N., T. Suzuki, and S. Kakuno (2007). Noise of Acoustic Doppler Velocimeter Data in Bubbly Flows. *Journal of Engineering Mechanics* 133.1, pp. 122–125. DOI:10.1061/(ASCE)0733-9399(2007)133:1(122).
- Morton, R. A. and A. H. Sallenger (2003). Morphological impacts of extreme storms on sandy beaches and barriers. *Journal of Coastal Research* 19, pp. 560–573. DOI:10.1007/0-387-30843-1_51.
- Nielsen, N and J. Nielsen (2006). Development of a washover fan on a transgressive barrier, Skallingen, Denmark. *Journal of Coastal Research* 39, pp. 107–111. DOI:10.1007/SPRINGERREFERENCE_4799.
- Oost, A. P. et al. (2012). Barrier island management: lessons from the past and directions for the future. *Ocean & Coastal Management* 68, pp. 18–38. DOI:10.1016/J.OCECOAMAN.2012.07.010.
- Passeri, D. L., M. V. Bilskie, N. G. Plant, J. W. Long, and S. C. Hagen (Aug. 2018). Dynamic modeling of barrier island response to hurricane storm surge under future sea level rise. *Climatic Change* 149.3, pp. 413–425. DOI:10.1007/s10584-018-2245-8.
- Pomeroy, A., R. Lowe, G. Symonds, A. Van Dongeren, and C. Moore (2012). The dynamics of infragravity wave transformation over a fringing reef. *Journal of Geophysical Research: Oceans* 117.C11. DOI:10.1029/2012JC008310.
- Pomeroy, A., R. Lowe, A. Van Dongeren, M. Ghisalberti, and D. Roelvink (Apr. 2015). Spectral wave-driven sediment transport across a fringing reef. *Coastal Engineering* 98, pp. 78–94. DOI:10.1016/J.COASTALENG.2015.01.005.

- Raubenheimer, B., S. Elgar, and R. T. Guza (1998). Estimating Wave Heights from Pressure Measured in Sand Bed. *Journal of Waterway, Port, Coastal, and Ocean Engineering* 124.3, pp. 151–154. DOI:10.1061/(ASCE)0733-950X(1998)124:3(151).
- Ribberink, J. S. and A. A. Al-Salem (1995). Sheet flow and suspension of sand in oscillatory boundary layers. *Coastal Engineering* 25.3, pp. 205–225. DOI:10.1016/0378-3839(95)00003-T.
- Rijnsdorp, D., P. Smit, and M. Zijlema (2012). NON-HYDROSTATIC MODELLING OF INFRA-GRAVITY WAVES USING SWASH. *Coastal Engineering Proceedings* 1.33, p. 27. DOI:10.9753/ICCE.V33.CURRENTS.27.
- Rijnsdorp, D. P., P. B. Smit, and M. Zijlema (2014). Non-hydrostatic modelling of infragravity waves under laboratory conditions. *Coastal Engineering* 85, pp. 30–42. DOI:10.1016/J.COASTALENG.2013.11.011.
- Rijnsdorp, D. P., G. Ruessink, and M. Zijlema (2015). Infragravity-wave dynamics in a barred coastal region, a numerical study. *Journal of Geophysical Research: Oceans* 120.6, pp. 4068–4089. DOI:10.1002/2014JC010450.
- Roelvink, J. A. and M. J. F. Stive (1989). Bar-generating cross-shore flow mechanisms on a beach. *Journal of Geophysical Research: Oceans* 94.C4, pp. 4785–4800. DOI:10.1029/JC094IC04P04785.
- Rosati, J. and G. W. Stone (2007). Critical Width of Barrier Islands and Implications for Engineering Design, pp. 1–14. DOI:10.1061/40926(239)156.
- Rosati, J. D. and G. W. Stone (2009). Geomorphologic Evolution of Barrier Islands along the Northern U.S. Gulf of Mexico and Implications for Engineering Design in Barrier Restoration. *Journal of Coastal Research* 25, pp. 8–22. DOI:10.2112/07-0934.1.
- Ruessink, B. G. (2010). Observations of Turbulence within a Natural Surf Zone. *Journal of Physical Oceanography* 40.12, pp. 2696–2712. DOI:10.1175/2010JPO4466.1.
- Ruessink, B. G., M. G. Kleinhan, and P. G. L. den Beukel (1998a). Observations of swash under highly dissipative conditions. *Journal of Geophysical Research: Oceans* 103.C2, pp. 3111–3118. DOI:10.1029/97JC02791.
- Ruessink, B. G., K. T. Houwman, and P. Hoekstra (Aug. 1998b). The systematic contribution of transporting mechanisms to the cross-shore sediment transport in water depths of 3 to 9 m. *Marine Geology* 152, pp. 295–324. DOI:10.1016/S0025-3227(98)00133-9.
- Ruessink, B. G., J. R. Miles, F. Feddersen, R. T. Guza, and S. Elgar (2001). Modeling the alongshore current on barred beaches. *Journal of Geophysical Research* 106.C10, pp. 22451–22463. DOI:10.1029/2000JC000766.
- Ruessink, B. G., T. J. J. van den Berg, and L. C. van Rijn (2009). Modeling sediment transport beneath skewed asymmetric waves above a plane bed. *Journal of Geophysical Research: Oceans* 114.C11. C11021. DOI:10.1029/2009JC005416.
- Ruessink, B. G., H. Michallet, T. Abreu, F. Sancho, D. A. Van der A, J. J. Van der Werf, and P. A. Silva (2011). Observations of velocities, sand concentrations, and fluxes under velocity-asymmetric oscillatory flows. *Journal of Geophysical Research: Oceans* 116.C3. C03004. DOI:10.1029/2010JC006443.
- Russell, P. E. (1993). Mechanisms for beach erosion during storms. *Continental Shelf Research* 13.11, pp. 1243–1265. DOI:10.1016/0278-4343(93)90051-X.
- Safak, I., J. C. Warner, and J. H. List (2016). Barrier island breach evolution: Alongshore transport and bay-ocean pressure gradient interactions. *Journal of Geophysical Research: Oceans* 121.12, pp. 8720–8730. DOI:10.1002/2016JC012029.
- Sallenger, A. H., Jr. (2000). Storm impact scale for barrier islands. *Journal of Coastal Research* 16, pp. 890–895. DOI:10.1306/44B4BA04-170A-11D7-8645000102C1865D.
- Schupp, C. A., N. T. Winn, T. L. Pearl, J. P. Kumer, T. J. Carruthers, and C. S. Zimmerman (2013). Restoration of overwash processes creates piping plover (*Charadrius melodus*) habitat on a barrier island (Assateague Island, Maryland). *Estuarine, Coastal and Shelf Science* 116, pp. 11–20. DOI:10.1016/J.ECSS.2012.07.003.

- Sherwood, C. R., J. W. Long, P. J. Dickhudt, P. S. Dalyander, D. M. Thompson, and N. G. Plant (2014). Inundation of a barrier island (Chandeleur Islands, Louisiana, USA) during a hurricane: Observed water-level gradients and modeled seaward sand transport. *Journal of Geophysical Research: Earth Surface* 119.7, pp. 1498–1515. DOI:10.1002/2013JF003069.
- Smit, P., M. Zijlema, and G. Stelling (2013). Depth-induced wave breaking in a non-hydrostatic, near-shore wave model. *Coastal Engineering* 76, pp. 1–16. DOI:10.1016/J.COASTALENG.2013.01.008.
- Smit, P., T. Janssen, L. Holthuijsen, and J. Smith (2014). Non-hydrostatic modeling of surf zone wave dynamics. *Coastal Engineering* 83, pp. 36–48. DOI:HTTPS://DOI.ORG/10.1016/J.COASTALENG.2013.09.005.
- Stockdon, H. F., R. A. Holman, P. A. Howd, and A. H. Sallenger (2006). Empirical parameterization of setup, swash, and runup. *Coastal Engineering* 53.7, pp. 573–588. DOI:10.1016/J.COASTALENG.2005.12.005.
- Stone, G. W. and R. A. McBride (1998). Louisiana Barrier Islands and Their Importance in Wetland Protection: Forecasting Shoreline Change and Subsequent Response of Wave Climate. *Journal of Coastal Research* 14.3, pp. 900–915.
- Stutz, M. L. and O. H. Pilkey (2011). Open-Ocean Barrier Islands: Global Influence of Climatic, Oceanographic, and Depositional Settings. *Journal of Coastal Research*, pp. 207–222. DOI:10.2112/09-1190.1.
- Swart, D. (1974). A Schematization of Onshore-Offshore Transport. *Coastal Engineering Proceedings* 1.14. DOI:10.1061/9780872621138.054.
- Symonds, G., K. P. Black, and I. R. Young (1995). Wave-driven flow over shallow reefs. *Journal of Geophysical Research* 100 (C2), p. 2639. DOI:10.1029/94JC02736.
- Thornton, E. B., R. T. Humiston, and W. Birkemeier (1996). Bar/trough generation on a natural beach. *Journal of Geophysical Research: Oceans* 101.C5, pp. 12097–12110. DOI:10.1029/96JC00209.
- Thornton, E. B. and R. T. Guza (1983). Transformation of wave height distribution. *Journal of Geophysical Research: Oceans* 88.C10, pp. 5925–5938. DOI:10.1029/JC088IC10P05925.
- Tissier, M., P. Bonneton, H. Michallet, and B. G. Ruessink (2015). Infragravity-wave modulation of short-wave celerity in the surf zone. *Journal of Geophysical Research: Oceans* 120.10, pp. 6799–6814. DOI:10.1002/2015JC010708.
- Van der Spek, A. J. (2018). The development of the tidal basins in the Dutch Wadden Sea until 2100: the impact of accelerated sea-level rise and subsidence on their sediment budget ? a synthesis. *Netherlands Journal of Geosciences* 97.3, 71?78. DOI:10.1017/NJG.2018.10.
- Van der Vegt, M and P Hoekstra (2012). Morphodynamics of a storm-dominated, shallow tidal inlet: the Slufter, the Netherlands. *Netherlands Journal of Geosciences* 91.03, pp. 325–339. DOI:10.1017/S0016774600000470.
- Van Dongeren, A and M Van Ormondt (2007). Hydrodynamic Aspects of Overwash. *Framework: H&I Zeereep (Report in Dutch), WL Delft Hydraulics, report Z 4412*, p. 33. DOI:10.1142/9789814355537_0137.
- Van Dongeren, A, J Battjes, T Janssen, J Van Noorloos, K Steenhauer, G Steenbergen, and A. J.H. M. Reniers (2007). Shoaling and shoreline dissipation of low-frequency waves. *Journal of Geophysical Research: Oceans* 112.C2. DOI:10.1029/2006JC003701.
- Van Dongeren, A., R. Lowe, A. Pomeroy, D. M. Trang, D. Roelvink, G. Symonds, and R. Ranasinghe (2013). Numerical modeling of low-frequency wave dynamics over a fringing coral reef. *Coastal Engineering* 73, pp. 178–190. DOI:10.1016/J.COASTALENG.2012.11.004.
- Van Rijn, L. (1993). *Principles of sediment transport in rivers, estuaries and coastal seas*. Aqua Publications, Amsterdam, The Netherlands.
- Vermeersen, B. L. et al. (2018). Sea-level change in the Dutch Wadden Sea. *Netherlands Journal of Geosciences* 97.3, 79?127. DOI:10.1017/NJG.2018.7.
- Wamdi Group (1988). The WAM model-a third generation ocean wave prediction model. *Journal of Physical Oceanography* 18.12, pp. 1775–1810. DOI:10.1175/1520-0485(1988)018<1775:TWMTOG>2.0.CO;2.

- Wang, Z. B., E. P. Elias, A. J. van der Spek, and Q. J. Lodder (2018). Sediment budget and morphological development of the Dutch Wadden Sea: impact of accelerated sea-level rise and subsidence until 2100. *Netherlands Journal of Geosciences* 97.3, 183–214. DOI:10.1017/NJG.2018.8.
- Wesselman, D., R. de Winter, A. Oost, P. Hoekstra, and M. van der Vegt (2019). The effect of washover geometry on sediment transport during inundation events. *Geomorphology* 327, pp. 28–47. DOI:DOI.ORG/10.1016/J.GEOMORPH.2018.10.014.
- Wesselman, D., R. Winter, A. Engelstad, R. McCall, A. Dongeren, P. Hoekstra, A. Oost, and M. Vegt (2017). The effect of tides and storms on the sediment transport across a Dutch barrier island. *Earth Surface Processes and Landforms* 43.3, pp. 579–592. DOI:10.1002/ESP.4235.
- Wu, J. (1982). Wind-stress coefficients over sea surface from breeze to hurricane. *Journal of Geophysical Research: Oceans* 87.C12, pp. 9704–9706. DOI:10.1029/JC087IC12P09704.
- Zijlema, M., G. Stelling, and P. Smit (2011). SWASH: An operational public domain code for simulating wave fields and rapidly varied flows in coastal waters. *Coastal Engineering* 58.10, pp. 992–1012. DOI:10.1016/J.COASTALENG.2011.05.015.

Acknowledgements/Dankwoorden/Danksagung

None of these pages would have been written without the support of the many people who accompanied and supported me during this journey into the wonders of barrier island inundation, professionally and private. Maarten, Gerben, and Piet, you were my supervisors and promoters. I am extremely grateful for all your support and the knowledge you shared with me. Maarten, thank you for your guidance throughout this work. Your immense knowledge about the physical processes of the coast and tidal basins are inspiring. Many of your creative ideas are reflected in this work. You let me room to grow on my own, but always pulled me back to the main questions when I left the orbit or got hung up in details. Your willingness to let me work remotely whenever possible enabled me to see this through. Thank you for that and all the Skype meetings we had. Gerben, I admire your profound knowledge of waves and sediment transport (to just name a few examples). Thank you for letting me ask you a thousand questions on a broad variety of topics from field instrumentation to infragravity waves and for patiently explaining some concepts more than once. Piet, you gave me insight into the larger Wadden Sea processes and valuable feedback even at times when you were already swamped with work. You always had the bigger picture in mind. I value your perspective and the detailed comments you gave on our publications. Albert, thank you for showing me the beauty of barrier islands and for sharing your love, knowledge and dedication of the Wadden Sea. A special thanks goes to the technicians of the Department of Physical Geography, Marcel, Henk, Arjan, Chris (you left too soon), Bas and Hans. The collection of all the field data would not have been possible without you. I enjoyed the days in the field and the evenings in de Tjattel. Marcel, thanks for patiently answering all my questions. Henk, thank you for going on a long quad-ride with me in the middle of winter and sweetening the field work in the cold with hot cacao.

Thanks go to many colleagues at the Department, but especially to the Coastal group. Anouk, Christian, Daan, Gerben, Jantien, Jasper, Joost, Klaas, Laura, Maarten, Nynke, Pam, Piet, Renske, Sepehr, Tim, Winnie, and Yvonne, I valued the talks and discussions in the coffee corner, during meetings and at conferences. Daan, I enjoyed our fieldworks and the adventures we had on the flooded parts of Schiermonnikoog and Texel. You taught me such important Dutch expressions such as "hatseflats", and always made sure that I did not feel left out when I could not follow conversations in Dutch. Our discussions in the office and over coffee were an important part of my stays in the Netherlands. Daan and Pam, you were the best office mates. Anouk, thank you for patiently explaining the mysteries of infragravity waves and bispectral analysis to me, and providing me with scripts and papers on the subject. Joyce, Jasper, Jantien and Steffi thanks for your friendship and the time we spent on the walls of Utrecht's climbing halls, having dinners and drinks. Steffi, I wouldn't have made it through the first year without you! And even though it did not always feel that way in the beginning, I enjoyed my time in the Netherlands and the Dutch way of life, such as the "gezelligheid", a lot. I learned much more than just wave and current processes during barrier island inundation, because many of you granted me insight into the Dutch culture (for example when Nynke made me read "De Schippers Van De Kameleon").

This journey started when I decided to take an oceanography class at City College of San Francisco instead of a plant identification class as planned. Katryn's oceanography class taught me firstmost that studying can be fun, and it inspired me to continue my studies. Katryn, I am very happy that I had you as a teacher and still have you as a friend. Tim Janssen enthusiastically shared with me his deep understanding of oceanic processes (even though I was lost at times) and guided me through my master degree.

My sister Antje, Christin, Danièle, Elke and Elke, Greta, my mom Hanne, Heike, Joe, Ursel, it made me happy to be closer to all of you again during my Utrecht studies. My visits in Stuttgart, Heilbronn, Brussels, and Berlin restored my energy and your support carried me through the years. You went through all the ups and downs with me, listened to my barrier island stories, celebrated successes or provided tissues or laughter when I was in doubt. Your visits in Utrecht made me enjoy the city and the surroundings even more. I miss having you all in my life here in the US. However, the distance does not change the place that you have in my heart. Karen and Jay, you shaped my past and my future, and I am happy to have you as my friends.

Ralf, none of this would have been possible without you. Our journey stretched over an ocean and a continent, and I am curious to see where it will take us next. Your love of volcanoes awoke my interest in the world of science, long before I actually started with my studies. You supported me through all these years and believed in me. You would not let me give up when I was close to doing so, even though it meant that we spent months apart. Thank you for being my "significant otter"!

Anita Engelstad
San Francisco, September 2019

About the author

Anita Engelstad was born on the 24th of December 1965 in Heidelberg, Germany. She went to high school in Stuttgart, but dropped out early to pursue her dream of being a landscaper. For many years she worked with friends and colleagues at "Blattwerk Gartengestaltung", planning, building and maintaining gardens of all sizes. After moving to San Francisco, her love for the ocean and interest in wave processes lead her to pursue a bachelor degree in Atmospheric and Oceanic Sciences at San Francisco State University (SFSU). This was followed by a Master degree in Geosciences at SFSU, which investigated the damping characteristics of waves propagating across the muddy Louisiana shelf. This research was focused on wave-mud interactions in the Gulf of Mexico and included the analysis of an extensive wave data-set and numerical modeling. Since she continued to be fascinated by wave processes, she moved to Utrecht, the Netherlands, and started her PhD candidacy in 2014. The work was part of the project "Rebuilding the natural integrity of barrier islands - restoration of washovers" and was focused on barrier island inundation. Since April 2019, Anita is working at the US Army Corps of Engineers (USACE) in San Francisco, USA.

Publications

Journal papers

- ENGELSTAD, A., B.G. RUESSINK, P. HOEKSTRA, & M. VAN DER VEGT. (under review), Sediment transport processes during barrier island inundation under variations in cross-shore geometry and hydrodynamic forcing. *Journal of Marine Science and Engineering*.
- ENGELSTAD, A., B.G. RUESSINK, P. HOEKSTRA & M. VAN DER VEGT (2018), Sand suspension and transport during inundation of a dutch barrier island. *Journal of Geophysical Research: Earth Surface* 123 (12), 3292-3307.
- WESSELMAN, A., R. WINTER, A. ENGELSTAD, R. MCCALL, A. VAN DONGEREN, P. HOEKSTRA, A. OOST & M. VAN DER VEGT (2017), The effect of tides and storms on the sediment transport across a Dutch barrier island. *Earth Surface Processes and Landforms* 43, 579-592.
- ENGELSTAD, A., B.G. RUESSINK, D. WESSELMAN, P. HOEKSTRA, A. OOST & M. VAN DER VEGT (2017), Observations of waves and currents during barrier island inundation. *Journal of Geophysical Research: Oceans* 122,3152-3169.
- ENGELSTAD, A., T.T. JANSSEN, T.H.C. HERBERS, G. VAN VLEDDER, S. ELGAR, R. RAUBENHEIMER, L. TRAINOR & A. GARCIA-GARCIA (2013), Wave evolution across the Louisiana shelf. *Continental Shelf Research* 52, 190-202.

Conference abstracts and proceedings

- ENGELSTAD, A., M. VAN DER VEGT, B.G. RUESSINK, & P. HOEKSTRA (2018), Observations of sediment transport during the inundation of a barrier island. Ocean Sciences Conference, 2018, Portland, USA (poster).
- ENGELSTAD, A., B.G. RUESSINK & M. VAN DER VEGT (2017), The effect of island slopes on wave transformation during overwash and inundation. Proceedings of the 8th International Conference on Coastal Dynamics, Helsingør, Denmark, 1701-1710 (oral).
- ENGELSTAD, A., B.G. RUESSINK, P. HOEKSTRA & M. VAN DER VEGT. (2017), How island slopes effect wave shape and transformation during island inundation. NCK days, 2017, Den Helder, the Netherlands (poster).
- ENGELSTAD, A., M. VAN DER VEGT, B.G. RUESSINK, P. HOEKSTRA, A. OOST & D. WESSELMAN (2017), Observations of the hydrodynamics during inundation on Schiermonnikoog. Workshop NWO & NCK: Building with Nature, Utrecht, the Netherlands (poster).
- ENGELSTAD, A., M. VAN DER VEGT, B.G. RUESSINK, & D. WESSELMAN (2016), Observations of waves and currents on an inundated barrier island: the role of the back-barrier basin. Ocean Sciences Conference, 2016, New Orleans, USA (poster).
- ENGELSTAD, A., M. VAN DER VEGT & D. WESSELMAN. (2015), Observations of waves crossing a barrier island during overwash. BBOS symposium, 2015, Renesse, the Netherlands (oral).
- ENGELSTAD, A., M. VAN DER VEGT & P. HOEKSTRA . (2015), Overwash observations on a Dutch barrier island. NCK days, 2015, Schoorl, the Netherlands (poster).

Utrecht University
Faculty of Geosciences
Department of Physical Geography